Experimental Investigation of Particle-Flow Interaction in Turbulent Channel Flows

by

Farzad Ahmadi Jokani

A thesis submitted in partial fulfillment of the requirements for the degree of

Doctor of Philosophy

Department of Mechanical Engineering
University of Alberta

Abstract

The transportation of mixtures of particles and liquids using slurry pipelines plays a crucial role in the petroleum and mining industries. Slurry pipeline flows are typically turbulent and the presence of the particulate phase results in pipe wear and increased pumping cost. As a result, slurry pipeline design and operation relies on analysis and modeling of turbulent two-phase flows. The main objective of this research is to study the transport and dispersion mechanism of particles in particle-laden turbulent flows. To achieve this goal, a series of experimental studies were performed in a horizontal turbulent channel flow. The research started by investigating the effect of the flow Reynolds number (Re), particle size, and volumetric concentration of the solid phase on the turbulence statistics of the particles and the liquid carrier phase. A combined two-dimensional particle tracking velocimetry (PTV) and particle image velocimetry (PIV) was used to obtain the instantaneous velocity of the glass beads and liquid phase. The PTV results indicated that the turbulence intensity of the particulates decreases with increase of Stokes number (St). It was also observed that the turbulence modulation of the liquid phase depends on the particle Reynolds number (Re_p). The turbulence intensity of the liquid phase augmented when Re_p was large enough to produce vortex shedding.

To study the interaction between the particles and turbulent events, an experiment was conducted to simultaneously measure the velocity of particles and the carrier liquid phase. Time-resolved three-dimensional PTV (3D-PTV) method based on shake-the-box algorithm was employed in this study. A conditional sampling of the beads and their surrounding fluid, based on the bead wall-normal motion, showed that the beads ascending from the bottom wall were mostly located within ejection motions of the fluid. However, the beads descending

to the bottom wall did not indicate any correlation with the streamwise fluid velocity.

Distribution of the glass beads in the near-wall region of a horizontal turbulent channel flow was studied to investigate the effect of different particle transport mechanisms. In addition to the gravitational settling and turbulence dispersion, it was identified that shear-induced lift, particle-wall lubrication, and inter-particle collisions affect the distribution of the beads. The shear-induced lift force was effective at larger Re and smaller concentrations, and tended to create a core-peaking profile of particle concentration. The number of inter-particle collisions became larger for the denser suspensions, which confined the beads to a region of high concentration near the wall.

The simultaneous velocity of the beads and their surrounding fluid was used to calculate the quasi-steady and viscous-unsteady forces in turbulent channel flow. It was observed that the viscous-unsteady force is significant in turbulent solid-liquid flows. This force is negatively correlated to the net force on the beads. It tends to reduce the magnitude of the acceleration. Investigation of the quasi-steady force showed that this is the main source of acceleration in the streamwise direction. The importance of this force reduced in the transverse directions.

Preface

This thesis is the original work by Farzad Ahmadi Jokani. All of the experiments and data processing were performed under the supervision of Dr. Sina Ghaemi and Dr. Sean Sanders.

The results presented in Chapter 4 have been published in the *International Journal of Multiphase Flow*. Masoud Ebrahimian helped me in conducting the experiments in this part of study.

- F. Ahmadi, M. Ebrahimian, R.S. Sanders, S. Ghaemi, 'Particle image and tracking velocimetry of solid-liquid turbulence in a horizontal channel flow', International Journal of Multiphase Flow (2019) vol: 112 pp: 83-99.

The results presented in Chapter 5 have been published in the journal of *Physical Review Fluids*.

- F. Ahmadi, S. Sanders, S. Ghaemi, 'Experimental investigation of three-dimensional flow around particles in a turbulent channel flow', Phys. Rev. Fluids 5, 014302.

The results presented in Chapter 6 have been submitted to the *International Journal of Multiphase Flow*.

Dedicated to my grandmothers and to the loving memory of my grandfather

for their love and for the value they placed on family

Acknowledgments

Firstly, I would like to express my sincere gratitude to my supervisors Dr. Sina Ghaemi and Dr. Sean Sanders for their continuous support of my PhD study, for their patience, and knowledge. I would like to thank Dr. Ghaemi for giving me the opportunity to grow as a research scientist and Dr. Sanders who taught me how to deal with the difficulties and challenges in the work.

I would like to extend my appreciation to Dr. Alexandra Komrakova for her insightful comments and constructive criticisms at different stages of my research. I also would like to thank Dr. Mark Martinez, Dr. Jaime Wong, and Dr. Arman Hemmati for serving in my Doctoral defense exam.

I really appreciate the help and support of my fellow labmates in the *Laboratory of Turbulent Flows*. I am specially grateful to Dr. Mohammad Mohammadtabar, Dr. Masoud Ebrahimian, Sadek Shaban, Sen Wang, Desiree Reholon Inojosa, and Dr. Wagih Abu Rowin. It was a pleasure for me to work and spend time with them. I would like to also thank my dear friends Majid Bizhani, Amirhossein Mahdavi, Arman Peyravi, Shahed Taghian, Mohammad Fayyaz and Mohsen Safaei for their support and constructive discussion we had.

Last but not the least, I would like to thank my family: my parents and my brothers for supporting me spiritually through all these years, and my wife for her dedication, and understanding. Her love helped me through tough situations.

Contents

List of Tables

List of Figures

Nomenclature

Abbreviations

cyl	Cylindrical
qs	Quasi-steady
sph	Spherical
3D	Three-dimensional
BBO	Basset-Boussinesq-Oseen
CCD	Charge-coupled device
CMOS	Complementary metal oxide semiconductor
DNS	Direct numerical simulation
FOV	Field of view
LDA	Laser Doppler anemometry
max	Maximum
min	Minimum
OTF	Optical transfer function
PDF	Probability density function
PIV	Particle image velocimetry
ppp	Particle per pixel
PSD	Power spectral density
PTV	Particle tracking velocimetry
rms	Root mean square
STB	Shake-the-box
VIC+	Vortex-in-cell plus

Greek Letters

β	Collision kernel
ϵ	Dissipation rate of turbulence

η	Kolmogorov length scale
κ	von Kármán constant
λ	Wall unit
μ	Dynamic viscosity
ν	Kinematic viscosity
ϕ_v	Bulk volumetric concentration
ρ	Fluid density
ρ_u	Streamwise correlation coefficient
ρ_v	Wall-normal correlation coefficient
ρ_w	Spanwise correlation coefficient
ρ_{uu}	Temporal autocorrelation of streamwise velocity fluctuation
σ	Standard deviation
τ	Shear stress
τ_b	Bead response time
τ_K	Kolmogorov time scale
τ_L	Integral time scale
τ_v	Viscous time scale
τ_w	Wall shear stress
τ_{vu}	Viscous-unsteady time scale
ε	Measurement error

Superscripts

$+$	normalized by the corresponding inner scaling

Symbols

$\langle\rangle_c$	Conditional average
$\langle u^2 \rangle$	Streamwise Reynolds stress
$\langle uv \rangle$	Reynolds shear stress
$\langle v^2 \rangle$	Wall-normal Reynolds stress
$\langle w^2 \rangle$	Spanwise Reynolds stress
τ_c	Estimated time required for the collision of beads pairs
$\boldsymbol{U}$	Velocity vector
$\boldsymbol{x}_r$	Distance vector between beads pairs

a	Acceleration
a_B	Viscous-unsteady (Basset) acceleration
a_S	Quasi-steady (Stokes) acceleration
B	Intercept of the logarithmic profile
C_M	Added-mass coefficient
d_b	Beads' diameter
f	Focal length of lens
f_c	Collision frequency
f_d	Drag factor
F_{am}	Apparent mass force
F_{qs}	Quasi-steady force
F_{sg}	Stress-gradient force
F_{SL}	Shear-lift force
F_{vu}	Viscous-unsteady force
h	Channel height
k	Turbulent kinetic energy
K_B	Basset kernel
l_m	Mixing length
M	Turbulence modulation
m_b	Mass of a bead
m_f	mass of fluid displaced by the particle
n	Number density of particles
P	Static pressure
p	Pressure fluctuation
Pa	Particle momentum number
R_{TI}	Relative turbulence intensity
Re	Reynolds number
Re_τ	Friction Reynolds number
Re_p	Particle Reynolds number
St	Stokes number
T^v	Tensor of viscous stress

T_b	Integral time scale of beads motion
U	Instantaneous streamwise velocity
u	Streamwise velocity fluctuation
u_τ	Friction velocity
V	Instantaneous wall-normal velocity
v	Wall-normal velocity fluctuation
v_r	Relative velocity between the particles
V_s	Terminal settling velocity
W	Instantaneous spanwise velocity
w	Spanwise velocity fluctuation
x	Streamwise direction
y	Wall-normal distance from the bottom wall
z	Spanwise direction

Subscripts

b	Bead
b	Bulk quantity
f	Fluid
i, j	Tensor index notation
PL	Particle-laden
UL	Unladen flow
avg	Average
c	Centerline

Chapter 1

Introduction

1.1 Motivation

The transport of solid particles by turbulent liquid flows occurs abundantly in nature and in the industry; two examples are particle transport in river flows and mining operations. Slurry pipelines are an effective way of transport for tailings, mineral ores, and industrial minerals. Material degradation and wear by erosion is one of the main concerns with these pipelines. The erosion due to particle-wall collision reduces the lifetime of the pipes and other equipment such as the valves and the pumps, and consequently, raises the cost of the projects. For example, Pipe inspection and replacement, and maintenance cost up to $1 billion in the Alberta Oil Sands industry [Fuhr et al., 2014].

In an attempt to reduce costs from material wear in particle-laden systems, extensive studies have been performed to understand the wear mechanism. Accurate models should be developed to predict the wear rate as a function of the main flow conditions. However, the knowledge is still limited since the erosion process is complicated and depends on many factors. The velocity and concentration of the particulates near the surface, and the local flow and turbulence field determine the frequency of particle-wall collision. These further depend on the flow characteristics such as the flow Re, particulate size, and the bulk concentration of the particulates. The main target of the current study is to answer the following questions

- How do the main flow conditions such as the particulate size and flow Re affect the

particulate velocity near the wall?

- How do the flow conditions change the concentration of the particles in the near-wall region?

- How do the particulates interact with the turbulence in the carrier phase? and

- What are the main forces on the particles in solid-liquid turbulent flow?

One phenomenon that is particularly poorly understood, and one that most models do not properly address, is the fact that carrier phase turbulence can be augmented or reduced by the presence of the dispersed phase. The change in the turbulence kinetic energy of the carrier phase when particles are added is referred to as turbulence modulation. Turbulence modulation is important since it can modify the behavior of particle-laden turbulent flows. Two mechanisms are identified to be responsible for turbulence attenuation: (a) the increased effective viscosity of the suspension and (b) increased dissipation arising from the particle drag [Balachandar and Eaton, 2010]. On the other hand, turbulence can be enhanced because of (a) increased velocity fluctuation in a particle wake due to the vortex shedding, and (b) buoyancy-induced instabilities arising from density gradients due to the preferential particle distribution [Balachandar and Eaton, 2010]. The length scale at which these mechanisms are effective varies. Accordingly, a particle can simultaneously enhance or reduce the turbulence over a different range of scales, and the overall modulation depends on the relative strength of these mechanisms. In addition, turbulence modulation depends on many factors such as particle size and density, flow Re, and volumetric concentration of the particles. Due to the wide differences in flow conditions of many earlier studies, it is difficult to draw a definite conclusion on the effect of different flow conditions. This has provided the motivation for this experimental investigation of turbulence statistics of the carrier and particulate phases over a consistent and wide range of conditions.

Another aspect of particle-laden turbulent flow is the spatial distribution of the particles across the conduit. The particles are transported by several mechanisms including gravitational settling, dispersion by turbulence, turbophoresis [Caporaloni et al., 1975],

inter-particle collisions [Abrahamson, 1975], and shear-induced lift [Saffman, 1965, Auton, 1987]. These mechanisms may oppose each other and their strength varies with several conditions including fluid velocity and turbulence, particle size and density, and bulk particle concentration [Kussin and Sommerfeld, 2002, Picano et al., 2015, Capecelatro and Desjardins, 2015, Capecelatro et al., 2018, Zade et al., 2018]. As a result, the particles may not uniformly disperse in the carrier phase. This is specifically important in the near-wall region since the local particle concentration directly affects the pressure drop and wear-rate of the surface material [Roco and Addie, 1987]. The relative strength of these mechanisms over a wide range of Re and volumetric concentration in the near-wall region of a horizontal channel is investigated in the current study.

A key feature of particle distributions in turbulent flows is the preferential accumulation of particles over different turbulent events. Here, turbulent events refer to outward interaction, ejection, inward interaction, and sweep. Distribution of the particles over these events has been studied in the literature based on whether the particles ascend from, or descend to, the bottom wall. This study also helps to identify how the particles are transported and how they stay in suspension in turbulent flows. The ascending particles typically originate from the slower near-wall flow and therefore have a smaller mean streamwise velocity than the descending particles [Nino and Garcia, 1996]. It has been stated in the literature that ascending particles preferentially accumulate in the ejection motions of the liquid phase, while descending particles have less preference to segregate in the sweep motions of the liquid phase towards the wall.

Accurate prediction of different forces acting on a particle is important in the modeling and simulation of the particle dynamics in particle-laden flows. The equation of motion for a small rigid particle was developed by Tchen [1947] and Maxey and Riley [1983]. This equation, known as the Basset-Boussinesq-Oseen (BBO) equation, relates particle acceleration to the effect of quasi-steady force (often called the Stokes drag), the stress-gradient force, the added-mass force, and the viscous-unsteady force (also known as the Basset history force). The Basset force arises from the viscous unsteady effect and the

temporal delay in the particle response. The delay is due to the time required for the boundary layer on the surface of the particle to adjust to the varying relative velocity [Traugott and Liberzon, 2017]. The computation of this term needs time-resolved data; hence, this term is often neglected in many investigations. It is also required to know the history of both particle and fluid acceleration for a sufficient time. This increases the memory requirement for numerical simulation of systems that involve large numbers of particles. Hence, the Basset term is usually neglected in numerical simulations. In the current study, this force is measured in a horizontal channel turbulent flow, and its correlation with the total acceleration of particles is investigated.

1.2 Objectives

This thesis aims to study particle-fluid interactions and the dispersion mechanism of particles in turbulent channel flows. Specifically, it is intended to

- study the turbulence modulation and investigate the effect of particle size, volumetric concentration, and flow Re on the velocity statistics of both phases;
- Evaluate particle concentration distribution for different turbulent events to identify mechanisms responsible for particle deposition and re-suspension;
- investigate the variation of local particle concentration in the wall region; and
- study the effect of quasi-steady and viscous-unsteady forces on the particle dynamics.

For this purpose, the instantaneous velocity of the particles and the carrier phase should be measured simultaneously. This allows for evaluation of the turbulence intensity of particles and the carrier phase, the velocity field around a particle, and particle dynamics. The investigations will be carried out over a wide range of flow Re, particle size, and particle concentrations to identify the effect of these conditions on the turbulence characteristics of particle-laden flows.

1.3 Thesis outline

This thesis includes 8 chapters; a brief description of each chapter follows.

Chapter 2 provides some essential background on turbulent channel flow and basic concepts about particle motion in turbulent flows.

Chapter 3 first describes the experimental setup used to carry out particle-laden flow experiments. The imaging setups and measurement techniques employed in this thesis are also detailed in this chapter. These techniques include planar particle image and tracking velocimetry (PIV/PTV) and time-resolved three-dimensional particle tracking velocimetry.

Chapter 4 provides a detailed investigation of the effects of flow Re, particle size, and particle volumetric concentration on the turbulence statistics of both phases. Distribution profiles of the coarse particles (glass beads) across the channel height are also presented in this chapter. The extent of turbulence modulation for different cases is calculated, and it is aimed to evaluate the modulation criterion established by Tanaka and Eaton [2008] at a higher range of Re.

Chapter 5 focuses on the interaction between the nearly neutrally buoyant beads and the fluid phase. The beads are sampled based on their wall-normal velocity, and the velocity field around the beads and distribution of the beads over different turbulent events are investigated. The pathlines of the beads in the near-wall region are inspected, showing the effect of streamwise vortices which generate considerable spanwise motion.

Chapter 6 investigates the distribution of the particles in the near-wall region in greater detail. The role of different mechanisms including shear-induced lift force and inter-particle collision is discussed in this chapter.

Chapter 7 investigates particle dynamics in solid-liquid turbulent flows. The acceleration of the beads is measured, and the contributions of the quasi-steady and viscous-unsteady forces are determined.

Chapter 8 summarizes findings of the present study. The chapter also contains a discussion of future works.

Chapter 2

Fundamentals of Turbulent and Multiphase Flow

One of the main sources of turbulence production is shear in the mean flow. Due to the no-slip condition at flow boundaries, there is a viscosity-dominant region near the wall [Tennekes and Lumley, 1972]. Once the vorticity has been generated, the flow can proceed to develop in the absence of the wall which is called free shear flow. The flows can also remain attached to the surface and develop under its influence. These flows are usually referred to as wall-bounded flows.

Wall-bounded flows constitute a major part of flows in industry and nature. Examples include external flows such as the atmospheric boundary layer and flow of rivers, and internal flows such as the flow through conduits. The main characteristics of single-phase turbulent flow in channels and particle motions in turbulent flows are described in this chapter.

2.1 Wall-bounded turbulent flows

We consider the flow between two parallel plates separated by a distance of h as shown in Figure 2.1. The mean flow is predominantly in the streamwise (x) direction, and the mean velocity varies in the wall-normal (y) direction. The flow is statistically independent of the spanwise (z) direction. The instantaneous velocities in the x, y, and z directions are U, V, and W, and the velocity fluctuations are denoted by u, v, and w, respectively. In this chapter, U_i and u_i are also used for instantaneous velocity and velocity fluctuation in i^{th}

direction (x_i).

There is a flow-development region at the entry of the channel. At distances farther from the entrance region, the velocity statistics no longer change with x, and the flow becomes fully-developed. Fully-developed channel flow is statistically stationary and one-dimensional since the velocity statistics only depends on the y location [Pope, 2000].

The channel flow can be characterized by the Reynolds number (Re):

$$Re = \frac{\rho U_b \, h}{\mu}, \tag{2.1}$$

where ρ is the fluid density, U_b is the bulk velocity (i.e. the mean velocity), and μ is the dynamic viscosity of the fluid. The flow is laminar for $Re < 1350$ and turbulent for $Re > 1800$; however, transitional effects may exist for Re up to 3000 [Patel and Head, 1969].

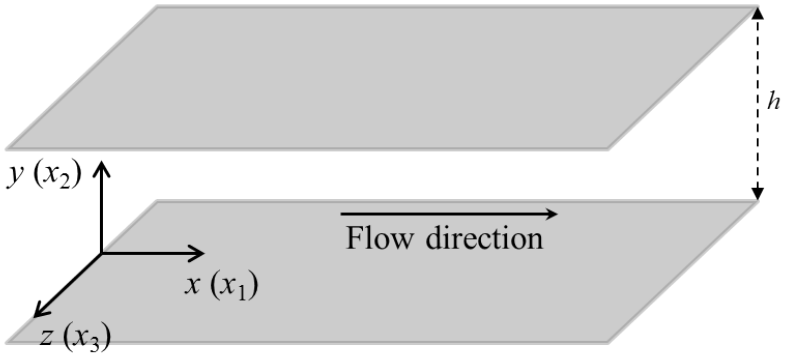

Figure 2.1: Schematic of a channel showing the coordinate system.

2.1.1 Governing equations

Using Cartesian tensor notation, the dynamical equation for a fluid can be written as

$$\frac{\partial U_j}{\partial x_j} = 0, \tag{2.2}$$

and

$$\rho \left[\frac{\partial U_i}{\partial t} + U_j \frac{\partial U_i}{\partial x_j} \right] = -\frac{\partial P}{\partial x_i} + \frac{\partial T^v_{ij}}{\partial x_j}, \tag{2.3}$$

where P represents the static pressure and T^v_{ij} is the tensor of viscous stress. The Einstein summation convention is employed in these equations. Equation 2.2 shows the

conservation of mass for an incompressible flow, and Eq. 2.3 is Newton's second law written for a continuum space. If the flow is incompressible and the fluid is Newtonian, the momentum equation reduces to [Davidson, 2015]

$$\frac{\partial U_i}{\partial t} + U_j \frac{\partial U_i}{\partial x_j} = -\frac{1}{\rho}\frac{\partial P}{\partial x_i} + \nu \frac{\partial^2 U_i}{\partial x_j^2}, \tag{2.4}$$

where $\nu = \mu/\rho$ is the kinematic viscosity.

2.1.2 Reynolds stresses

The instantaneous velocity can be decomposed into mean, indicated by the symbol $\langle\rangle$, and velocity fluctuations shown by the lower-case letters. The decomposition is expressed as $U_i = \langle U_i \rangle + u_i$. The pressure term is also decomposed as $P = \langle P \rangle + p$. Decomposition of the instantaneous motion is referred to as the Reynolds decomposition. Applying the Reynolds decomposition to Eq. 2.1 yields the relations

$$\frac{\partial \langle U_j \rangle}{\partial x_j} = 0, \tag{2.5}$$

and

$$\frac{\partial u_j}{\partial x_j} = 0, \tag{2.6}$$

for the mean velocity and velocity fluctuation. Applying the decomposition to the momentum equation results in

$$\rho \left[\frac{\partial \langle U_i \rangle}{\partial t} + \langle U_j \rangle \frac{\partial \langle U_i \rangle}{\partial x_j} \right] = -\frac{\partial \langle P \rangle}{\partial x_i} + \frac{\partial}{\partial x_j} \left[\mu \frac{\partial \langle U_i \rangle}{\partial x_j} - \rho \langle u_i u_j \rangle \right]. \tag{2.7}$$

The terms in the square bracket on the right have the dimension of stress. The first term is the viscous stress, and the second term is called the Reynolds stress. The total shear stress is the sum of the viscous and the Reynolds stresses. In a fully-developed channel flow, it can be written as [Pope, 2000]

$$\tau = \mu \frac{d\langle U_1 \rangle}{dx_2} - \rho \langle u_1 u_2 \rangle. \tag{2.8}$$

All the Reynolds stress components are zero at the wall; consequently, the shear stress is completely due to the viscous contribution. Since the wall shear stress (τ_w) and kinematic

viscosity are the dominant factors close to the wall, they can be used to define the velocity and length scales in the near-wall region. Accordingly, the shear or friction velocity is defined as

$$u_\tau = \sqrt{\frac{\tau_w}{\rho}}, \tag{2.9}$$

and the wall unit or viscous length scale is

$$\lambda = \frac{\nu}{u_\tau}. \tag{2.10}$$

The normalized distance from the wall is denoted by y^+ and calculated as

$$y^+ = \frac{y}{\lambda} = \frac{u_\tau y}{\nu}. \tag{2.11}$$

The magnitude of y^+ can represent the relative importance of viscous and turbulent processes.

2.1.3 Mean velocity profile

At high Reynolds numbers, there is an inner layer close to the wall where the mean velocity profile is determined by viscous scales independent of h and U_b [Prandtl, 1921]. It can be shown that [Pope, 2000]

$$\frac{d\langle U\rangle}{dy} = \frac{u_\tau}{y}\Phi_I\left(\frac{y}{\lambda}\right), \qquad \text{for } \frac{y}{h} \ll 1, \tag{2.12}$$

where Φ_I is a universal non-dimensional function. Equation 2.12 can be written in a non-dimensional form as

$$\frac{d\langle U\rangle^+}{dy^+} = \frac{1}{y^+}\Phi_I\left(y^+\right). \tag{2.13}$$

Here, $\langle U\rangle^+ = \langle U\rangle/u_\tau$. The integral of Eq. 2.13 is the law of the wall:

$$\langle U\rangle^+ = f_w\left(y^+\right). \tag{2.14}$$

The no-slip boundary condition on the wall and the normalized expression of wall-shear stress (Eq. 2.8) at $y = 0$ gives $f_w(0) = 0$ and $f'_w(0) = 1$. Therefore, the Taylor expansion of f_w for small y^+ can be expressed as

$$f_w\left(y^+\right) = y^+ + O\left(y^{+2}\right). \tag{2.15}$$

The inner layer is generally defined as $y/h < 0.1$. Viscosity has an insignificant effect at large values of y^+ in the inner layer. Hence, the dependence of Φ_I on ν vanishes in Eq. 2.12, and Φ_I becomes a constant value usually denoted by $1/\kappa$:

$$\Phi_I\left(y^+\right) = \frac{1}{\kappa}, \qquad \text{for } \frac{y}{h} \ll 1, \text{ and } y^+ \gg 1. \tag{2.16}$$

Accordingly, the velocity gradient in this region is

$$\frac{d\langle U\rangle^+}{dy^+} = \frac{1}{\kappa y^+}, \tag{2.17}$$

which yields

$$\langle U\rangle^+ = \frac{1}{\kappa}\ln\left(y^+\right) + B, \tag{2.18}$$

where B is a constant and κ is the von Kármán constant. Equation 2.18 describes the logarithmic law of the wall. The constants can roughly be expressed as $B = 5.2$ and $\kappa = 0.41$.

2.2 Transport of particles in turbulent flow

2.2.1 Momentum coupling

The first analytical solution for flow passing a sphere at low Re was given by Stokes [1851]. Subsequently, Basset [1889], Boussinesq [1895] and Oseen [1927] investigated the motion of a spherical particle falling in a quiescent fluid. The equation of motion for spherical particles is called BBO (Basset-Boussinesq-Oseen) equations in the literature. Maxey and Riley [1983] performed a detailed analysis of motion of small particles in a non-uniform and unsteady flow. They introduced gravity, drag force due to the pressure gradient of the flow undisturbed by the presence of the particle, quasi-steady force, apparent mass force, and Basset force as the main source of particle acceleration. A brief description of each term is provided here.

Quasi-steady force: The term is called quasi-steady since it refers to the force when the relative velocity between the particle and fluid phase does not change significantly with time. In order to incorporate the effects of Re, the quasi-steady force is usually written as

$$F_{qs} = 3\pi\mu d_b f_d(u_i - v_i), \tag{2.19}$$

where F_{qs} stands for quasi-steady force and f_d is the drag factor. The drag factor can safely be considered to be unity in creeping flow ($Re < 1$). However, it starts to deviate from the Stokes law as the Re increases. There are several correlations available in the literature for f_d. The following correlation provided by Schiller and Naumann [1933] and predicts f_d within 5% of the experimental results for Reynolds number up to 800:

$$f_d = 1 + 0.15 Re_p^{0.687}. \tag{2.20}$$

Here, Re_p is the particle Reynolds number which is calculated based on the relative velocity between the fluid and particle, i.e., $u_i - v_i$. The compressibility and rarefaction effects also affect F_{qs}, but these are not applicable in the current study.

Virtual or apparent mass force: When a particle accelerates through a fluid, the kinetic energy of the surrounding fluid changes. This change in the fluid kinetic energy occurs at the expense of work done by the particle. This additional work is associated with the virtual or apparent mass drag force. It can be shown that for a potential flow around a sphere, this force is equal to

$$F_{am} = \frac{1}{2} m_f \frac{d}{dt}(u_i - v_i). \tag{2.21}$$

Basset force: This force accounts for the viscous effects of unsteady flow around a particle. This term is also called the viscous-unsteady force. This force arises due to the temporal delay in the development of a boundary layer around the particle when the relative velocity between the particle and fluid phase changes.

The analytical solution of flow above an infinite plane due to a sudden acceleration in the plane revealed that the wall effect diffuses into the fluid at a rate proportional to $\sqrt{\nu t}$. Here, t is time, and $t = 0$ refers to the time when the sudden acceleration initials. The thickness of the shear layer also varies with $\sqrt{\nu t}$. This is similar to a conducting solid when its bottom temperature suddenly changes [White, 2006]. Considering a sudden change equal to Δu_0 in the velocity of the bottom plane, the shear stress changes with time as

$$\tau(t) = \frac{\sqrt{\rho\mu}\Delta u_0}{\sqrt{\pi t}}. \tag{2.22}$$

Any general variation in the velocity of the bottom plane can be broken into a series of stepwise changes as shown in Figure 2.2. Superposition gives the shear stress at time t as

$$\tau(t) = \sqrt{\frac{\rho\mu}{\pi}} \left[\frac{\Delta u_0}{\sqrt{t}} + \frac{\Delta u_1}{\sqrt{t-t_1}} + \frac{\Delta u_2}{\sqrt{t-t_2}} + \cdots \right]. \tag{2.23}$$

For a very small time step $\Delta t'$, the change in the velocity would be $du/dt'\Delta t'$. As $\Delta t'$ approaches zero, the summation in Eq. 2.23 becomes

$$\tau(t) = \sqrt{\frac{\rho\mu}{\pi}} \int_0^t \frac{\frac{du}{dt'}}{\sqrt{t-t'}} dt'. \tag{2.24}$$

Applying the same approach to a small spherical particle accelerating in a fluid at low Reynolds number gives the Basset drag force:

$$F_{vu} = \frac{3}{2} d_b^2 \sqrt{\pi\rho\mu} \int_0^t \frac{\frac{d}{dt'}(u_i - v_i)}{\sqrt{t-t'}} dt'. \tag{2.25}$$

In this equation, $\frac{1}{\sqrt{t-t'}}$ is the so-called Basset kernel which is accurate at $Re < 1$. The Basset kernel was extended by Mei and Adrian [1992] to finite Reynolds numbers using

$$K_B(t-\tau) = \left\{ (t-\tau)^{1/(2c_1)} + \left[\sqrt{\frac{\pi}{\nu}} \frac{|u_i - v_i|^3 (t-\tau)^2}{2\nu f_h} \right]^{1/c_1} \right\}^{-c_1}, \tag{2.26}$$

where

$$f_h = \left[0.75 + c_2 \left(\frac{d_b |u_i - v_i|}{\nu} \right) \right]^3. \tag{2.27}$$

The constants $c_1 = 2$ and $c_2 = 0.105$ were proposed by Mei and Adrian [1992]. The kernel expressed in Eq. 2.26 suggests that it decays at a rate proportional to $t^{-1/2}$ at short-time periods, and decays at a faster rate of t^{-2} at long-time periods.

2.2.2 Response times

The response time of a particle to the changes in flow velocity is an essential parameter that characterizes the motion of a particle suspended in a flow. Based on Stokes law, the velocity of an initially stationary particle in a flow with uniform velocity of u_0 changes as

$$v(t) = u_0(1 - e^{-t/\tau_b}), \tag{2.28}$$

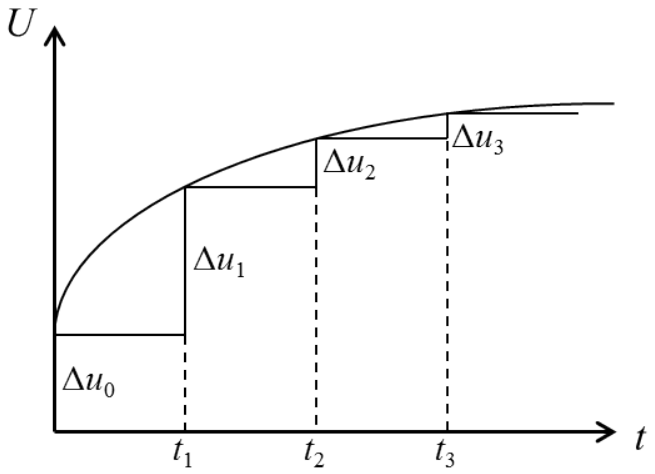

Figure 2.2: Successive stepwise change in the velocity of the bottom plane.

where τ_b is the bead response time:

$$\tau_b = \rho_b d_b^2 / 18\mu \tag{2.29}$$

which is the time required for a stationary particle released in a uniform flow to reach 63% of the free stream velocity. The factor introduced in Eq. 2.20, $f_d = 1 + 0.15 Re_p^{0.687}$, is usually included to correct the deviation from Stokes law when the particle Reynolds number is too large to follow Stokes law, and the response time becomes $\tau_b = \rho_b d_b^2 / 18\mu f_d$. Here, Re_p is calculated based on the terminal settling velocity

$$V_s = \frac{1}{18\mu f_d} d_b^2 g \left(\rho_b - \rho_f\right). \tag{2.30}$$

It was noted that the time response in Eq. 2.29 is derived by considering only the quasi-steady force (Stokes drag) on the particle. This assumption is valid in gas-solid flows where unsteady forces are negligible. However, in liquid-solid flows the unsteady forces are significant and affect the particle dynamics. A simple way to account for the effect of the apparent mass force is to replace ρ_b with $\rho_b + \rho_f/2$ in Eq. 2.29 [Minier and Pozorski, 2017].

The ratio of particle to fluid time scales is called the Stokes number, $St = \tau_b / \tau_f$, which characterizes the particle-laden flow behavior. If $St \ll 1$, the particle responds quickly to changes in the flow. Hence, the particles follow all the motions in the flow field. On the

other hand, the particles do not respond to flow changes if $St \gg 1$.

Different characteristic time scales can be considered for the flow. The viscous time scale, $\tau_v = \nu/u_\tau^2$, estimates the characteristic time scale of the flow near the wall. In this region, flow time scale is smaller and the St has larger value than for the central region of the flow. The integral and Kolmogorov time scales are also used in the literature to calculate the St at the channel centerline. The integral time scale, τ_L, can be estimated using dimensional analysis [Tennekes and Lumley, 1972]

$$\tau_L = \frac{1}{3}\frac{\langle u^2 \rangle}{\epsilon}, \tag{2.31}$$

where ϵ is the turbulence dissipation rate at the channel centerline. The Kolmogorov time scale, τ_K, is defined as

$$\tau_K = \left(\frac{\nu}{\epsilon}\right)^{1/2}. \tag{2.32}$$

The dissipation rate is calculated using [Milojević, 1990]

$$\epsilon = C_\mu^{0.75}\frac{k^{1.5}}{l_m} \tag{2.33}$$

where $C_\mu = 0.09$ and $l_m = 0.14h$ [Schlichting and Gersten, 2017]. The turbulent kinetic energy k is calculated using ensemble averages of velocity fluctuations:

$$k = \frac{1}{2}\left(\langle u^2 \rangle + \langle v^2 \rangle + \langle w^2 \rangle\right). \tag{2.34}$$

2.2.3 Particle transport near the wall

Particle transport in the near-wall region is dominated by the dynamics of turbulent structures. Numerous flow visualization experiments revealed existence of streaks near the wall [Kline et al., 1967]. The streaks correspond to the regions with velocity smaller than the mean flow while the fluid between streaks is fast moving [Pope, 2000]. At some point, the streak moves away from the wall which is called ejection of low-speed fluid. Corino and Brodkey [1969] also identified regions of high-speed fluid moving toward the wall which is called sweep events. Ejections and sweeps control the momentum transfer and also affect the transfer of particles near the wall.

The mechanism that generates and maintains ejection and sweep events is not identified accurately. It is believed that quasi-streamwise vortices generate ejections and sweeps. These vortices have a characteristic length of about 200 wall units separated by a distance of about 400 wall units [Kline et al., 1967, Jiménez and Pinelli, 1999]. These vortices are also tilted away from the wall by an average angle of about 9°and inclined slightly to the left and right. Regions located between two vortices at the upwash side are characterized by a streamwise velocity lower than the mean flow. In comparison, the regions at the downwash side of vortices are characterized by a streamwise velocity larger than the mean velocity. Low-speed streaks are longer than quasi-streamwise vortices with a length of around 1000 wall units. A single low-speed streak is usually surrounded by many quasi-streamwise vortices [Minier and Pozorski, 2017]. In summary, the turbulence in the near-wall region is dominated by the slow-speed and high-speed streaks generated by counter-rotating quasi-streamwise vortices. These vortices are known to be the most usual vortical structures near the wall.

Particles are not distributed uniformly in the near-wall region. It has been shown that the particles accumulate preferentially in the low-speed regions [Nino and Garcia, 1996, Pan and Banerjee, 1996]. A correlation was also observed between the particle flux toward the wall and sweep events, and between particle flux away from the wall and ejection events. The correlation is significant for particles of small St, and reduces with the increase of St. This means there is a chance of finding large particles moving away from (or toward) the wall while surrounded by a non-ejection (or non-sweep) event.

The action of ejection motions is effective in the suspension of particles in turbulent flows. Sumer and Oguz [1978] used a photographic technique to record the trajectory of inertial particles. They found that the ejection motion of the liquid phase transports particles away from the wall and generates a negative streamwise velocity fluctuatio [Sumer and Oguz, 1978, Rashidi et al., 1990, Ji et al., 2013]. Once the ejection motion weakens, the suspended particles gradually approach the wall. The particles may be lifted up again by another ejection motion and remain suspended in the flow.

2.3 Particle-particle interaction

Turbulence is the main source of particle-particle collisions. Gravitational sedimentation, the action of molecular forces, and Brownian motion are among the other mechanisms that cause a particle to collide with another one. Determining the collision frequency of liquid droplets or solid particles is of interest in investigation of two-phase systems. The collision frequency, f_c, in a system with a large number of particles is proportional to the particle number density, n, which is the number of particles in a unit volume:

$$f_c = \beta n. \tag{2.35}$$

Here, β (m^3/s) is called the collision kernel. Early models of inter-particle collision were developed for turbulent flows with low energy dissipation [Camp, 1943, Saffman and Turner, 1956]. In these flows, even the smallest eddies are large enough to confine a particle. Hence, the paths of the particles were fully determined by the eddy fluid velocities and accelerations [Abrahamson, 1975]. Saffman and Turner [1956] presented the first formulation of a collision kernel in this type of flow which works perfectly for zero-inertia particles. The collision kernel based on the spherical formulation is

$$\beta_{sph} = 2\pi R^2 \langle |v_r| \rangle. \tag{2.36}$$

The spherical kernel actually describes the inward flow rate of the fluid across the surface of the collision sphere as shown in Figure 2.3a. In Eq. 2.36, v_r is the radial component of relative velocity between two particles approaching each other. In a monodispersed system $R = d_b$.

In cylindrical formulation, the collision kernel describes the volume of a cylinder passing through a particle with cross sectional area of πR^2 and length of $|w|$ per unit time as presented in Figure 2.3b. The collision kernel is then

$$\beta_{cyl} = \pi R^2 \langle |w| \rangle, \tag{2.37}$$

where $|w|$ is the magnitude of the relative velocity. This is different from v_r which stands for the radial component. It should be noted that the $\langle\rangle$ operator in Eqs. 2.36 and 2.37

averages the velocity in all direction and in time. Hence, both kernel formulae are developed for stationary and isotropic turbulent flow.

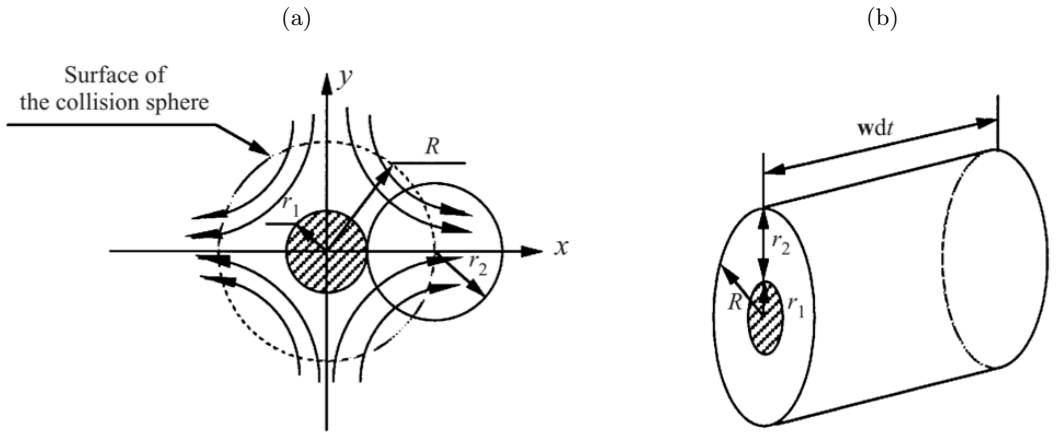

Figure 2.3: Geometrical description of (a) spherical and (b) cylindrical formulation of collision kernel.

In flows with much higher energy dissipation, the smallest eddy becomes smaller. Hence, a particle usually transfers momentum with more than one eddy, and the models for low dissipation turbulence become invalid. When the particles have considerably larger time scale than the flow time scale, it can be assumed that the motion of particles are not correlated. In this case, the velocity of particles become statistically independent which is similar to the motion of molecules in the kinetic theory of gases. The collision kernel for high-inertia particles provided by Abrahamson [1975]:

$$\beta = 4\pi^{1/2}\frac{2k_b}{3}R^2, \tag{2.38}$$

where k_b is the turbulent kinetic energy of particles, and R is collision radius. Similar to the previous relations, $R = d_b$ for monodispersed particles. It is shown that the assumption of independent particle velocities is suitable for high intensity turbulence in suspensions being pumped or mixed under industrial conditions [Abrahamson, 1975].

The basic concepts of turbulence in channel flows, particle response to the flow, and momentum transfer between the particles and fluid phase were introduced in this chapter. These concepts will be used in the rest of the thesis to explain the flow conditions and

interpret the results.

Chapter 3

Experimental Setup and Measurements

A horizontal slurry flow loop was used to perform experiments in the current research. The flow loop contained a channel section, and the measurements were conducted in this section of the loop. Glass beads with density (ρ_p) of around 2.60 gr/cm^3 and polystyrene spherical beads with ρ_p = 1.05 gr/cm^3 of different sizes and at different concentrations were used to produce suspensions. More details about the flow loop are provided in this chapter. Different sets of velocity measurements were conducted in this research. The first one was a two-dimensional particle image/tracking velocimetry (PIV/PTV) which was performed to study the effect of particle size and flow Re on the velocity statistics of the dispersed and carrier phases. This technique is detailed in Section 3.2 and the related results are presented in Chapter 4. Two sets of three-dimensional PTV measurements, based on the shake-the-box algorithm [Schanz et al., 2016], were also carried out. These measurements are explained in Sections 3.3 and 3.4, and the related results are presented in Chapters 5 to 7.

3.1 Slurry flow loop

The experiments were performed in a horizontal slurry flow loop equipped with a centrifugal pump (LCC-M, GIW Industries Inc.) which can circulate up to 2 m^3/min of unladen water. The schematic of the flow loop is displayed in Figure 3.1. The test section had a rectangular

cross-section of 120 mm width and 15 mm height (h). The channel windows were made of glass with high quality surface finish of 0.7 µm, which can be considered as a smooth surface. The flow rate was measured using a Coriolis flow meter (Micro Motion, F-series) with mass flow accuracy of ±0.10% of the measured flow rate. The centrifugal pump was controlled by a variable frequency drive (A510, Teco Electric & Machinery Co., Ltd.) to hold the flow rate constant during each experiment. The standard deviation of the time series of the flow rate data was less than 0.03% of the average flow rate. The flow loop utilized two data acquisition cards (NI 9211 and 9263, National Instruments) to record the mass flow rate, temperature and mixture density at a sampling rate of 1 Hz, and to control the variable frequency drive. A double-pipe heat exchanger was used to keep the fluid temperature constant during the experiments. The test section was 2.5 m long; the measurements were made at a distance of 1.65 m (220 h) downstream of the channel entrance (as indicated in Figure 3.1) to ensure fully developed flow.

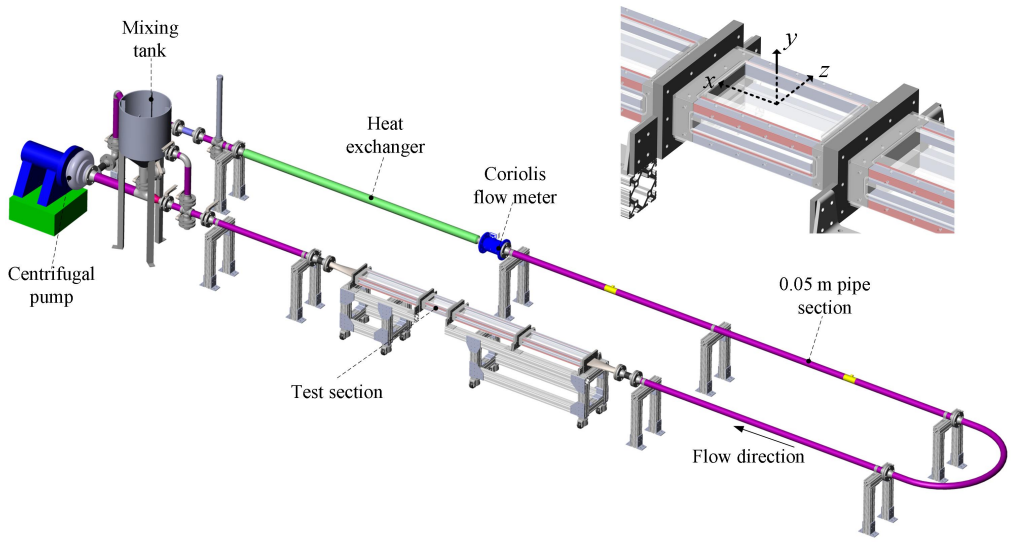

Figure 3.1: Schematic of the flow loop demonstrating its main components. The inset shows the test section and the streamwise (x), wall-normal (y), and spanwise (z) directions. The origin of the coordinate system is on the bottom wall of the channel.

3.2 Two-dimensional PIV/PTV

A combined PIV and PTV method was applied to measure the velocity of the glass beads and the carrier liquid phase from a common set of images. Methods based on fluorescence tagging [Sridhar and Katz, 1995], intensity discrimination [Anderson and Longmire, 1996], phase dynamics [Delnoij et al., 1999], and geometrical characteristics [Hassan et al., 1992] have been used to discriminate the smaller tracers of the liquid phase from the larger beads (i.e., the solid phase) in image-based measurements. There are specific challenges and limitations associated with each of these methods. For example, fluorescence tagging requires a substantial amount of fluorescent particles for a large-scale experimental setup such as the flow loop used here. Khalitov and Longmire [2002] used the size and intensity of tracers to distinguish them from larger and brighter particles. Kiger and Pan [2000] used a two-dimensional median filter to separate images of particles and tracers. The median filter increases the intensity difference of the tracers and dispersed particles to apply a phase discrimination algorithm. An algorithm based on that of Kiger and Pan [2000] was used to separate the tracers and the glass beads in the images.

The measurement setup is shown in Figure 3.2. Images were captured using two CCD cameras (Imager Intense, LaVision, GmbH), each with a sensor size of 1040 $\times$ 1376 pixel, arranged side-by-side to cover a larger streamwise portion of the channel for improved statistical convergence. Each pixel of the CCD is 6.45 $\times$ 6.45 μm^2 with 12-bit digital resolution. A Nd:YAG laser (New Wave Research, Solo PIV III) with maximum pulse energy of 50 mJ over 3–4 ns pulse width at 532 nm wavelength was used for illumination. The laser beam was directed into a combination of two spherical lenses and a cylindrical lens to form a 1 mm-thick laser sheet, which illuminates an x–y plane in the mid-spanwise section of the channel. The cameras were equipped with SLR lenses (Sigma) with focal length of $f = 60$ mm at an aperture diameter of $f/16$. Each camera lens was aligned normal to the laser sheet and sidewalls to minimize astigmatism and variation of magnification in the images. The field of view (FOV) of each camera was 11.8 mm by 15.5 mm along the x and y directions, respectively. Overall, for the imaging system, the magnification and digital

resolution were 0.57 and 88 pixel/mm, respectively. The estimated depth-of-field was about 5 mm, which was greater than the laser sheet thickness. The cameras were synchronized with the laser using a programmable timing unit (PTU9, LaVision, GmbH) controlled by DaVis 7.4 (LaVision, GmbH), acquiring double-frame images at a sampling rate of 3 Hz. The particle displacement between two consecutive frames was set to 20 pixels by adjusting the time interval between the two laser pulses. A large ensemble of 60,000 double-frame images of the two-phase flow was captured for each experimental condition. The images included the glass beads and the liquid phase seeded with the 2 µm silver-coated glass beads (SG02S40 Potters Industries) with a density of 4 gr/cm^3. This large number of images was necessary to capture a sufficient number of particles for improved statistical convergence of PTV results. Only 8000 double-frame images were used for the liquid phase PIV results.

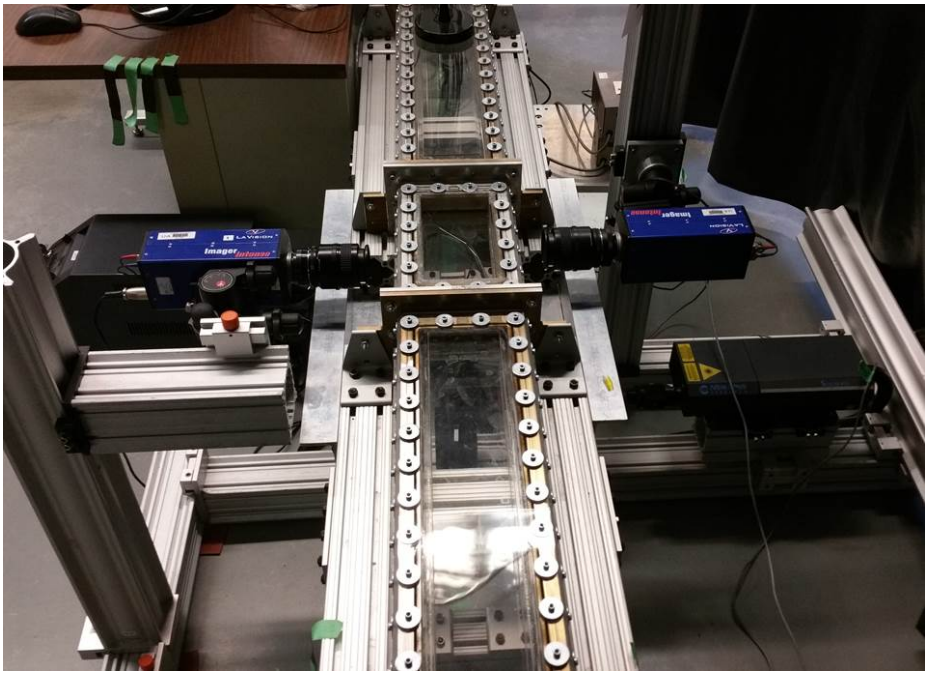

Figure 3.2: The setup used for two-dimensional PIV/PTV.

The PTV algorithm detected and tracked the large glass beads in the double-frame images. The diameter of glass beads in the images varied from 25 pixels for 285 µm particles to 60 pixels for particles of 700 µm in diameter. The glass beads in the two-phase images were detected using the 'imfindcircle' function in MATLAB (R2015a, MathWorks). This

function uses the circle Hough transform to find the circle center and radius [Atherton and Kerbyson, 1999]. The beads with average intensity below a threshold value were considered out of the laser sheet and the information was discarded. A sample of two overlapped frames with the detected glass beads is shown in Figure 3.3a. A tracking script developed in MATLAB was used to search for the particle in an area specified by a search radius (20 pixels for 285 µm and 30 pixels for 700 µm particles) around the predicted position in the second frame. The particle position in the second frame was predicted using an averaged velocity field obtained from an ensemble of the correlation maps [Meinhart et al., 2000]. In the next step, two interrogation windows were placed around the particle pair in the first and the second frames as demonstrated in Figure 3.3b and c. The interrogation windows were cross-correlated to obtain the displacement of the bead. The area around the perimeter of the glass bead in the first frame was cleared and filled with random noise to minimize the impact of tracers in the cross-correlation. A cross-correlation coefficient with a threshold of 0.85 was used to filter out the pairs that did not have a similar pattern. The wall-normal direction was divided into 150 pixels (2 mm) bins with 50% overlap for calculation of the particle mean velocity profile and turbulence statistics. The error analysis for the PTV results of the particles is provided in Section 4.5. The rms of measurement uncertainty is around 30.0 mm/s for the mean velocity and is in the order of 10^{-5} for turbulence intensities.

A PIV algorithm was applied to the two-phase images to obtain the velocity of the liquid phase surrounding the glass beads. The background noise was first removed by subtraction of the minimum intensity of the ensemble of images in order to reduce the laser glare from the wall and stationary image features [Raffel et al., 2007]. A median filter was then applied for phase discrimination and to mask out the glass beads. The filter reduced the intensity of the tracers while the intensity of glass beads remained almost constant. This is indicated in the inverted images of Figures 3.4a and 3.4b. The image intensity is inverted here for image clarity. The pixels with intensity above a threshold (dark areas in the inverted image) are the glass beads, which are excluded from the cross-correlation algorithm. The kernel size

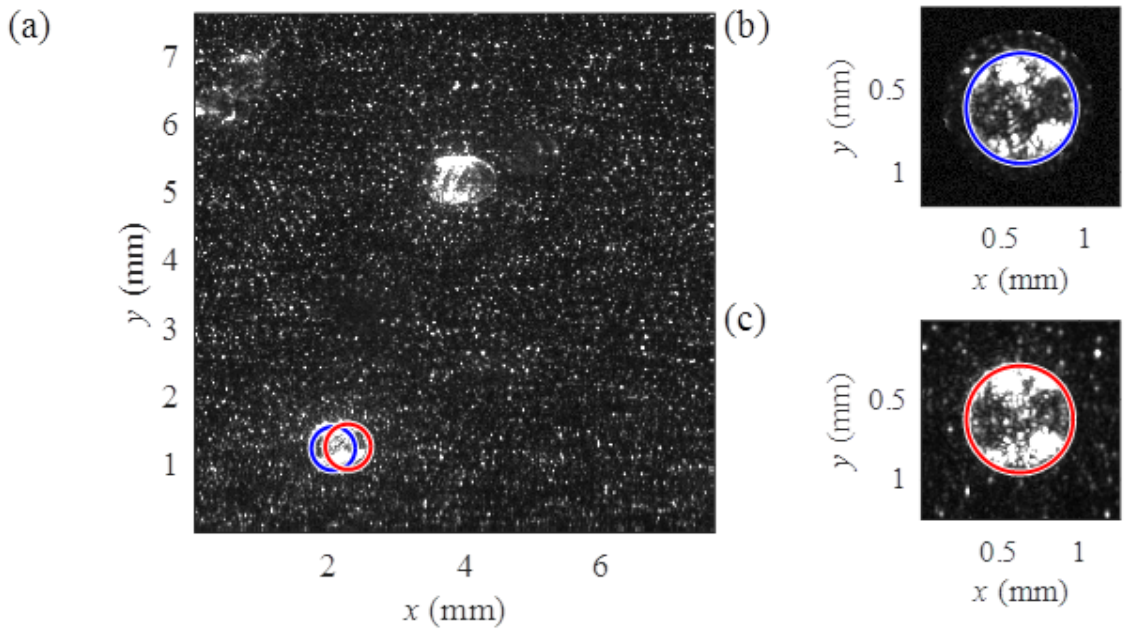

Figure 3.3: (a) A sample image of two superimposed frames. The detected pair of glass beads is specified in blue (first-frame) and red (second-frame). (b) The interrogation window around the glass bead of the first frame. The perimeter of the glass bead is filled with random noise. (c) Interrogation window around the glass bead in the second frame includes the surrounding tracer particles.

of the median filter depends on the size of the glass beads, but was about 25 × 25 pixel in the measurements made in the current study.

A multi-pass PIV was applied in Davis 8.3 (LaVision, GmbH) to the images with masked-out particles to obtain the fluid phase velocity. The first correlation pass applied an interrogation window size of 128 × 128 pixel and 50% overlap. The window size was reduced to 16 × 16 pixel (0.18×0.18 mm^2, $0.012h \times 0.012h$) and 75% overlap in the final cross-correlation pass. The instantaneous vector field obtained from the sample image is shown in Figure 3.4c. The white areas represent the pixels occupied by the glass beads. The interrogation windows that contained a masked-out area larger than 1% of the window area were rejected to ensure no bias occured in liquid phase velocimetry. The results of the measurements detailed in this section are presented in Chapter 4.

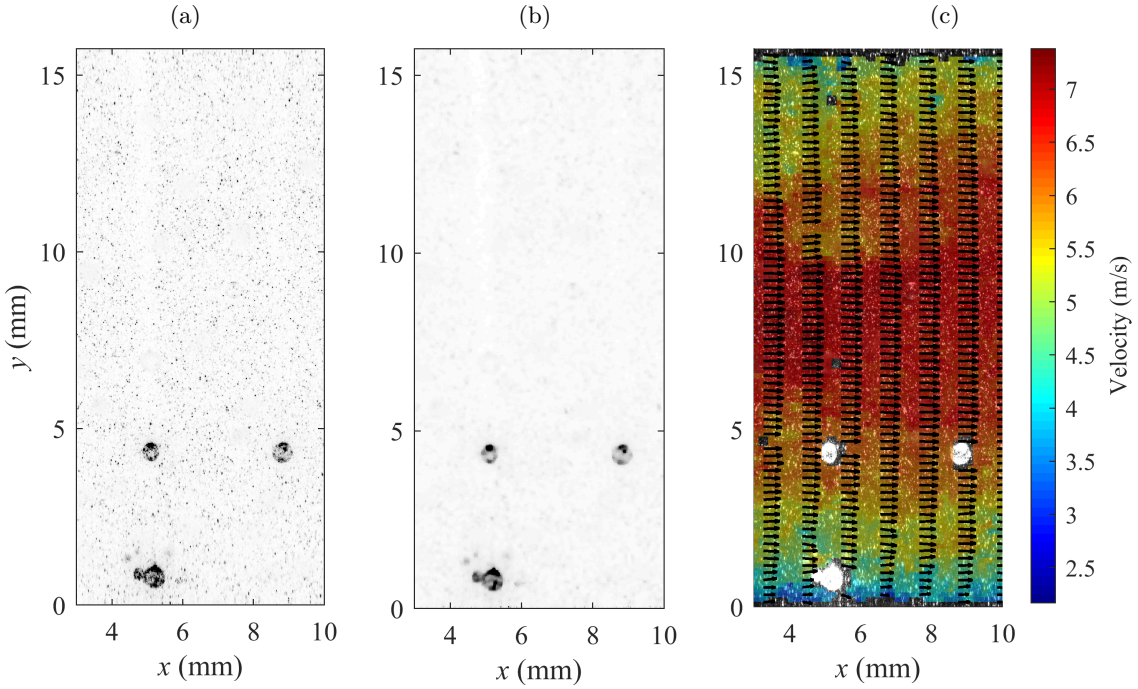

Figure 3.4: (a) A sample inverted image after subtracting the sliding minimum. (b) The image after applying the median filter to enhance the contrast of the large glass beads. (c) The velocity field of the liquid phase obtained from the cross-correlation algorithm.

3.3 Time-resolved three-dimensional PTV

This section provides the details about the measurement system used for the study presented in Chapter 5. A three-dimensional imaging system was used to simultaneously record time-resolved images of the particle-laden flow from four viewing angles. To distinguish the fluid tracers (2 µm) from the beads (370 µm), a median filter was applied to the images to increase their intensity contrast [Kiger and Pan, 2000]. Using a threshold intensity, the filtered images were decomposed to two sets: images of the tracers and images of the beads. To obtain 3D trajectories of the tracers and the beads, the two image sets were processed using a Lagrangian 3D particle tracking velocimetry based on the shake-the-box (STB) method [Schanz et al., 2016]. This method enabled us to obtain simultaneous 3D measurements of both the solid and fluid phase velocities.

The measurement volume was illuminated using a dual-cavity Nd:YLF laser (Photonics

Industries, dual-head DM-527 series) with a maximum energy of 20 mJ per pulse at a wavelength of 527 nm. The laser beam was expanded and collimated into an 8-mm-thick sheet in the y direction and a width of 60 mm in the x direction. The laser sheet entered the channel along the z axis through the sidewall, as shown in Figure 3.5. A mirror was located normal to the illumination direction (z axis) to reflect the light back into the test section to amplify the light intensity and to reduce the intensity difference between the forward and backward scattering cameras [Ghaemi and Scarano, 2010]. Knife-edge filters were attached to the sidewalls to remove the low-energy edges of the laser sheet and to obtain a relatively top-hat intensity profile.

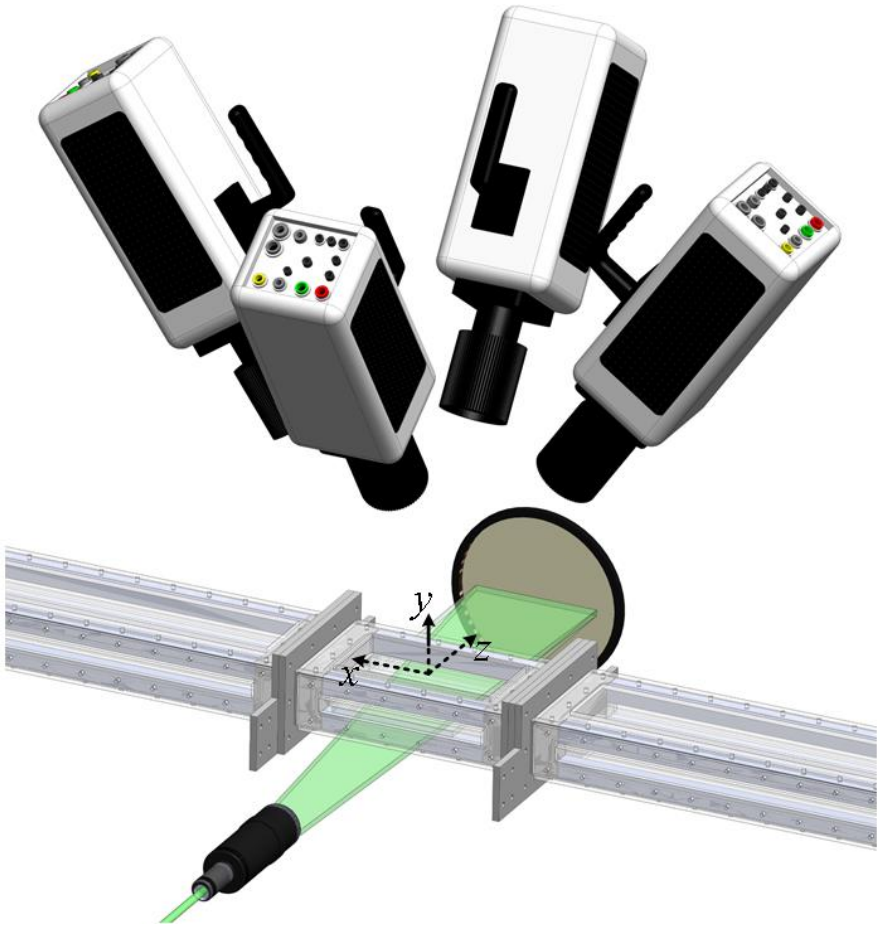

Figure 3.5: Schematic of the four cameras and the laser sheet with respect to the channel and the coordinate system.

The imaging system consisted of four high-speed CMOS cameras (Phantom v611) with a sensor size of 1280 $\times$ 800 pix. Each pixel of the CMOS sensor is 20 $\times$ 20 m^2 with 12-bit resolution. As shown in Figure 3.5, the cameras imaged the measurement volume from the top of the test section through the glass window. The cameras were arranged in a pluslike configuration at a working distance of $\sim$35 cm. The aperture angle, defined as the angle between two opposing cameras, was 65°. A camera lens with a focal length of f = 105 mm (Sigma) was connected to each camera using a lens-tilt adapter (Scheimpflug). The aperture size of each lens was set to $f/22$ to decrease any astigmatism effect on the particle images. The estimated depth-of-focus was 12 mm, which covered the thickness of the laser sheet. The magnification of each camera was 0.43 with a digital resolution of 22 pix/mm, which resulted in a measurement volume of 60 $\times$ 8 $\times$ 40 mm^3 in the x, y, and z directions, respectively. Using a high-speed controller (HSC v2, LaVision GmbH), the cameras were synchronized with the laser to acquire single-frame images at 6000 Hz. Five sets of 5500 time-resolved images were collected.

The initial calibration of the imaging system was performed using a dual-plane 3D calibration plate and the application of a third-order polynomial mapping function [Soloff et al., 1997]. The root mean square (rms) of the fit error was less than 0.25 pix on both planes of the 3D target. The remaining calibration error was corrected using the volumetric self-calibration technique [Wieneke, 2005, 2008]. The volume self-calibration process was repeated several times to obtain a mean disparity of 0.026 pix with the standard deviation of 0.017 pix in the entire domain.

To reduce background noise, the minimum intensity of all the images was subtracted from each image, and the images were also normalized using the average intensity of the data set. The signal-to-noise ratio was further improved by subtracting a sliding minimum over a kernel of 30 $\times$ 30 pix and local normalization by the average intensity in a kernel of 50 $\times$ 50 pix. To separate the beads from the tracers, a 6 $\times$ 6 pix median filter was applied. This filter reduced the intensity of the small tracers ($\sim$3 pix), but it had a negligible effect on the intensity of the beads ($\sim$8 pix). An intensity threshold was then used to obtain

Table 3.1: Summary of the 3D-PTV system specifications.

Magnification	Digital resolution (pix/mm)	Acquisition frequency (kHz)	Field of view (mm^3)	Image diameter (pix)		Particle Image density (ppp)	
				tracers	beads	tracers	beads
0.43	0.22	6	$60 \times 40 \times 8$	3	8	0.035	0.005

a mask identifying the high-intensity glass beads. The mask was applied to generate two sets of images for the beads and tracers based on the initial images (i.e., before applying the median filter). A Gaussian filter with a kernel of 7×7 pix was applied to the bead images to obtain a Gaussian intensity distribution. The volumetric concentration of beads resulted in an image number density of 0.005 particle per pixel (ppp), while the density of fluid phase tracers was 0.035 ppp. To evaluate the uncertainty of the measurement system and characterize the turbulent channel flow, unladen flow measurements were also carried out at a particle number density of 0.04 ppp. It was observed that the measurements had a maximum uncertainty of $0.15u_\tau$ (0.03 pixels) at $y^+ > 15$. A summary of measurement specifications is provided in Table 3.1.

To obtain the optical transfer function (OTF) for the STB algorithm [Schanz et al., 2016], the measurement domain was divided into $15 \times 8 \times 9$ subvolumes in the x, y, and z directions, respectively. In the OTF process, an elliptical Gaussian model is fitted to the particle shape for each subvolume to include the distortion effects from astigmatism and blurring [Wieneke, 2013]. The fit area used for calculation of the OTF was 11×11 pix for the beads and 3×3 pix for the tracers. The STB algorithm initiates particle tracking by detecting local intensity peaks. A maximum triangulation error of 1.0 and 0.5 pix was applied to the beads and the tracers, respectively. Particle pairs with spacing smaller than 2.0 pix were removed in the STB algorithm. For each image, the STB method performs an iterative triangulation process (also called an outer loop) to detect particles that enter the domain. The position and intensity of all detected particles were updated through another iterative process (inner loop) that shakes the particles around the predicted position by 0.1 pix to find the optimal position [Schanz et al., 2016]. Four outer loop iterations, followed by eight shaking iterations of the inner loop, were applied. The maximum displacement

of particles between two successive frames was around 5 pix, and the allowable maximum particle shift was limited to 8.0 pix. Calculation of OTF and particle tracking was performed in Davis 8.4 (LaVision GmbH).

To increase particle positioning accuracy, a second-order polynomial was fitted to the time series of particle positions (particle tracks) through a weighted linear least-squares ('rloess') function (R2015a, MathWorks), as also applied by van Hout [van Hout, 2011] and Oliveira et al. [Oliveira et al., 2013]. A polynomial kernel size of 40 time steps (equal to 6.6 ms) was applied to the beads and kernel of 20 time steps (3.3 ms) for the fluid phase. Using the relation given by Milojević [Milojević, 1990] and Schlichting and Gersten [Schlichting and Gersten, 2017] for a turbulent channel flow, the Kolmogorov timescale (τ_K) is 6.0 ms, which is greater than the 3.3 ms kernel size. This ensures that only measurement noise or turbulence fluctuations with negligible energy are filtered out. A larger kernel size was used for the beads since they have a longer response time than the fluid phase. The velocity and acceleration of the particles were also obtained from the coefficients of the second-order polynomial.

3.4 Measurement setup for relatively dense flow

The apparatus introduced in the previous section is used again to acquire time-resolved images of the glass beads suspended in relatively dense flows. The high-speed cameras were arranged in a pluslike configuration as shown in Figure 3.6. The cameras were placed underneath the channel to reduce the blockage by the glass beads in the line-of-sight of the cameras. This enables performing the measurements at larger bead concentrations. The results related to this section are presented in Chapters 6 and 7.

The cameras were placed at a working distance of approximately 30 cm and at an angular aperture of 70°, defined as the angle between two opposing cameras. Four camera lenses with a focal length of $f = 60$ mm were connected to the cameras using lens-tilt adapters (Scheimpflug) to have the whole image in focus. An aperture size of $f/11$, which resulted in an approximate depth-of-focus of 8 mm, was used to cover the entire thickness

of the illuminated volume. The digital resolution of each camera was 90.9 µm/pix at a magnification of 0.22. The dual-cavity Nd:YLF laser (Photonics Industries, dual-head DM) was used to illuminate the measurement volume. A combination of cylindrical and spherical lenses with a beam expander was employed to expand and collimate the laser beam in to a sheet that entered the channel in the z axis direction. The laser sheet was also reflected back to the test section by a mirror located normal to the illumination direction as seen in Figure 3.6. To obtain a top-hat intensity profile, knife-edge filters were used to remove the low-energy edge of the laser sheet. This resulted in a sheet with 3 mm thickness in the wall-normal direction, y, and 80 mm width in the streamwise, x, direction. This system resulted in a measurement domain with dimensions of $80\times3\times55$ mm^3 in x, y, and z directions, respectively. The diameter of glass beads in the images was around 3 pix, and the particle density in the images was less than 0.05 particle per pixel (ppp) for all the volumetric concentrations investigated here. The images were processed using 3D-PTV introduced in the previous section.

Thirty sets of 400 time-resolved single-frame images were acquired for each flow condition. The bead displacement between two consecutive frames was set to $\sim$4 pix using an acquisition frequency of 2,300 Hz for the bulk Re = 20,000, 4,200 Hz for Re = 40,000, and 6,000 Hz for Re = 60,000. The total duration of the collected images was $370h/U_{avg}$, $405h/U_{avg}$, and $420h/U_{avg}$ for the smallest to the largest Re.

The minimum intensity of the ensemble of images was subtracted from each image to reduce the background noise, and then each image was normalized using the average intensity of the images. To further enhance the signal to noise ratio, a sliding minimum with a kernel size of 10×10 pix was also subtracted. In addition, to enhance the uniformity of intensity, images were also normalized using the local intensity averaged over a kernel size of 20×20 pix.

The calibration and volume self-calibration were conducted as explained in the previous section. The standard deviation of the fit was 0.16 pix and 0.12 pix for the two planes of the 3D target. After applying the self-calibration process several times, the mean disparity

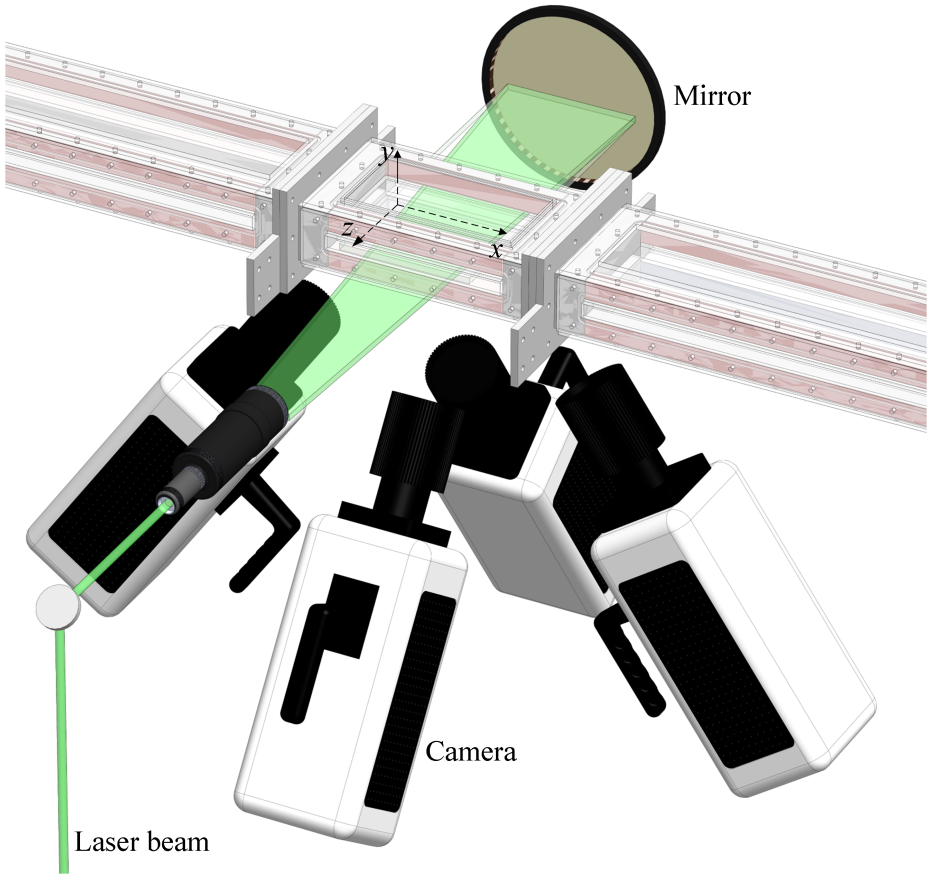

Figure 3.6: The measurement setup indicating the arrangement of cameras, collimator, the laser sheet with respect to the channel, and the coordinate system.

reduced to be less than 0.02 pix with a standard deviation of about 0.03 pix in the entire domain.

An optical transfer function (OTF) was obtained for 20×5×10 sub-volumes in the x, y, and z directions, respectively. A fit area of 3×3 pix was used to calculate the OTF. The STB algorithm applied 4 outer loop iterations with a maximum triangulation error of 1.0 pix and 4 inner loop iterations with a shake width of 0.1 pix. The maximum particle shift was limited to 8.0 pix, and the particles that were closer than 2.0 pix to each other were removed from the tracking process. The aforementioned processes were performed in DaVis 8.4 (LaVision GmbH).

Quadratic regression was applied to the detected trajectories to enhance the accuracy of

particle positioning and to obtain the particle velocity using a script developed in MATLAB (R2018a). The kernel size of the regression was selected based on the method used by Voth [2000] and Ebrahimian et al. [2019]. It was observed that the variance of streamwise acceleration deviates from the fitted exponential function and increases noticeably due to particle positioning errors for the kernel size smaller than 7 time steps. Therefore, the kernel size of 7 was selected for regression, and the instantaneous velocity of the beads was obtained from the coefficients of the fitted quadratics.

The instantaneous velocity and position of the beads and liquid phase tracers are measured using the aforementioned methods. The results of these measurements are presented in the following chapters.

Chapter 4

Turbulence Modulation

The present study provides a detailed investigation of the effects of particle size, flow Re, and particle concentration on the turbulence statistics of both the liquid and solid phases in a horizontal channel. The Stokes number is employed in the analysis to combine the effect of particle size and flow Re. A combination of PIV and PTV techniques is used for simultaneous measurement of the turbulence statistics of the carrier and particulate phases. The mean velocity profile and Reynolds stresses of the unladen flow are compared with the DNS results of Moser et al. [1999] for evaluation of the measurement system. The measurements are used to obtain turbulence modulation data and evaluate the modulation criterion established by Tanaka and Eaton [2008] at higher Re.

4.1 Introduction

Many earlier studies focused on gas-solid flows, where the influence of particles on the overall flow and on the continuous phase is greater than in liquid-continuous flows because of the larger density ratio and mass loading in gas-solid systems. That said, there are many similarities between particle-laden liquid and gas flows: for example, the addition of particles flattens the mean velocity profile of the carrier phase in the core region of the pipe [Nouri et al., 1987, Tsuji and Morikawa, 1982, Tsuji et al., 1984]. In horizontal air-solid channel flows, the maximum velocity moves away from the pipe axis due to the asymmetric distribution of the particles [Tsuji and Morikawa, 1982]. In vertical gas-solid flows, Tsuji

et al. [1984] observed a concave velocity profile with a local minimum at the center of the pipe. Vreman [2015] observed that the mean velocity profile of the particles in downward air-solid flow is flatter than the velocity profile of the carrier phase in the core region of channel. Nouri et al. [1987] also observed that the velocity difference between the particles and the unladen fluid decreases as the Re increases in a descending liquid-solid pipe flow. As this short review reveals, there are many factors that influence the behavior of particle-laden flows. The difference in previous results is due to the wide range of conditions tested. Here, for improved relevance to mining and petroleum industry, experiments in high Re horizontal solid-liquid flows are required.

One phenomenon that is not properly addressed by most models, is the fact that carrier phase turbulence can be attenuated or amplified by the presence of the particles. The change in carrier phase turbulence kinetic energy when particles are added is referred to as turbulence modulation, which depends on several flow conditions including the flow Re, particle density and size, and volumetric concentration (ϕ_v) of the solid phase [Gore and Crowe, 1989]. The former factors are quantified using the particle Reynolds number (Re_p), which is defined based on the slip velocity and particle diameter. Measurements of Tsuji et al. [1984] in a gas-solid vertical pipe flow showed that 3 mm polystyrene spheres with $Re_p = 470$ intensifies the carrier phase turbulence. They attributed the turbulence augmentation to vortex shedding due to the large Re_p. Although Re_p is a critical parameter to characterize carrier phase turbulence modulation, it is difficult to estimate the slip velocity *a priori* since it depends to a great extent on the carrier phase turbulence [Doroodchi et al., 2008] and local particle concentration [Lee, 1987]. Tanaka and Eaton [2008] introduced a particle momentum number (Pa) to model turbulence modulation for a large set of experimental data. The Pa combines Stokes number (St) with flow Re, Kolmogorov length scale, and the characteristic dimension of the conduit. They observed that particles with $Pa < 10^3$ or $Pa > 10^5$ augment the turbulence kinetic energy while attenuation occurs when $10^3 < Pa < 10^5$. It is important to note that for the set of data examined by Tanaka and Eaton [2008], Re was limited to 30,000. The experiments of the current investigation will extend

evaluation of turbulence modulation to Re higher than 125,000.

There are a limited number of investigations focusing on the turbulent statistics of the dispersed (solid) phase. The effects of particle concentration, particle size and density and flow conditions (e.g. flow Re) have been investigated, typically over narrow ranges. As described in the following paragraphs, different investigations sometimes provided conflicting results. Tsuji and Morikawa [1982] measured solid-phase turbulence in a horizontal pipe flow of an air continuous system using laser Doppler anemometry (LDA). They observed a relatively uniform and flat distribution of solid-phase streamwise turbulence intensity across most of the cross-section, which decreased with increasing particle concentration. Nouri et al. [1987] also used LDA to observe the reduction of streamwise turbulence intensity of acrylic particles in water with the increase of volumetric concentration from 0.1% to 14% in a vertical pipe. The LDA measurements of Kulick et al. [1994] also showed reduction of the turbulence intensity of copper particles in a channel flow of air with increasing particle concentration. The decreasing particle turbulence intensity at higher particle concentrations has been associated with the rise in the number of inelastic particle collisions. Most studies on particulate phase turbulence were carried out in solid-gas flows or in vertical pipes. The influence of volumetric concentration on turbulence in horizontal solid-liquid systems remains unexplored, and is addressed in the current investigation.

Measurements in solid-gas flows have shown that, in general, larger and heavier particles result in higher streamwise particle turbulence intensity. Kussin and Sommerfeld [2002] observed the increase of particle turbulence intensity when the diameter of glass beads increases from 60 to 190 µm in a channel flow of air. They associated the trend with larger particle inertia and more collisions with the wall. Kulick et al. [1994] indicated that the streamwise turbulence intensity of particles also increases with increase of particle density. The effect of particle size on turbulence intensity in an upward liquid flow was investigated by Shokri et al. [2017] using combined PIV and PTV. They investigated 0.5, 1 and 2 mm glass beads at $Re = 320{,}000$ and observed, in contrast to the result of Kussin and Sommerfeld [2002], that the smaller particles have higher near-wall turbulence. More investigation is

required to clarify the discrepancy between the results obtained in gas and liquid carrier phases. Specifically, no experimental investigation is found in the literature concerning the effect of particle size on the particulate phase turbulence in horizontal liquid-continuous flows. The current study investigates this relationship at different flow Re.

Another important aspect of two-phase particulate flows is the spatial distribution, or concentration profile, of particles across the channel or pipe. This is particularly important for modeling wear in two-phase pipelines [Shook et al., 1990]. In a vertical gas-solid pipe flow, Lee and Durst [1982] carried out several experiments with 100-800 µm particles at $Re \sim 8000$. It was found that small particles are concentrated in a region near the pipe wall while the larger particles mostly accumulate in the core region. They attributed the distribution to the shear-induced lift force (i.e., Saffman force) in the radial direction [Saffman, 1965]. The magnitude and direction of this lift force depends on the relative velocity between the particles and the carrier phase around them. In the near wall region, the small particles are faster than the surrounding fluid while the larger particles are slower than the surrounding fluid. In the former case, the Saffman force acts towards the wall, while in the latter case (for the larger particles) it acts in the direction of the pipe core. Concentration profiles of buoyant particles at $Re = 5600$ were evaluated using direct numerical simulation (DNS) by Picano et al. [2015]. Their results showed a generally uniform distribution of particles across the channel except near the wall, where a near-wall local maximum at $y/h \sim 0.06$ and a local minimum at $y/h \sim 0.12$ were observed. In their study, y refers to wall-normal distance and h to the half-channel height. The investigations showed that the number density and dispersion of the particles across the channel height depends on the carrier phase turbulence and density ratio of solid and liquid phases. However, in general, lighter particles at high Re have a more uniform distribution.

4.2 Experimental conditions

Glass beads with nominal diameters of 285 µm, 530 µm, and 700 µm (Manus Abrasive Systems Inc.) and density of 2.60 gr/cm^3 were used as the particulate phase. The actual

size distribution of each particle type is obtained from the PTV images (detailed in Section 3.2) and their probability density functions are shown in Figure 4.1. An estimation of the median diameter (d_b) of the beads is used to indicate the particle size as presented in Table 4.1. The experiments are conducted at different particle volumetric concentrations (ϕ_v) and Re, as summarized in Table 4.1. The Re is calculated based on the channel height (h) and average velocity (U_{avg}) at the test section. The first row of the table shows the experiments conducted to study the effect of Re for different particle sizes. The results of these experiments are detailed in Sections 4.4.2 and 4.4.3. The second and third rows of the table present the experimental conditions selected to investigate the influence of particle size and volumetric concentration, which will be discussed in Sections 4.4.4 and 4.4.5, respectively.

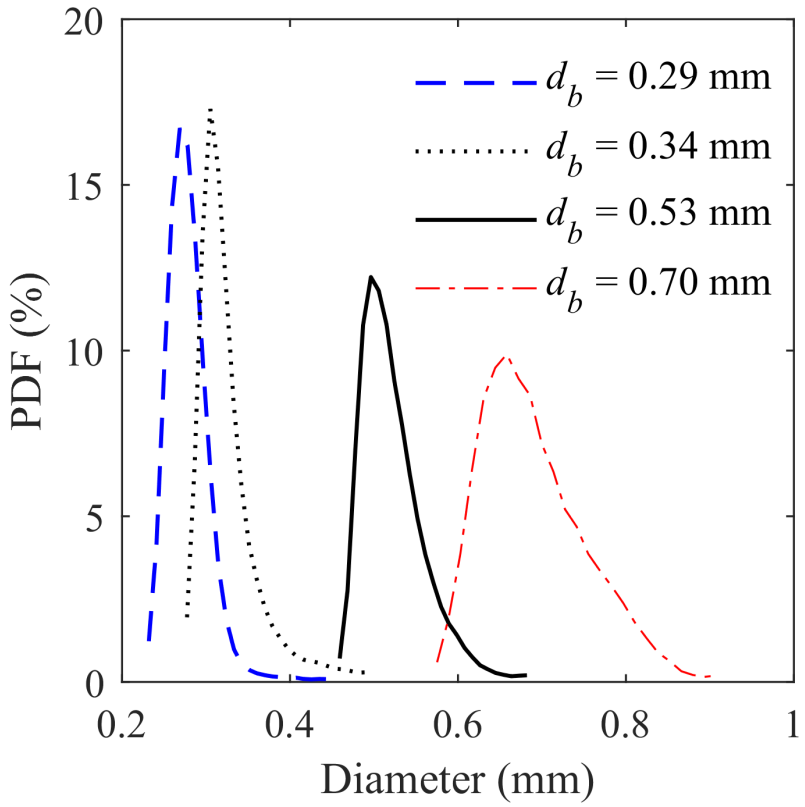

Figure 4.1: Size distributions of the four particle types used in the experiments in this chapter, estimated from the PTV images.

Table 4.1: Experimental conditions used in the two-phase experiments to investigate the effect of Re, particle size and volumetric concentration.

Objective of the investigation	$Re \times 10^{-3}$	d_b (µm)	ϕ_v (%)
Effect of Re	50, 75, 100, 125	285	0.05
	50, 75, 100, 125	530	0.05
	50, 75, 100, 125	700	0.05
Effect of particle size	50	285, 530, 700	0.05
	125	285, 530, 700	0.05
Effect of ϕ_v	75	340	0.03, 0.09, 0.18
	125	340	0.03, 0.09, 0.18

Table 4.2: The unladen flow conditions obtained from PIV measurements detailed in Section 3.2.

$Re\,(\times 10^3)$	$Re_\tau\,(\times 10^3)$	U_{avg} (m/s)	U_c (m/s)	u_τ (m/s)	λ (µm)
50	1.20	2.45	2.74	0.12	6.1
75	1.65	3.67	4.08	0.16	4.6
100	2.25	4.89	5.40	0.22	3.3
125	2.75	6.12	6.70	0.27	2.7

4.3 Flow conditions

The non-dimensional numbers used for presenting and discussing the results are defined here. Measured mean velocity and rms of velocity fluctuations in the two-phase experiments are normalized by the centerline velocity (U_c). The average velocity (U_{avg}) is the average of liquid phase velocity over the channel height at the mid-spanwise plane of the channel, and is used to calculate the Re. These quantities are obtained from PIV measurements in the unladen flow and are presented in Table 4.2. The table also presents the friction velocity, u_τ , and wall-unit, $\lambda = \nu/u_\tau$, estimated using the Clauser method [Clauser, 1956] from the measured PIV data. The Reynolds number based on the friction velocity and half-channel height ($Re_\tau = u_\tau h/2\nu$) is also reported, where ν is the kinematic viscosity of water.

Both the flow characteristics and the fluid interaction with the particulate phase are

Table 4.3: Calculated values of particle Stokes numbers (St) based on the Kolmogorov time scale and the integral time scale (presented in parentheses).

	$Re = 50,000$	$Re = 75,000$	$Re = 100,000$	$Re = 125,000$
$d_b = 285$ µm	4.1 (0.60)	7.5 (0.90)	11.4 (1.19)	15.8 (1.47)
$d_b = 530$ µm	8.1 (1.18)	14.8 (1.76)	22.5 (2.33)	31.0 (2.89)
$d_b = 700$ µm	10.6 (1.55)	19.3 (2.31)	29.4 (3.05)	40.6 (3.79)

governed by several non-dimensional flow conditions including density ratio, Re, and St. The St is the ratio of the response time of particles to a characteristic time-scale of the flow, typically the integral or Kolmogorov time scale. The integral time-scale (τ_L) is basically computed using the autocorrelation function [Pope, 2000], which is not applicable here, since it requires time-resolved data. Similar to the works of Milojević [1990], Kussin and Sommerfeld [2002], and Brenn et al. [2003], the integral (τ_L) and Kolmogorov (τ_K) time scales are calculated using Eqs. 2.31 to 2.34.

The calculated values of St for the 285, 530, and 700 µm particles at the Re values studied here (see Table 4.1) are presented in Table 4.3. The Kolmogorov Stokes number is referred to as St_k and will be used for the analysis reported in this chapter. The settling parameter is defined as the ratio of the terminal settling velocity V_s to the friction velocity, u_τ. When V_s/u_τ is ~ 1, the particles stay in suspension [Sumer and Oguz, 1978]. The particle sizes and Re numbers considered here are such that a particle bed does not form in the channel: V_s/u_τ values vary from 0.31 for $d_b = 285$ µm and $Re = 125{,}000$ to 4.5 for $d_b = 700$ µm and $Re = 50{,}000$. It was observed that the particles remain completely suspended in the flow when $V_s/u_\tau = 0.31$, while the particles mostly appear at bottom half channel for $V_s/u_\tau = 4.5$.

4.4 Results and discussion

In this section, measurements for the unladen flow are compared with the DNS results of Moser et al. [1999] for an uncertainty evaluation of the PIV system. The subsequent subsections investigate the effect of Re, particle size and concentration on the turbulence

intensity of the solid and liquid phases. The observations are discussed and compared with previous studies reported in the literature (e.g., Kiger and Pan [2002], Shokri et al. [2017], Varaksin et al. [2000], Zhao et al. [2015]). The velocity and turbulence intensity results are plotted for the bottom half of the channel due to its higher solids concentration and greater relevance to industrial applications. The instantaneous velocity U in turbulent flow is decomposed into a mean, shown as $\langle U \rangle$, and a fluctuating component u, where $U = \langle U \rangle + u$.

4.4.1 Unladen turbulent channel flow

The mean velocity profile and turbulence intensities of the unladen flow at Re = 20,000, 40,000 and 75,000 are compared with DNS of Moser et al. [1999] in Figure 4.2. The Re of the unladen flows are selected based on the availability of DNS data but they are also within the range of Re of the two-phase flow experiments. The figures are normalized using the channel height and centerline velocity. This outer layer scaling (h and U_c) is selected since spatial resolution of the PIV system is selected to measure the full channel. The mean streamwise velocity profiles are in agreement with the DNS results in the bottom-half of the channel as shown in Figure 4.2a. The discrepancy between the DNS and the experimental results is less than 1.0% at $y/h > 0.025$. The figure also reveals that the maximum velocity is also located at $y/h = 0.5$, showing the symmetry between the top and bottom halves of the channel.

The streamwise turbulence intensity, $\langle u^2 \rangle / U_c^2$, plotted in Figure 4.2b, agrees with the DNS results at $y/h > 0.1$ with a maximum discrepancy of 4.0%. The discrepancy closer to the wall is due to the limited spatial resolution of the PIV system. The PIV measurements of the wall-normal Reynolds stress, $\langle v^2 \rangle / U_c^2$, in Figure 4.2c are smaller than the DNS values. This figure indicates a systematic bias error with underestimation of approximately 8.5% at $y/h = 0.1$ at Re = 75,000. The difference decreases approaching the channel centerline since the turbulent scales become larger. The spatial averaging within the interrogation window in the PIV measurement causes an underestimation of the turbulence intensities since the

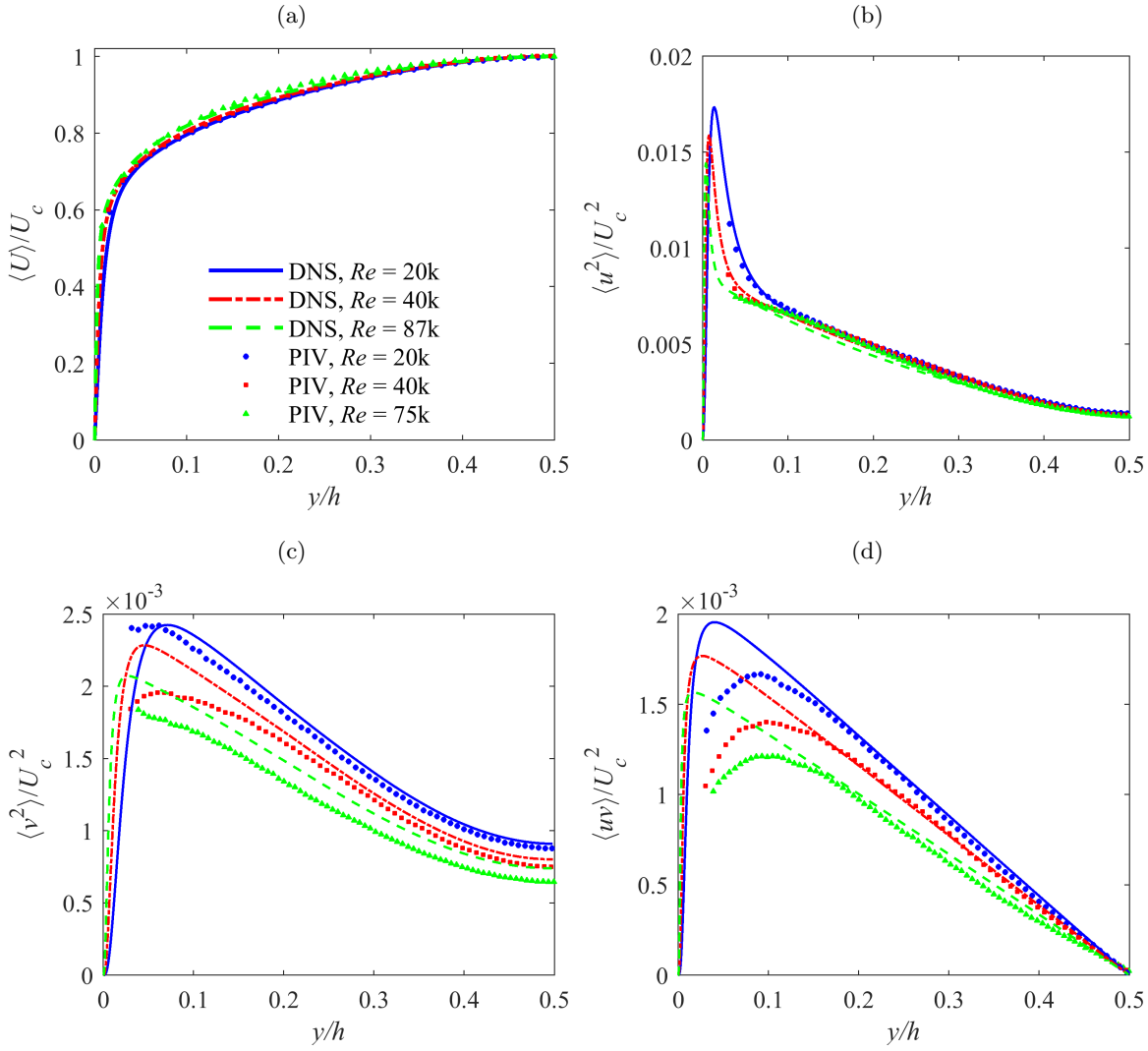

Figure 4.2: Profiles of normalized (a) mean streamwise velocity, (b) streamwise turbulence intensity, (c) wall-normal turbulence intensity, and (d) Reynolds shear stress. The lines represent the DNS data at Re = 20,000 (Re_τ = 540), Re = 40,000 (Re_τ = 1050), and Re = 87,300 (Re_τ = 1995). The symbols indicate the PIV measurement results at Re = 20,000 (Re_τ = 545), Re = 40,000 (Re_τ = 1000), and Re = 75,000 (Re_τ = 1640). Only one out of two data points is presented for clarity of the plots.

turbulent energy contribution from small scale eddies is not resolved [Lee et al., 2016]. The ratio of interrogation window size to the Kolmogorov scales rises with the increase of the Reynolds number. Hence, the missing small-scale energy due to spatial resolution is larger at higher Re. The Reynolds shear stress profiles of Figure 4.2d show agreement with DNS

results at $y/h > 0.15$ where the profile is linear. A discrepancy is observed closer to the wall with the deviation of 10% at $y/h = 0.1$.

The assessment of the deviation of PIV measurements from the DNS data shows that measurement of $\langle u^2 \rangle$ is reliable at $y/h > 0.1$, with an uncertainty smaller than 4.0%. The smaller displacement of the tracers in the wall-normal direction in the double-frame PIV images increases the relative error in statistics that include the v component. Therefore, the investigation of the wall-normal turbulent intensity and the Reynolds shear stress of the liquid-phase is restricted to $y/h > 0.15$ in the next sections.

4.4.2 Effect of *Re* on mean velocity

This section investigates the effect of Re on the mean velocity profile of the liquid and particulate phases. The normalized streamwise and wall-normal mean velocity profile of the glass beads and the carrier phase over the bottom half-channel are plotted in Figure 4.3a–c for the three particle diameters of 285 µm, 530 µm and 700 µm, respectively. Volumetric concentration of the particles is 0.05% as mentioned in Table 4.1. The results are presented for the bottom half-channel because most of the beads were found in this region, and thus the computed statistics are more reliable. Each figure shows velocity profiles of liquid and solid phases for Re of 50,000, 75,000, 100,000 and 125,000, as well as the streamwise velocity of the unladen flow. In general, the impact of particles on the mean velocity profile at the investigated concentration is negligible and the profiles of the liquid phase and the unladen flow are essentially identical. However, the velocities of the carrier phase and the particles are different, as discussed below. The wall-normal velocity profiles also indicate that the net wall-normal velocity is negligible compared to the streamwise component of velocity, and the glass beads stay in suspension.

Figure 4.3 shows that the relative velocity of the liquid and particulate phase depends on both Re and particle size. Scrutiny of Figure 4.3 reveals that the mean velocity of $d_b = 285$ µm particles at all Re is smaller than the velocity of the liquid phase at $0.03 < y/h < 0.5$ where reliable data for the particulate phase is available. For larger particles of $d_b = 530$ and

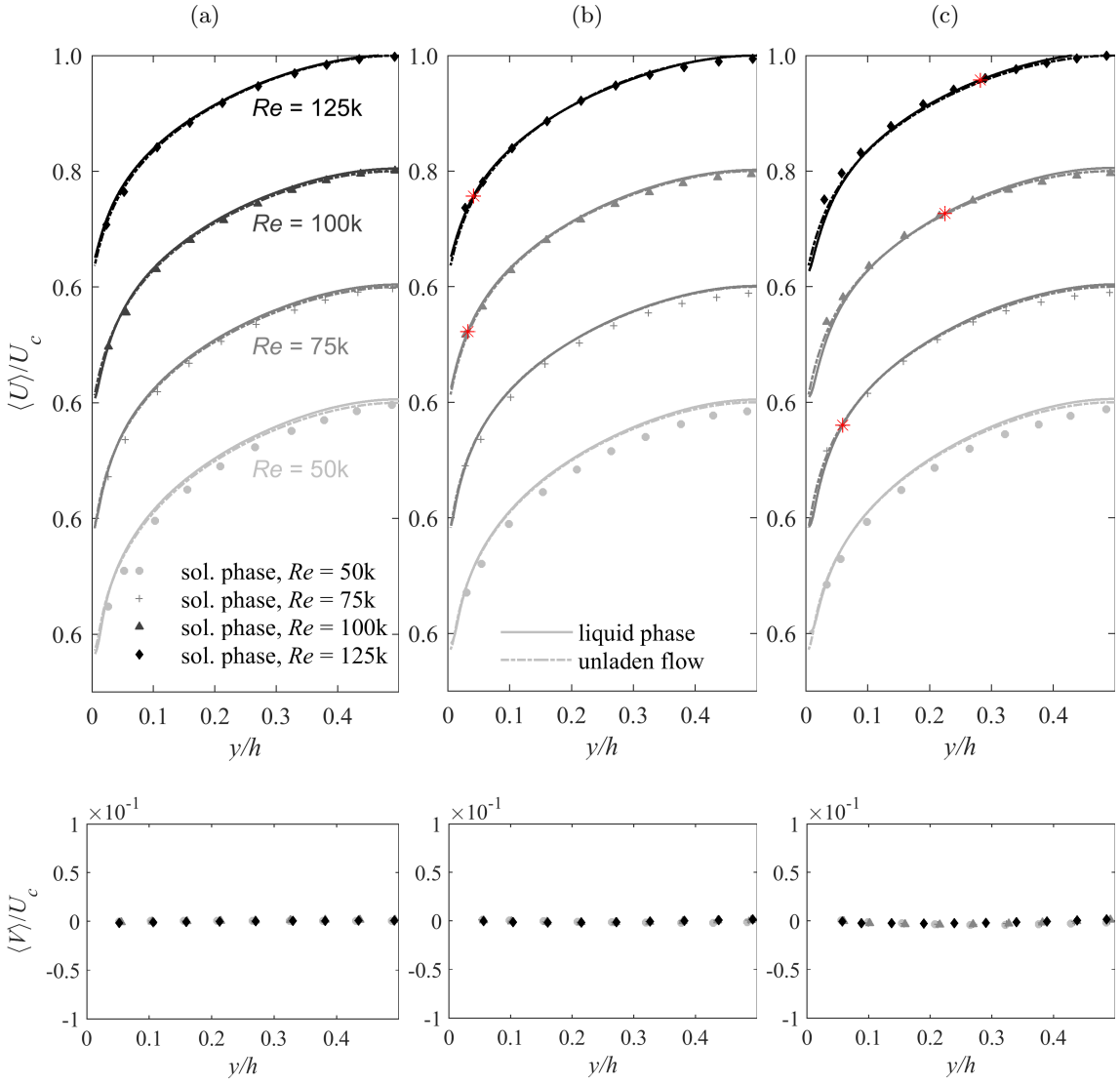

Figure 4.3: Mean streamwise and wall-normal velocity profile of liquid phase and the dispersed phase of (a) 285 µm, (b) 530 µm and (c) 700 µm glass beads. The profiles are shown for four Reynolds numbers of Re = 50,000, 75,000, 100,000, 125,000 that are discriminated using different shades. The normalized streamwise mean velocity profile changes from almost 0.6 near the wall to 1.0 at the centerline. The data of the four Re are separated by shifting the profiles upward by an increment of $0.2U_c$.

700 µm, the mean velocity is smaller than the unladen liquid only at the lowest Re of 50,000 in the specified region. In other words, at higher Re, only the small particles have a mean velocity lower than that of the carrier phase, while all the particles exhibit a finite (nonzero) mean slip velocity at the lowest Re tested here. The observed lag is due to the preferential

accumulation of the beads in low-speed regions. It has been shown by Kiger and Pan [2002] and van Hout [2011] that most of the upward-moving beads (ejection motion) are located in low-speed regions, while downward-moving beads (sweep motion) are distributed more evenly over high-speed and low-speed flow regions. However, it is noteworthy that the glass beads in the aforementioned cases might lead the fluid in the near-wall region ($y/h < 0.03$).

In the high velocity region of the channel ($y/h > 0.3$), the particles are slower than the liquid phase at all flow Re tested here. This lag in particle velocity decreases as the Re increases, consistent with the results of Rashidi et al. [1990] for the liquid-continuous flow in a horizontal channel and those of Shokri et al. [2017] for the liquid-continuous flow in a vertical pipe. In the near-wall region, the larger particles lead the liquid phase. For example, the 700 µm particles of Figure 4.3c have higher mean velocity than the fluid phase at $y/h < 0.25$ for Re = 100,000 and larger. The same result was found in upward pipe flow by Shokri et al. [2017], and has been associated with the large wall-normal displacement of high velocity glass beads from the center of the channel to the near-wall region [Vreman, 2015]. The larger particles travel a longer distance in the wall-normal direction and preserve their momentum for a longer time, due to their larger St.

The point at which the velocity of the particle and the liquid phase are the same is called the crossing point and is indicated by the symbol '*' in Figure 4.3. No crossing point is detected in the region $0.03 < y/h < 0.5$ for the 285 µm particles at Re = 50,000 as the particle velocity is smaller than the liquid phase across the measurement range. As the particle size and Re increase, St also increases, and the crossing point moves away from the wall. A similar trend was observed by Shokri et al. [2017] in an upward solid-liquid pipe flow, while Lee and Durst [1982] observed that the crossing point moves closer to the wall as the particle size increases in a solid-gas flow. This highlights the different behavior of particles in liquid and gas flows. Increasing the St (by increasing particle density or diameter) in gas flows reduces the particulate phase velocity across the whole conduit cross-section, which moves the crossing point towards the wall [Kulick et al., 1994, Lee and Durst, 1982]. However, with increase of St, the particulate phase velocity increases in the

near-wall region for solid-liquid flows, and the crossing point moves away from the wall.

The particle Reynolds number is a critical parameter in evaluating the turbulence modulation and is defined here as $Re_p = |\langle U \rangle - \langle U_b \rangle| d_b/\nu$. This is computed using the mean velocities of the liquid and solid phases and is shown in Figure 4.4a–c for $d_b = 285$, 530, and 700 µm particles, respectively. As expected, Re_p is larger for larger particles and decreases with increase of flow Re at $y/h > 0.3$ where the particle velocity is lower than that of the fluid. However, the influence of flow Re on Re_p is more pronounced for the larger particles of Figure 4.4b and 4.4c. A large increase in Re_p (and the relative velocity) is observed for the larger particles of Figure 4.4c at wall-normal distances at $y/h \leqslant 0.1$. The Re_p changes from 11 at Re = 50,000 and reaches a maximum value of 225 for Re = 125,000 in this region.

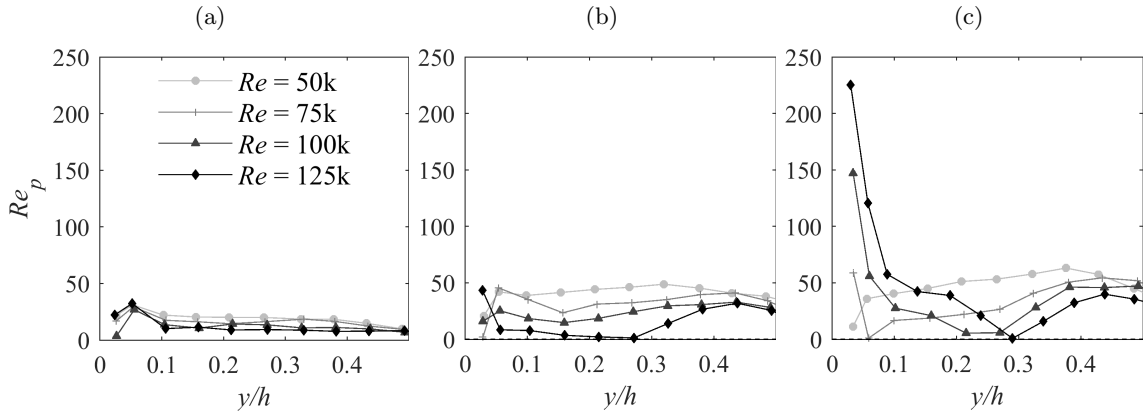

Figure 4.4: Particle Reynolds number across the channel based on the mean relative velocity ($\langle U \rangle - \langle U_b \rangle$) for (a) 285 µm, (b) 530 µm, and (c) 700 µm glass beads at different Re.

The suspended particles can augment or attenuate liquid phase turbulence over different length scales [Balachandar and Eaton, 2010], which can be discussed in terms of Re_p. Taneda [1956] investigated the wake of a sphere as it moved through a tank of water. It was observed that when $Re_p < 22$, the flow around the sphere is completely laminar and no vortices can be found. As Re_p increases to about 24, a pair of stationary vortices appear in the wake. They stated that the vortices grow and stretch along the flow direction as Re_p increases. The vortices start oscillating when Re_p of 130 is reached while they are

still attached to the sphere. At larger Re_p vortex shedding occurs behind the particle and enhances the liquid phase turbulence. On the other hand, attenuation of liquid phase turbulence occurs due to turbulence dissipation at smaller scales. The overall modulation of turbulence in the liquid phase relies on the relative strength of the vortex shedding and the dissipation mechanisms.

The average of instantaneous slip velocity, defined as $\langle|U - U_b|\rangle$, is a more accurate representation of mean slip velocity for computing Re_p, relative to the difference between the average velocity of the liquid and particulate phase ($\langle|U - U_b|\rangle$). Computing $\langle|U - U_b|\rangle$ requires measurement of liquid velocity, with high spatial resolution, in the immediate vicinity of the glass beads, which is not available from the current PIV/PTV. Due to preferential accumulation of glass beads in the low-speed streaks, Figure 4.4 can slightly overestimate Re_p. Lelouvetel et al. [2009] observed that around 60% of 200 µm glass beads at Re = 30,000 are aggregated in the low-speed regions of the flow. However, distribution of glass beads over high-speed and low-speed regions is expected to be more uniform in the current experiment, since particle aggregation in low-speed streaks reduces with the increase of St [Marchioli et al., 2003].

4.4.3 Effect of *Re* on turbulence and particle distribution

The effect of Re on streamwise turbulence of the liquid and solid phases at the bottom half of the channel is shown in Figure 4.5a and 4.5b for d_b = 285 and 700 µm particles, respectively. The streamwise turbulence of the unladen flow at the same Re is also shown for comparison. In general, the streamwise turbulence intensity of the liquid in the two-phase flow is slightly larger than the unladen flow. Therefore, turbulence production by vortex oscillation is stronger than the dissipation of turbulence. For the 700 µm particles, which are associated with larger values of Re_p, the vortex shedding augmentation mechanisms are stronger and a slightly larger difference is observed between the turbulence intensity of the liquid phase in the two-phase flow and the unladen flow. The wall-normal turbulence intensities of both the solid and liquid phases for d_b = 285 µm and d_b = 700 µm particles

are shown in Figure 4.6a and b, respectively. The level of bias error in the $\langle v^2 \rangle$ profiles estimated through comparison with the DNS data is shown by the error bars in the figure for Re of 50,000 and 75,000. The augmentation in wall-normal turbulence is relatively large; the addition of glass beads increases $\langle v^2 \rangle$ of the liquid phase up to two times that of the unladen flow. The largest increase in liquid phase wall-normal intensity occurs for the two-phase flow with the 700 µm particles.

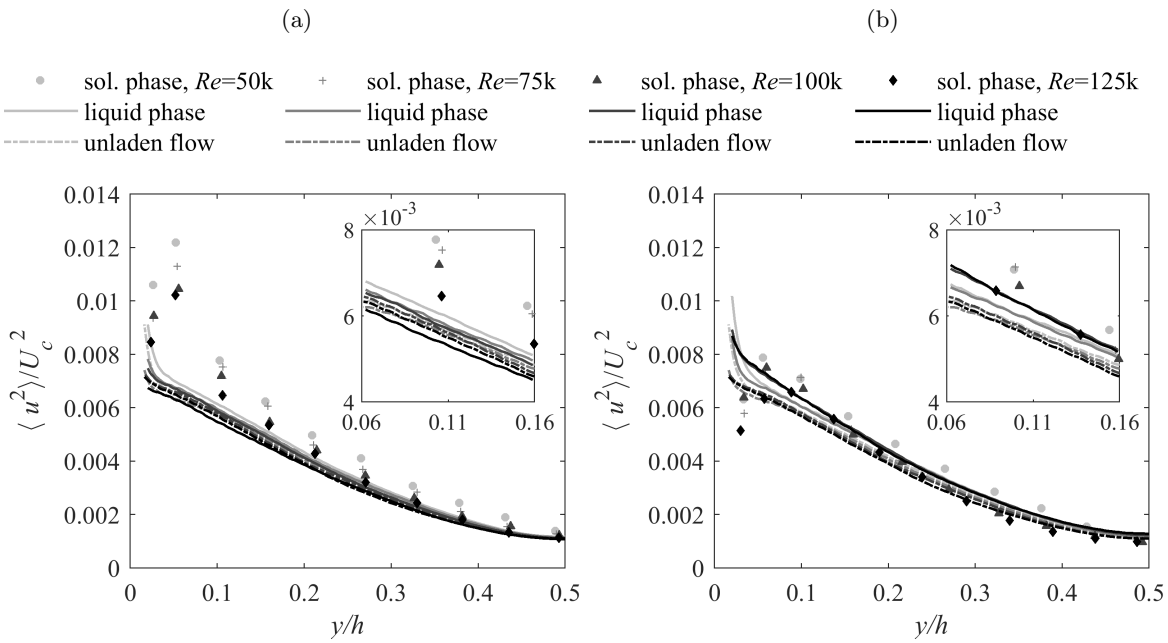

Figure 4.5: Streamwise turbulence intensity of the carrier and solid phases in flow with (a) $d_b = 285$ µm and (b) $d_b = 700$ µm particles. The statistics of the unladen flow at the same Re is also shown for comparison.

The streamwise turbulence intensities of the $d_b = 285$ µm particles (shown in Figure 4.5a) and $d_b = 700$ µm particles at Re of 50,000 as shown in Figure 4.5b are larger than the carrier liquid phase. Due to the larger inertia of the particles, they maintain their streamwise velocity longer than the fluid when transported in the wall-normal direction. This results in larger streamwise velocity fluctuations of the particulate phase [Kulick et al., 1994]. Comparison with $\langle u^2 \rangle$ shows the wall-normal turbulence intensity of the particulate phase is smaller than the liquid phase intensity (see Figure 4.6a). Similar results were

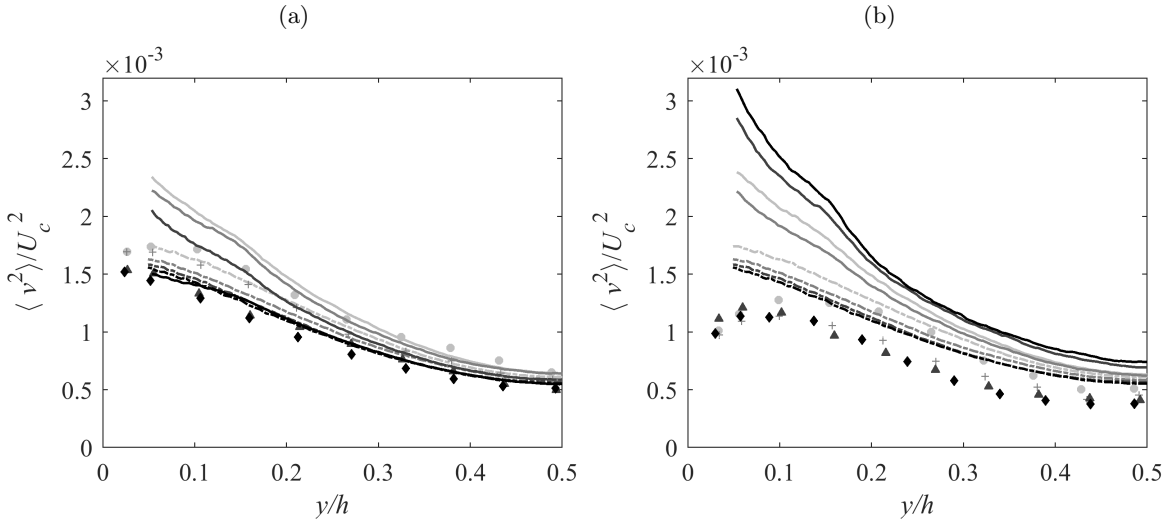

Figure 4.6: Wall-normal turbulence intensity of the carrier and solid phases in flow with (a) 285 µm, and (b) 700 µm particles. The statistics of the unladen flow at the same Re is also shown for comparison. For legends, see Figure 4.5.

found by Kulick et al. [1994] and Varaksin et al. [2000] in downward air-solid flow and also in horizontal channel air-solid flow by Sommerfeld [2003] and Zhao et al. [2015]. The power spectra of the streamwise and wall-normal velocity show that the v fluctuation occurs at higher frequency than the streamwise fluctuations [Kulick et al., 1994, Zhao et al., 2015]. Therefore, the smaller $\langle v^2 \rangle$ of the particles is associated with lack of response of the particles to high-frequency wall-normal fluctuations of the fluid. This is consistent with the smaller wall-normal turbulence intensity of the larger 700 µm particles in Figure 4.6b relative to that of the smaller particles in Figure 4.6a.

Figures 4.5 and 4.6 also show that $\langle u^2 \rangle$ and $\langle v^2 \rangle$ of the particles decrease with increase of flow Re and also by increase of particle diameter. The larger Re results in a smaller flow time-scale and consequently larger St. Larger particles also indicate a longer response time and larger St, as observed in Table 4.3. Therefore, increase of St reduces the turbulence of the particles. This agrees with the results of Shokri et al. [2017] regarding the variation of $\langle u^2 \rangle$ versus particle size. When St is large, the response of the particle to carrier phase fluctuation decreases and transfer of turbulent kinetic energy to the glass beads is reduced.

Hence, the turbulence intensity of particles is reduced with increase of Re and particle size (increase of St).

The DNS results of Zhao et al. [2015] showed an opposite trend for variation of particle streamwise turbulence intensity with St. They studied gas-solid flow in a horizontal channel at low Re ($Re \sim 4200$) and compared the turbulence intensity of 96 µm particles with densities of 225 and 1350 kg/m^3 at a volumetric concentration of 0.0073% (about ten times lower than the concentration used in this study). Their results revealed that heavier particles with larger St have higher streamwise turbulence intensity. The same result as Zhao et al. [2015] was obtained by Kussin and Sommerfeld [2002] at Re of 42,500 and Kulick et al. [1994] at $Re = 13{,}800$, for particle sizes ranging from 50 to 190 µm. The two aforementioned studies also involved solid-gas flows at lower Re and smaller particle size than the current study, which caused their St to be one to two orders of magnitude smaller than those tested here. This implies that there should be a critical Stokes number St_{cr} characterizing these two regimes. Turbulence intensity of the solid phase increases with St for $St < St_{cr}$, and decreases for $St > St_{cr}$.

The Reynolds shear stress profiles are shown in Figures 4.7a and 4.7b for the 285 µm and 700 µm particles, respectively. The maximum Reynolds shear stress of the particles occurs at $y/h \sim 0.1$, and in general they have larger $\langle uv \rangle$ than the liquid phase. This is associated with the larger inertia of the glass beads, which allows them to maintain a higher correlation between the u and v fluctuations. Figure 4.7 also shows that, as the Re increases, the Reynolds stress of the particles is reduced across $0.1 < y/h < 0.5$. The reduction is associated with the attenuation of the streamwise and wall-normal Reynolds stress of the particles as shown in Figures 4.5 and 4.6.

The distribution of glass beads across the entire channel at various Re is indicated in Figure 4.8a for $d_b = 285$ µm and in Figure 4.8b for $d_b = 700$ µm particles. The channel height is divided into 50 pixels ($\Delta y_{bin} = 0.57\text{mm}, 0.004h$) bins with zero overlap, and the number density profiles are computed as the ratio between the number of particles in each bin (N_i) and the average number of particles in the bins (N_{avg}). The profiles are not

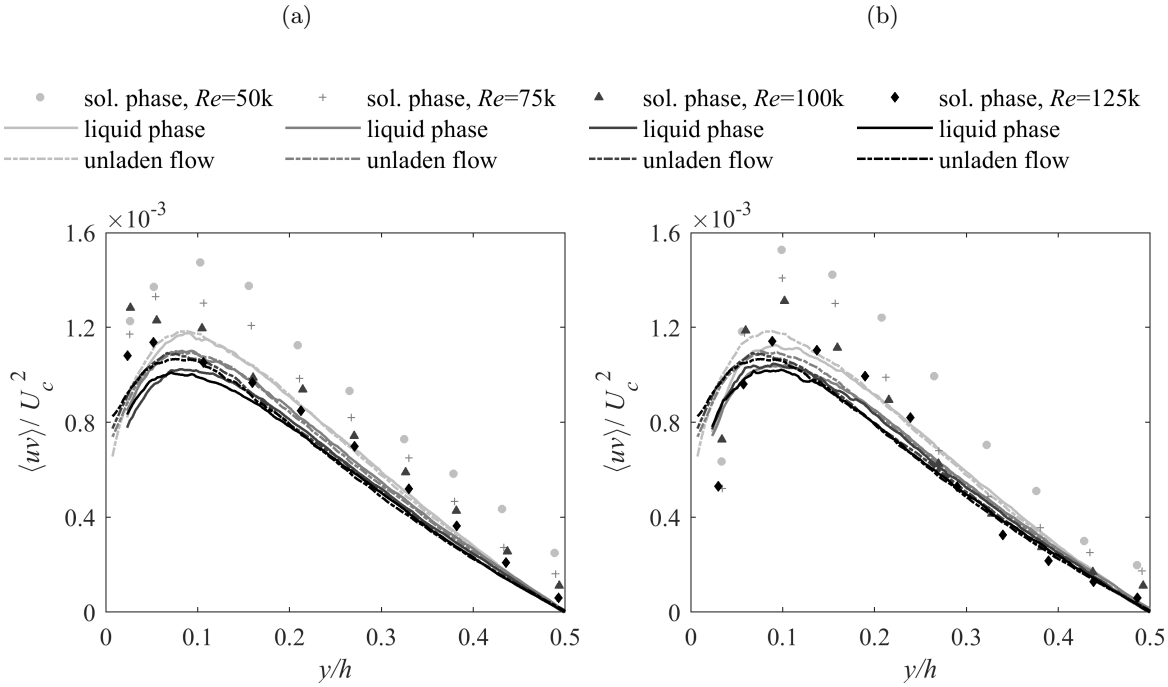

Figure 4.7: Reynolds shear stress of the liquid and solid phases in flow with (a) 285 µm, and (b) 700 µm particles. The statistics of the unladen flow at the same Re is also shown for comparison.

dependent on the bin size because of normalization by N_{avg}, and the area under each plot is equal to unity. The number density is larger in the near-wall region for the low Re cases. This is associated with the larger ratio of the settling velocity to the friction velocity, which indicates poorer dispersion of the glass beads across the channel. With increasing Re, turbulence dispersion becomes stronger, which results in more uniform distribution of particles. A local maximum also appears at $y/h \sim 0.4$ for the 700 µm particles at the highest Re tested (Re = 125,000). Smaller wall-normal bead velocities compared to the streamwise component as represented in Figure 4.3 indicates the bead distributions are in an equilibrium state. Figure 4.6 also indicates that the $\langle v^2 \rangle$ of the particles is $\sim 0.04 U_c$, while the maximum observed wall-normal settling velocity is $\sim 5 \times 10^{-3} U_c$. The comparison of these two values reveals that turbulence in the flow can disperse the beads and bring them into suspension.

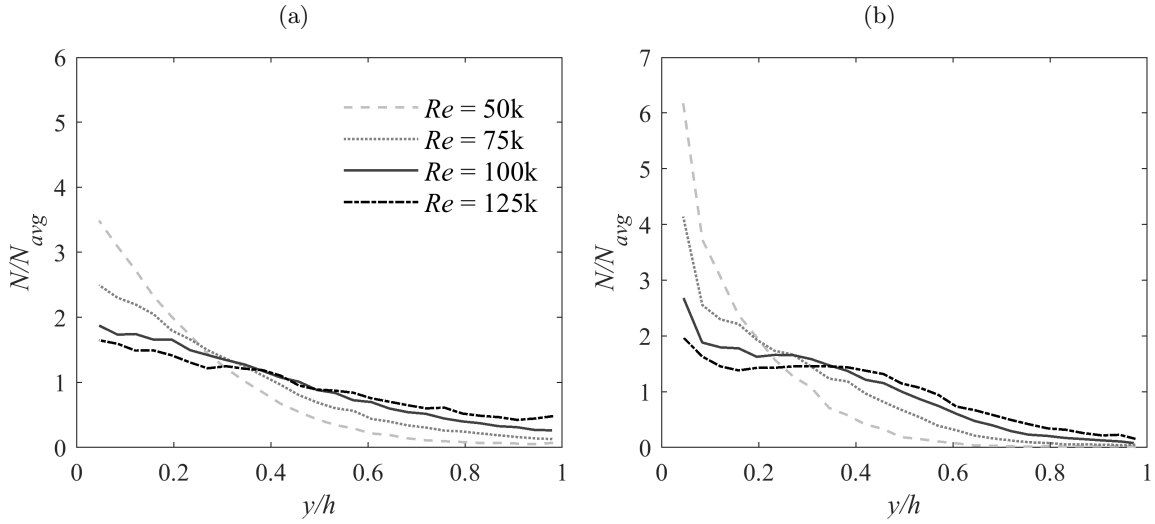

Figure 4.8: The number density distribution for (a) 285 µm particles, and (b) 700 µm particles at Re varying from 50,000 to 125,000. The plots show the number of particles detected in each bin normalized by the average number of particles in all the bins (N_{avg}).

4.4.4 Effects of particle size on turbulence and particle distribution

The influence of particle size on the statistics of the liquid and solid phases at the bottom half of the channel as well as the particle distribution across the entire channel are studied in this section for the experimental conditions mentioned in the second row of Table 4.1. It was observed in Figure 4.3 that the effect of particle size on the mean velocity of the liquid phase is negligible, while it has a stronger effect on the solid phase velocity profile especially near the wall. Increasing the particle size from 530 µm to 700 µm at Re of 100,000 and 125,000 flattens the velocity profile and moves the cross-over point (indicated by '*') toward the center of channel. The variation of the streamwise turbulence intensity of solid and liquid phases with the particle size can be seen in Figure 4.9a for Re = 50,000, and in Figure 4.9b for Re = 125,000. Smaller particles have larger streamwise turbulence intensity. The same trend is observed in Figure 4.10 for the wall-normal turbulence intensity. It was explained in Section 4.4.3 that smaller particles lead to smaller St and relaxation time; hence, they are more responsive to the velocity fluctuations of the liquid phase. The turbulent eddies exert a force on the particle and, consequently, part of the energy of the eddy will be transferred

to the particle. This results in increase of the turbulence intensity of the particulate phase [Gore and Crowe, 1989].

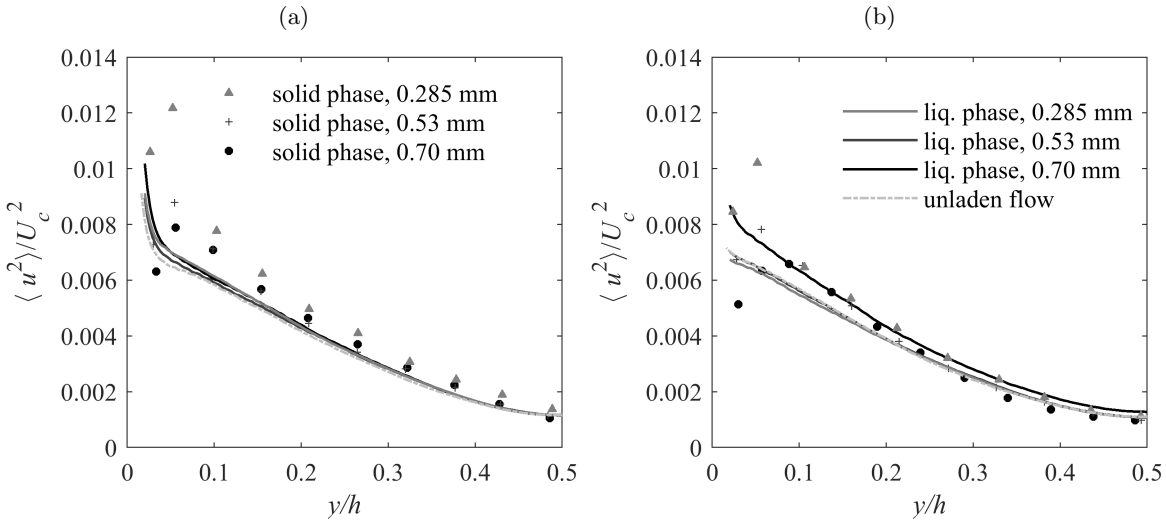

Figure 4.9: The streamwise turbulence intensity of the solid and liquid phases at (a) Re = 50,000 and (b) Re = 125,000 for d_b = 285 µm, 530 µm, 700 µm particles. The streamwise turbulence intensity of the unladen flow is also shown for comparison.

Figures 4.9 and 4.10 show that the difference between $\langle u^2 \rangle$ and $\langle v^2 \rangle$ of the liquid phase in particle-laden and unladen flow is larger in the case of the 700 µm glass beads at Re = 125,000. This is attributable to the larger Re_p of this case with an average value of ~ 60 over the bottom half of the channel. It is observed in Figure 4.5a that the $\langle u^2 \rangle$ of particles is reduced significantly with the increase of particle diameter (or St) at $y/h < 0.1$. The flow has a smaller time scale in this region than in the central region, and the difference between the local St of different particles is more pronounced [Righetti and Romano, 2004]. It can be seen that $\langle u^2 \rangle$ and $\langle v^2 \rangle$ for the 530 µm and 700 µm particles overlap at $y/h > 0.1$ while the 285 µm particles still have moderately larger turbulence intensity. This is related to the fact that the 530 µm and 700 µm particles have similar St, whereas 285 µm particles have considerably smaller St as seen in Table 4.3.

The number density distributions of the three sizes of glass beads are shown in Figures 4.11a-c for Re of 50,000, 100,000 and 125,000, respectively. The number density at $y/h <$

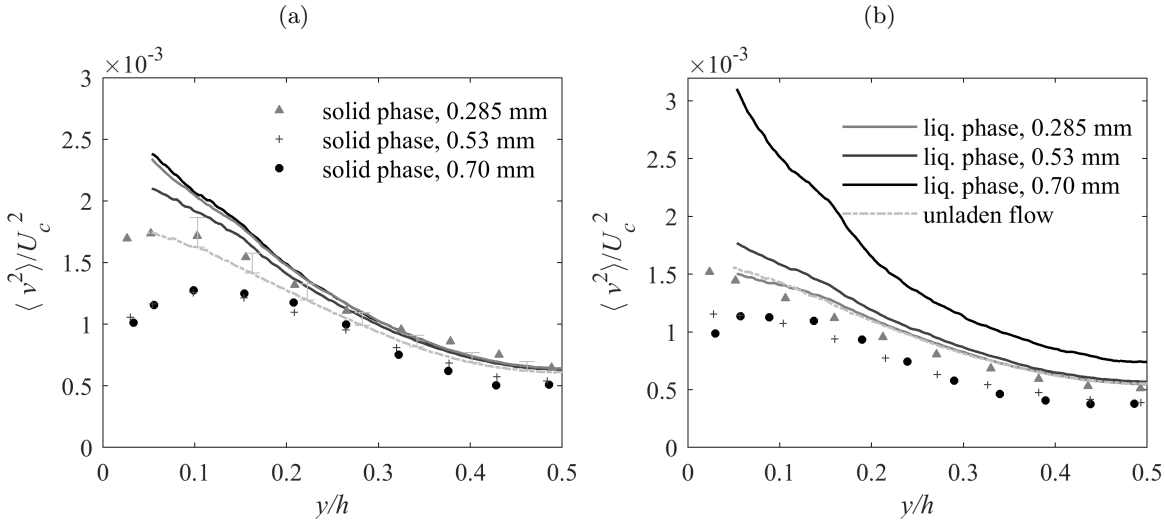

Figure 4.10: The wall-normal turbulence intensity of the solid and liquid phases at (a) Re = 50,000 and (b) Re = 125,000 with d_b = 285 µm, 530 µm, 700 µm particles. The expected underestimation is also shown using error bars for unladen flow at Re = 50,000.

0.15 increases with increasing particle size because of the associated increase in particle settling velocity. The figures also show a clear difference for the largest particle size at Re = 100,000 and 125,000; a local minimum appears at $y/h \sim 0.15$. The number density at the local minimum also decreases with the increase of Re as shown in Figure 4.8b. The local minimum for the d_b = 700 µm particles at Re = 125,000 in Figure 4.11c is indicated by the '*' symbol. A local maximum also appears at greater distance from the wall ($y/h \sim 0.3$). The number density of the particles increases at the local maximum with the increase of particle size.

The distribution of the particles across the channel cross-section depends on the forces acting on the particles in the wall-normal direction. The drag force, shear-induced lift force [Saffman, 1965], gravity, and turbophoresis forces have been shown to be the most important forces in particle-laden turbulent flows [Li et al., 2016, 2001, Marchioli et al., 2003]. The interaction of particles with the non-isotropic turbulence causes turbophoresis [Reeks, 1983, Caporaloni et al., 1975], defined as the tendency of particles to migrate in the direction of decreasing turbulence [Marchioli and Soldati, 2002]. The turbophoretic force

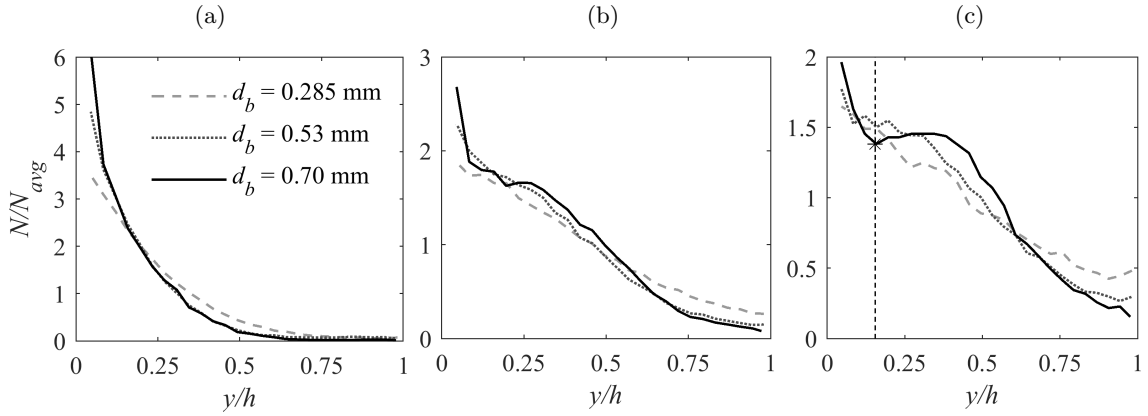

Figure 4.11: The number density distribution for $d_b = 285$ µm, 530 µm, and 700 µm particles at (a) Re = 50,000, (b) Re = 100,000 and (c) Re = 125,000. The number of particles in each bin is divided by the average number of particles in the bins.

acting on the particles in the wall-normal direction is proportional to $\rho_b V_b d\langle v^2 \rangle / dy$, where V_b is the particle volume and the term $d\langle v^2 \rangle / dy$ shows the gradient of wall-normal velocity fluctuation for the particles [Caporaloni et al., 1975]. The magnitude of this force increases with increasing particle size and also increase in $\langle v^2 \rangle$ of particles with increasing flow Re. It is observed in Figure 4.10b that $d\langle v^2 \rangle / dy$ becomes almost zero at $y/h \sim 0.15$ for the 700 µm particles. Therefore, the turbophoretic force is toward the channel center at $y/h > 0.15$, while it changes direction and pushes the particles toward the wall for $y/h < 0.15$. The change in the direction of turbophoretic force seems the most probable factor that causes the local minimum point in Figure 4.11c.

4.4.5 Effects of volumetric concentration on turbulence intensity

The influence of particle volumetric concentration on the mean velocity and turbulence intensity of the liquid and solid phases over the bottom half of the channel for $d_b = 340$ µm particles at Re = 125,000 is shown in Figure 4.12 for $\phi_v = 0.03\%$–0.18% (mass loading of 0.48%). At higher concentrations, the blockage of the line-of-sight of the cameras by the glass beads (i.e., occlusion) becomes significant. The 340 µm beads located between the channel sidewall and laser sheet block approximately 8%, 24%, and 48% of the image area at volumetric concentrations of 0.03%, 0.09% and 0.18%, respectively. These issues limit

the current planar PIV/PTV measurement to 0.18% concentration.

Increasing ϕ_v from 0.03% to 0.18% has an insignificant effect on the solid and liquid phase mean velocity as indicated in Figure 4.12a. It is also shown in Figures 4.12b–d that increasing the volumetric concentration to 0.18% has only a slight impact on the turbulence intensities and Reynolds shear stresses of the glass beads. Comparing the results with the literature shows that the negligible variation is due to the low volumetric concentration. Large eddy simulations of gas-solid flow in a downward channel conducted by Yamamoto et al. [2001] revealed that inter-particle collisions reduce $\langle u^2 \rangle$ and intensify $\langle v^2 \rangle$ of 70 µm copper particles at $\phi_v = 0.014\%$. Yamamoto et al. [2001] stated that the particle-particle collisions convert the energy in streamwise turbulent fluctuations to the wall-normal direction. The same trend is observed by Nouri et al. [1987] in a downward liquid-solid flow. The $\langle u^2 \rangle$ of particles decreased by about 20% as the volumetric concentration of 270 µm acrylic beads increased from 6% to 15%. Reduction in $\langle u^2 \rangle$ of the particulate phase with increasing particle concentration occurs at much lower volumetric concentrations in gas flows.

Tsuji and Morikawa [1982] observed that the streamwise fluctuations of 200 µm particles decreased when the volumetric concentration was increased from 0.04% to 0.33% (mass loading changed from 0.4 to 3.3). The number of inter-particle collisions increases with the number of particles contained in the flow. Hence, the streamwise turbulence intensity should decrease, and the wall-normal turbulence intensity of the solid phase should increase at higher volumetric concentrations. This implies that the collisions between particles is negligible over the range of concentrations investigated in the current study.

Figures 4.12b and 4.12d show that varying the volumetric concentration of the solid phase has a negligible effect on $\langle u^2 \rangle$ and $\langle uv \rangle$ of the liquid phase at $y/h > 0.1$. However, Figure 4.12b indicates that $\langle v^2 \rangle$ of the liquid phase increases with the increase of volumetric concentration. The influence of particles on the liquid phase indicates that two-way coupling exists between the solid and liquid phases. The impact of volumetric concentration at Re = 75,000 is also similar to Re = 125,000 (as shown in Figure 4.12); the results for Re = 75,000 are not presented here for brevity.

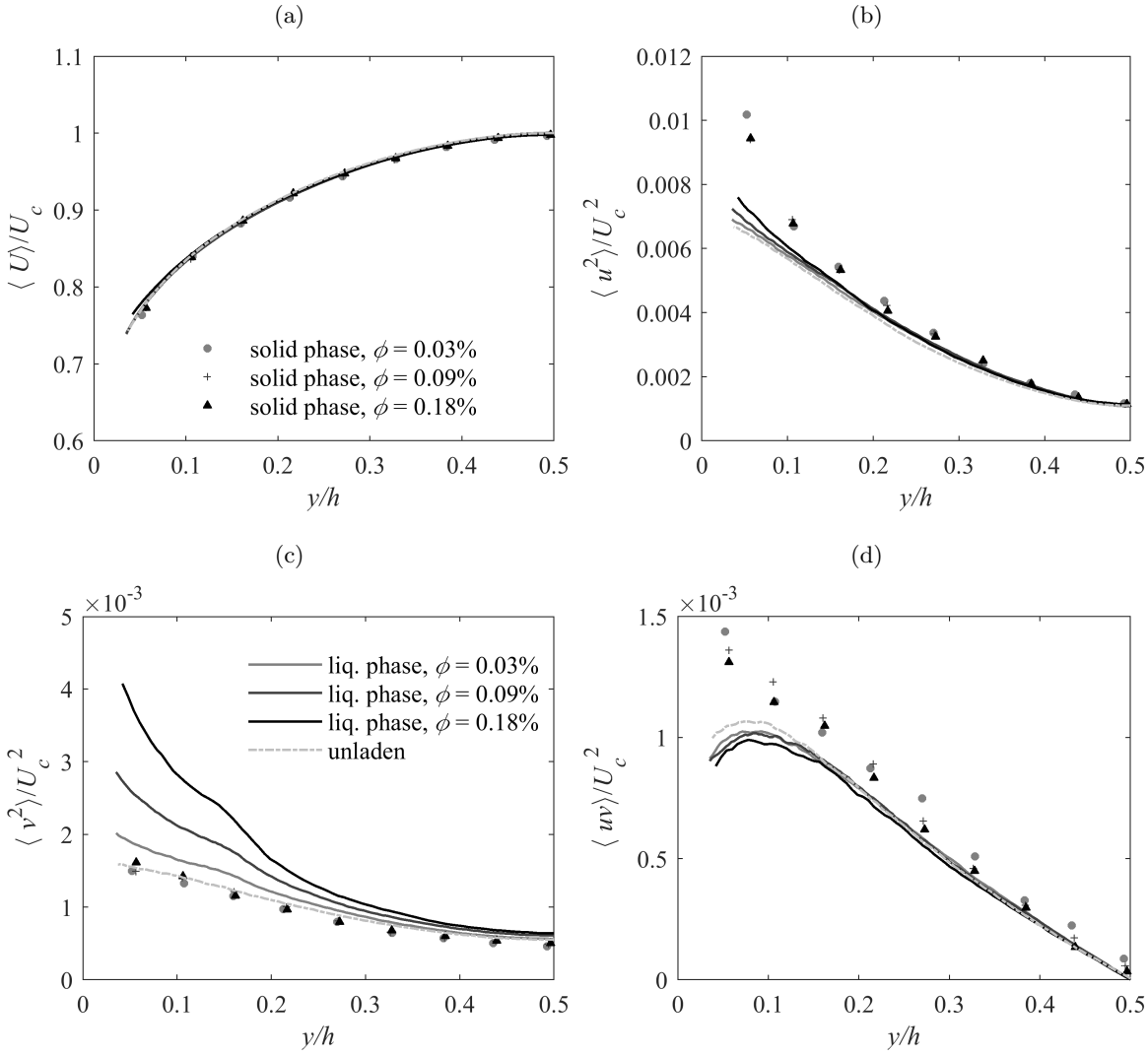

Figure 4.12: The profiles of (a) mean streamwise velocity, (b) streamwise turbulence intensity, (c) wall-normal turbulence intensity, and (d) Reynolds shear stress at Re = 125,000. The statistics of the unladen flow is also shown with the dashed line for comparison.

4.4.6 Turbulence modulation

The addition of solid particles to the flow can either increase or decrease carrier phase turbulence. The difference between the root-mean-square (rms) of streamwise velocity fluctuation of the liquid phase in the particle-laden and the unladen experiments measured at

the channel centerline ($y/h = 0.5$) is defined as turbulence modulation, i.e.:

$$M(\%) = \frac{\sqrt{\langle u^2 \rangle_{PL}} - \sqrt{\langle u^2 \rangle_{UL}}}{\sqrt{\langle u^2 \rangle_{UL}}}, \tag{4.1}$$

where the subscript PL refers to the particle-laden and UL denotes the unladen flow. Several investigations have been carried out to predict M in particle-laden flows. Tanaka and Eaton [2008] suggest a dimensionless number called particle momentum number, Pa, to predict turbulence modulation of the particles. The Pa is defined as

$$Pa = \frac{1}{54\sqrt{2}} \frac{Re^2}{St_K^{0.5}} \frac{\rho_b^{1.5}}{\rho_f^{1.5}} \left(\frac{d_b}{h}\right)^3. \tag{4.2}$$

Tanaka and Eaton [2008] showed, using 80 data points, that turbulence modulation can be divided into three regions in the Re versus Pa plot of Figure 4.13. These two dimensionless numbers are selected since they appear in the non-dimensional particle-laden Navier-Stokes equations. However, it appears that the classification mainly depends on Pa, and Re has little effect, at least in the studied range of Re, which is limited to 30,000. The critical particle momentum numbers are $Pa_{c1} \sim 10^3$ and $Pa_{c2} \sim 10^5$, and the turbulence is attenuated when $Pa_{c1} < Pa < Pa_{c2}$. The particles with $Pa > Pa_{c2}$ or $Pa < Pa_{c1}$ will augment the carrier phase turbulence. The previous data summarized by Tanaka and Eaton [2008], which includes turbulence modulation in air (indicated by circular markers) and also augmentation in a liquid (indicated by square symbols), are shown in Figure 4.13a. In order to evaluate the established criterion at a higher range of Re, the cases from the current experiments that have a modulation larger than 2% have also been added to Figure 4.13a. These cases include the 700 µm particles at Re of 75,000, 100,000 and 125,000 at $\phi_v = 0.05\%$ and also the 340 µm particles at Re = 125,000 and $\phi_v = 0.18\%$. The particle momentum number is close to Pa_{c1} for these four data points, and the liquid phase turbulence increases as predicted using the criterion of Tanaka and Eaton [2008]. The variation of turbulence modulation with Pa for the aforementioned cases is depicted in Figure 4.13b. These data points fall within the range of $620 < Pa < 1200$. An increase in M with the increase in Pa is observed in this range, implying that turbulence augmentation in water can probably also occur at $Pa > 10^3$. The turbulence intensity of the liquid phase in two-phase flow is

compared with the turbulence intensity of the solid phase at the channel centerline using the relative turbulence intensity (R_{TI}), defined as

$$R_{TI}(\%) = \frac{\sqrt{\langle u^2 \rangle_b} - \sqrt{\langle u^2 \rangle_l}}{\sqrt{\langle u^2 \rangle_l}} \times 100, \tag{4.3}$$

where the subscript b refers to the beads, and l denotes the liquid phase. The results for the conditions shown in the first row of Table 4.1 are displayed in Figure 4.14. A number of previous experiments were also examined, and the corresponding relative turbulence intensity was estimated. The results are also presented in Figure 4.14. The collected experimental data includes gas-solid flow in a channel [Kulick et al., 1994, Lain et al., 2002, Wu et al., 2006] and pipe [Lee and Durst, 1982, Varaksin et al., 2000] in horizontal and vertical orientations. Gas flows result in larger St than liquid flows at any given Re. The data also contains experimental measurements in vertical liquid flow with ceramic, polystyrene [Alajbegovic et al., 1994], and glass [Kameyama et al., 2014] beads. The details of these experiments are summarized in Table 4.4. The table highlights the lack of any measurement of turbulence intensity in a horizontal solid-liquid channel as addressed by the current investigation.

Table 4.4: Summary of previous experiments used to estimate the relative turbulence intensity (R_{TI}) of the solid and liquid phase.

Ref.	Flow descriptions	Carrier phase	Particles	Re
Alajbegovic et al. [1994]	Upward pipe	Water	Ceramic	$60–92\times10^3$
Alajbegovic et al. [1994]	Upward pipe	Water	Polysterene	$60–92\times10^3$
Lee and Durst [1982]	Upward pipe	Air	Glass	15×10^3
Kulick et al. [1994]	Horizontal channel	Air	Glass	15×10^3
Varaksin et al. [2000]	Horizontal pipe	Air	Glass	15×10^3
Lain et al. [2002]	Horizontal channel	Air	Glass	15×10^3
Wu et al. [2006]	Horizontal channel	Air	Polythene	15×10^3
Kameyama et al. [2014]	Downward pipe	Water	Glass	19.5×10^3

For very low St_K ($< 10^{-3}$) and low ϕ_v, the particles act as tracers. Hence, $R_{TI} \sim 0$ at very low St_K, and gradually increases until $St_K \sim 2$. In the St_K range of the current experiments ($4.1 < St_K < 40.6$), R_{TI} decreases with St_K as shown in Figure 4.14. This

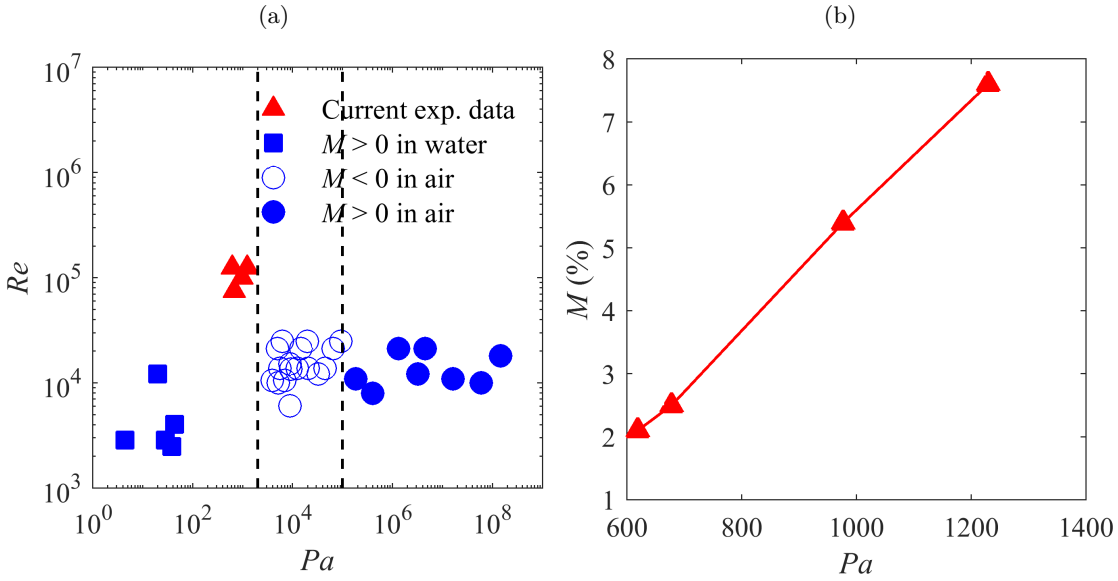

Figure 4.13: (a) Mapping of the experimental data for turbulence modification. The data from the literature are collected by Tanaka and Eaton [2008], which include the turbulence augmentation and attenuation in air, and turbulence augmentation in water that are indicated in blue. The data of the current experiments which correspond to $Pa < Pa_{c1}$ region (augmentation in water) are presented in red. (b) Streamwise turbulence modulation for current experimental data as a function of Pa.

is associated with the reduction of turbulence intensity of the particulate phase due to the decrease in transfer of turbulent kinetic energy to particles with larger St_K. When $St_K > 15$, $R_{TI} < 0$, indicating that the solid phase has smaller turbulence intensity relative to the liquid phase. The line fitted to the current experimental results for a horizontal solid-liquid flow shows that the relative turbulence intensity changes with the St_K as $R_{TI} = -14ln(St_K) + 38.5$.

4.5 Error analysis

The errors due to alignment of the laser sheet, deviation of the time delay between the laser pulses, and change in magnification across the field-of-view are negligible in the current PTV setup. The latter source is small since the observation angle is less than 3°and the working distance is larger than the field-of-view. The uncertainty in measurement of the

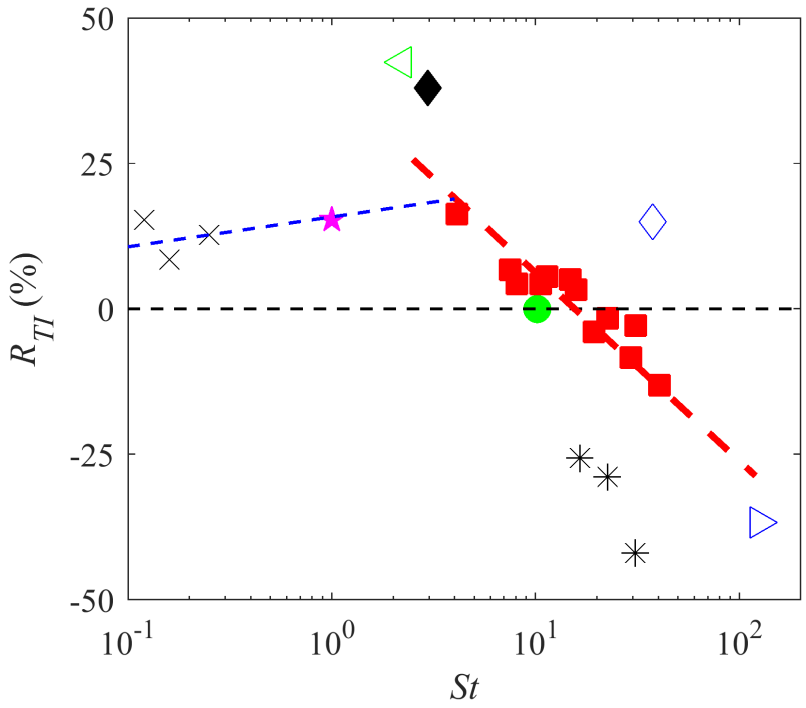

Figure 4.14: The turbulence intensity of the solid phase relative to the liquid phase as defined in Eq. 4.14. The results of the current experiment (■) are fitted by $R_{TI} = -14ln(St_K)+38.5$ (– –). The other symbols show the relative turbulence intensity obtained from Alajbegovic et al. [1994] for polystyrene (×) and ceramic particles (∗), Lee and Durst [1982] (▷), Kulick et al. [1994] (•), Varaksin et al. [2000] (◁), Lain et al. [2002] (◊), Wu et al. [2006] (♦), and Kameyama et al. [2014] (⋆). The experimental conditions of these works are summarized in Table 4.4.

channel height can also lead to error in calculating the scaling factor. This is estimated to be about $\varepsilon_M = 7.3 \times 10^{-5}$ mm/pixel based on an assumed uncertainty of 0.1 pixel. The main source of random error in PTV algorithm is due to overlapping particle images, low signal-to-noise ratio (SNR), and uncertainty in particle location [Kähler et al., 2012]. The error associated with the overlapping particles is negligible here because of the small number of glass beads in the each image. The SNR is also enhanced by subtraction of the minimum value over an ensemble of images. In the current study, the PTV algorithm is followed by cross-correlation of two interrogation windows around the particle pair (as presented in Figure 3.3). The cross-correlation reduces the uncertainty associated with the inaccurate estimation of glass beads position with a large non-Gaussian intensity. The remaining error

in determining the displacement based on the cross-correlation with sub-pixel accuracy is about $\varepsilon_{cc} = 0.1$ pixel [Westerweel et al., 1997]. The root mean square (rms) uncertainty of the particle displacement $\varepsilon_{\Delta s}$ is given by

$$\varepsilon_{\Delta s} = \sqrt{(M\varepsilon_{cc})^2 + \left(\frac{\Delta s}{M}\varepsilon_M\right)^2} \tag{4.4}$$

where M is digital resolution and Δs is the particle displacement between frames that varies from 12 pixel near the wall to 20 pixel at the channel centerline. The computed $\varepsilon_{\Delta s}$ is about 1.5×10^{-3} mm across the channel. The rms uncertainty of the instantaneous velocity ε_U is estimated using

$$\varepsilon_U = \sqrt{\left(\frac{1}{\Delta t}\varepsilon_{\Delta s}\right)^2 + \left(\frac{\Delta s}{\Delta t^2}\varepsilon_{\Delta t}\right)^2} \tag{4.5}$$

The error in the mean velocity, velocity fluctuation, and turbulence intensity is calculated using the error propagation method. The normalized uncertainty at the middle of channel and also near the wall is reported in Table 4.5.

Table 4.5: Summary of rms measurement uncertainty estimated using error propagation method.

Parameter	$y/h = 0.05$	$y/h = 0.25$	$y/h = 0.5$
ε_U (mm/s)	28.8	30.7	32.7
$\varepsilon_{\langle U\rangle/U_c}$	4.7×10^{-5}	5.5×10^{-5}	7.8×10^{-5}
$\varepsilon_{\langle u^2\rangle/U_c^2}$	7.9×10^{-6}	7.1×10^{-6}	6.4×10^{-6}
$\varepsilon_{\langle v^2\rangle/U_c^2}$	3.8×10^{-6}	3.4×10^{-6}	4.3×10^{-6}
$\varepsilon_{\langle uv\rangle/U_c^2}$	4.4×10^{-6}	4.0×10^{-6}	3.9×10^{-6}

An alternative method to estimate the random error is through statistical convergence of the $\langle U\rangle$, $\langle u^2\rangle$, $\langle v^2\rangle$ and $\langle uv\rangle$ of the solid phase at the channel centerline as shown in Figure 4.15. The statistics reach a plateau after about 3000 data points. The random error is also estimated using the difference between the maximum and minimum values in the last 3000 data points at three locations. The estimated errors are shown in Table 4.6 for comparison with the results of Table 4.5. It can be seen that the estimation based on statistical convergence results in larger uncertainty than the error propagation method.

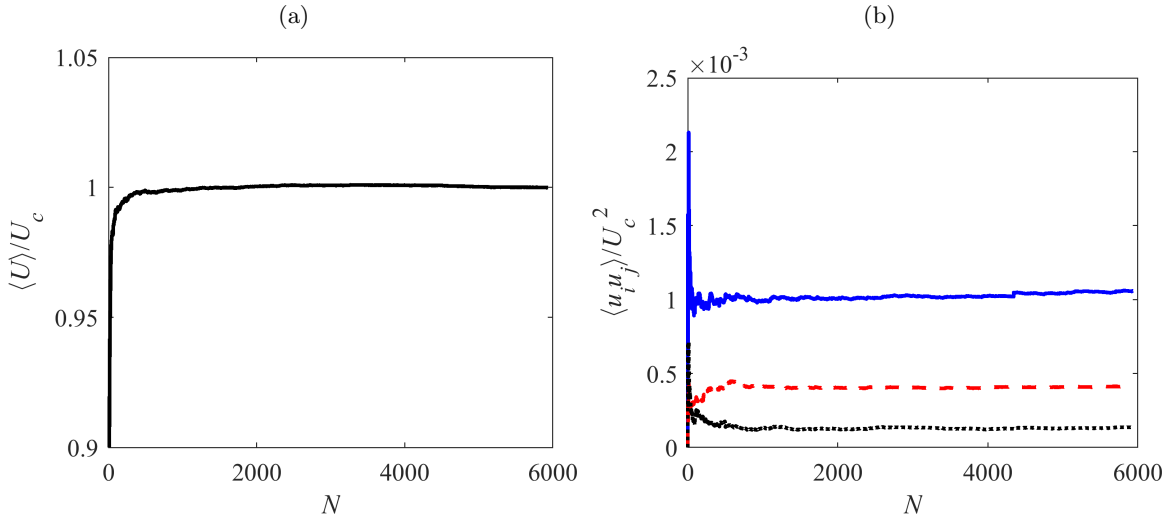

Figure 4.15: The convergence of (a) mean velocity, (b) Reynolds stresses of the solid phase at the channel centerline for flow with $d_b = 530$ µm particles at Re of 100,000.

Table 4.6: Summary of rms measurement uncertainty estimated using error propagation method.

Parameter	$y/h = 0.05$	$y/h = 0.25$	$y/h = 0.5$
$\varepsilon_{\langle U \rangle / U_c}$	6.1×10^{-4}	4.3×10^{-4}	1.1×10^{-3}
$\varepsilon_{\langle u^2 \rangle / U_c^2}$	1.2×10^{-4}	2.9×10^{-5}	4.9×10^{-5}
$\varepsilon_{\langle v^2 \rangle / U_c^2}$	6.4×10^{-5}	2.1×10^{-5}	1.4×10^{-5}
$\varepsilon_{\langle uv \rangle / U_c^2}$	2.5×10^{-5}	1.8×10^{-5}	1.6×10^{-5}

4.6 Conclusion

The turbulence of both the solid and liquid phases for flow of two-phase mixtures in a horizontal channel was investigated using PIV/PTV techniques. Flows with Re of 50,000, 75,000, 100,000 and 125,000 were investigated to study the effect of Re on turbulence statistics for different particle sizes. Glass beads of $d_b = 285$, 530, and 700 µm were used to investigate the effect of particle size at Re of 50,000 and 125,000. The effect of volumetric concentration of the particulate phase was also studied over the range $0.03\% \leqslant \phi_v \leqslant 0.18\%$. The instantaneous velocity of the liquid phase was obtained using cross-correlation, and the solid phase velocity was measured by particle tracking from a common set of images.

The results demonstrated that smaller particles (d_b = 285 µm) were slower than the liquid phase at all Re tested, over the region $0.03 < y/h < 0.5$ where statistically reliable data for the particulate phase was available. Larger particles at higher Re lead the flow in the near-wall region while their velocity was lower than the liquid phase at $y/h > 0.3$. The mean streamwise velocity of the solid phase increased near the wall with increasing St. The crossing point, which shows the point where the particle and liquid velocities are equal, moved toward the channel centerline with increase of St.

In general, larger particles produced a greater increase in streamwise and wall-normal turbulence intensity of the carrier phase. In case of the largest particles (d_b = 700 µm), the liquid phase turbulence intensity was larger than the unladen flow, and the turbulence was augmented as Re increased. A maximum turbulence modulation of 7.6% was observed for d_b = 700 µm at Re = 125,000. This was associated with the large particle Reynolds number ($Re_p \sim 250$) in the near-wall region, which was large enough to generate vortex shedding and enhance carrier phase turbulence. Larger turbulence in the carrier phase strengthens the dispersion of particles and prevent sedimentation. The measured turbulence modulation was shown to be reasonably well predicted using the criterion established by Tanaka and Eaton [2008].

The investigation of solid phase velocity fluctuations showed that the streamwise and wall-normal turbulence intensity of the solid phase decreased as the particle size and Re increased (i.e., with increasing St). Smaller velocity fluctuation of the particles in the near-wall region corresponds to a smaller particle-particle and wall-particle collision frequency which reduces the amount of surface erosion. Comparison with the literature revealed that there is a critical Stokes number (St_{cr}) which divides the variation of particle turbulence into two regimes. For $St < St_{cr}$, the turbulence intensity of the solid phase increases with St while it decreases for $St > St_{cr}$. The turbulence intensity of the solid phase was also compared to the liquid phase turbulence using R_{TI}, the relative turbulence intensity. The results showed that R_{TI} varies with the St_K as $R_{TI} = -14ln(St_K) + 38.5$ for the St_K range of the current experimental study.

The particle number density distributions indicated that at relatively low Re and large particle size, when the particle terminal settling velocity was much larger than the friction velocity, the particle number density increased monotonically from the center of the channel towards the bottom wall. The distribution of particles became more uniform with increasing Re, since the turbulent dispersion force increases with increasing Re. A local minimum was observed in the particle number density profile at $y/h \sim 0.15$ for the largest particles ($d_b =$ 700 µm) at the highest Re tested here ($Re =$ 125,000).

It was determined that varying the particle concentration from 0.03% to 0.18% had no significant effect on the solid phase turbulent statistics but does affect the liquid phase turbulence intensity, especially the wall-normal Reynolds stress. It is concluded that over this range of particle concentrations, there is no interaction between particles, and the liquid and solid phases interact through two-way coupling.

Chapter 5

Particle-Turbulence Interaction

This chapter investigates the interaction between particles and turbulent flow by simultaneous measurement of the time-resolved three-dimensional (3D) velocities of particles and the carrier liquid phase. The measurement system is explained in Section 3.3. The investigation is conducted in the horizontal channel flow at a bulk Reynolds number of 20,000. The suspension contains nearly neutrally buoyant beads with a density of 1.05 g/cm^3 and a mean diameter of 370 µm at a volumetric concentration of 0.1%.

5.1 Introduction

In turbulent wall flows, suspended particles that are heavier than the liquid phase move successively toward and away from the bottom wall [Sumer, 1974, Sutherland, 1967]. Sumer and Oguz [1978] applied a photographic technique and recorded the trajectory of inertial particles over a smooth surface. They concluded that the ejection motions of the liquid phase transport the particles away from the wall and generate a negative streamwise velocity fluctuation [Sumer and Oguz, 1978, Rashidi et al., 1990, Ji et al., 2013]. Once the ejection motion attenuates, the suspended particles gradually approach the wall and may be lifted up again by another ejection motion, keeping the inertial particles suspended. For inertial particles that are smaller than the viscous sublayer thickness, it was observed by Yung et al. [1989] that the particles initially slide on the wall and then are lifted up by ejection motions.

The interaction of particles with the liquid phase has traditionally been investigated

based on whether the particles ascend from, or descend to, the bottom wall. The ascending particles typically originate from the slower near-wall flow, and therefore they have a lower mean streamwise velocity than the descending particles [Nino and Garcia, 1996]. To observe the relation between particle motion and that of the surrounding fluid, Kiger and Pan [2002] performed a simultaneous planar PIV of inertial particles and their surrounding liquid flow. They confirmed a preferential accumulation of ascending particles in the ejection motions, while less accumulation of descending particles was observed in the sweep motions of the liquid phase. It was shown by Lelouvetel et al. [2009] that the quadrant distribution of liquid velocity fluctuations around the descending particles was similar to that of the unladen flow, suggesting a lack of correlation between the descending beads and the liquid phase turbulence. In contrast, more than half of the ascending particles were located in the ejection motions of the liquid phase, which showed a stronger correlation between ascending particles and the surrounding fluid. A poorer correlation of descending beads with sweep motions was also observed by van Hout [2011] in a square channel flow for nearly neutrally buoyant particles.

A few investigations have shown that a suspension of particles is not restricted to streamwise plus ascending and descending motions. The direct numerical simulations of Brooke et al. [1992] showed that inertial particles also have a strong spanwise velocity. In an experimental study of polystyrene beads [Kaftori et al., 1995], the ascending and descending motion of the beads was associated with streamwise vorticity. Using DNS, Marchioli and Soldati [2002] observed that sweep and ejection motions are generated by the downwash and upwash sides of quasi-streamwise vortices. Their DNS was carried out for particles smaller than the inner length scale, and with a $St^+ = 30$. Here, St^+ was calculated as the ratio of the particle response time to the inner time scale of the turbulent flow. The volumetric concentration of particles was also $6.0 \times 10^{-3}\%$, which indicates a one-way coupling where the particles have a negligible effect on the flow statistics [Elghobashi, 1991]. However, the role of the spanwise motions and quasi-streamwise vortices in transport of larger particles and at higher volumetric concentrations still needs to be evaluated.

The investigation of the turbulent fluid flow surrounding finite-size particles has been limited by challenges in both numerical simulations and experimental techniques. A large number of numerical simulations have applied the classical point-particle method for modeling particles that are smaller than the smallest turbulent eddies present in the flow, examples include studies by Zhao et al. [2013] and Lee et al. [2015]. These investigations have resulted in significant progress for understanding the behavior of sub-Kolmogorov particles [Soldati and Marchioli, 2009, Sardina et al., 2012]. However, such a method may not be applicable to finite-size particles since it only considers the quasi-steady drag force, while forces such as lift, added-mass, and Basset history forces are neglected. For an accurate simulation of flow surrounding finite-size particles, advanced interface resolved simulations are required (e.g. Lashgari et al. [2016] and Costa et al. [2018]). Furthermore, measurement of the liquid phase surrounding finite-size particles is also experimentally challenging because of blockage effects and strong reflections of the laser light by the large particles. The few available experiments have also been limited to a wall-normal-streamwise plane, which does not provide access to the spanwise motion of the particles and the surrounding fluid.

In the current investigation, the analysis in the literature is extended to higher particle concentration, and the three-dimensional (3D) motion of the flow surrounding the particles is investigated. The acceleration of particles is used to elucidate the momentum exchange of the particles with the surrounding fluid. It is suggested that a particle sampling approach using particle acceleration can be more effective since it indicates momentum exchange between the particles and the surrounding flow. Simultaneous 3D measurement of particles and the surrounding fluid velocity is carried out in a suspension of nearly neutrally buoyant beads in a horizontal turbulent channel flow of water at a $Re = 20{,}000$. Large particles with a normalized diameter, d_b^+, of 26 are used. Here, d_b^+ is bead diameter normalized by the wall unit. The volume concentration is 0.1%, in which two-way coupling between particles and fluid is expected. Time-resolved volumetric particle tracking velocimetry based on the shake-the-box (STB) algorithm [Schanz et al., 2016] is performed. This PTV method makes it possible to perform measurements at relatively high particle volumetric concentrations

(0.1%), in comparison with the previous 3D-PTV measurements in particle-laden flows, such as 0.03% [Suzuki et al., 2000] and 1.4×10^{-3}% [Oliveira et al., 2015, 2013]. Based on particle wall-normal motion and acceleration, Lagrangian particle trajectories are obtained and used to conditionally sample the surrounding fluid. The 3D trajectories of the beads are also inspected for their 3D motion.

5.2 Experimental conditions

The experiments were performed at a constant mass flow rate of 2.08 kg/s, i.e. Re = 20,000 based on the full channel height and the average velocity, U_{avg}, of 1.16 m/s. The friction Reynolds number, Re_τ, was 545, defined based on the half channel height and friction velocity, u_τ. The flow loop also utilized a double-pipe heat exchanger to maintain the fluid temperature at 25 $\pm$ 0.1°C. For the particulate phase, polystyrene spherical beads with a density (ρ_b) of 1.05 gr/cm^3, and at a volumetric concentration (ϕ_v) of 0.1%, were used. The mean diameter of beads (d_b) was 370 µm with a standard deviation of 35 µm. The size distribution of the beads was obtained from 30,000 two-dimensional images with a digital resolution of 69 pix/mm. The images were processed using the 'imfindcircle' function (MATLAB R2015b, MathWork), which uses Circle Hough Transform (CHT) [Atherton and Kerbyson, 1999] to find the diameter of the beads. About 61% of the data were within one standard deviation of the mean.

The liquid flow was also seeded with 2 µm silver-coated glass beads (SG02S40 Potters Industries) at a concentration of 8×10^{-3}% (by volume) to obtain the velocity of the fluid phase. These tracer particles had a density of 4.0 gr/cm^3 and were seven times smaller than the wall unit. Their response time is 1.0 µs with $St = 3.2 \times 10^{-3}$. The latter was calculated using the inner time scale of the turbulent flow, as will be discussed in the following paragraphs.

The analysis of the velocity field in this chapter is carried out using dimensionless numbers, which are normalized by outer and inner scales of the turbulent channel flow. The average velocity of unladen flow across the channel height (U_{avg}) and the channel height

(h) are used as the outer velocity and length scales, respectively. Inner scaling includes the friction velocity, u_τ, and the inner length scale (λ) of the unladen flow, which are equal to 0.062 m/s and 14.05 µm, respectively. The inner scaling is obtained using the Clauser method [Clauser, 1956], and the quantities normalized using inner scaling are indicated by a superscript '+'. The turbulent scales are estimated from the 3D-PTV measurements of the mean velocity profile. The inner length scale of the flow results in $d_b^+ = d_b/\lambda = 26$.

The viscous time scale, $\tau_v = \nu/u_\tau^2$, is considered as the charateristic time scale of flow. The bead response time, τ_b, is also calculated using Eq. 2.29. The estimated time scales are $\tau_v = 0.23$ ms and $\tau_b = 9.2$ ms, which result in a bead St^+ of 40.0. This estimation of St^+ applies to the inner layer, since the flow time scale increases with distance from the wall. The local St is expected to reach its minimum value at the center of the channel. The settling parameter, $V_s/\kappa u_\tau$, is about 0.2, showing that the effect of gravity is small. In this parameter, V_s is the terminal settling velocity of the beads and κ is the von Kármán constant [Sumer and Oguz, 1978, Marchioli et al., 2008]. The estimated Shields number, $\left(\rho_f u_\tau^2\right) / \left(\left[\rho_p - \rho_f\right] g d_p\right)$, is about 15, which also indicates small gravitational effects with respect to wall shear stress [Miller et al., 1977]. For the current volumetric concentration of 0.1%, the ratio of the mean distance between the beads (S) to bead diameter (d_b), S/d_b, is 12. According to the criterion suggested by Elghobashi [1991], a small probability of particle-particle collision exists at $\phi_v = 0.1\%$, and $S/d_b \sim 12$.

The investigations of van Hout [2011] and Shao et al. [2012] were carried out on particle-laden flows of solid-liquid in horizontal channels, and with similar particle-laden conditions as the current experiments. van Hout [2011] experimentally investigated the dynamics of nearly buoyant polystyrene beads with $d_b^+ = 12$ and $St = 0.27$. Shao et al. [2012] carried out a direct numerical simulation of beads with $\rho_b \sim 1.5\rho_f$, $d_b/h = 0.025$ (the same as the current experiment), and $d_b^+ = 10$. Both studies showed preferential distribution of beads in the low-speed region, suggesting its possibility for the current investigation.

For the results presented in this chapter, the channel height is divided into 0.5 mm ($0.03h$) bins with 50% overlap to calculate the mean velocity and turbulence intensities. To

obtain the fluid velocity surrounding a bead, the velocity of tracer particles is averaged in a cubic volume, where the bead is located at its center. Different volume sizes were evaluated, and it was found that the results are independent of the volume size when the volume is smaller than $1.4 \times 1.4 \times 1.4$ mm^3 ($3.8d_b \times 3.8d_b \times 3.8d_b$). This cubic volume around the bead is referred to as the 'surrounding' fluid.

The instantaneous velocity components are indicated by U, V, and W in the streamwise, wall-normal, and spanwise directions, respectively. The instantaneous velocity is decomposed into mean, indicated by the symbol $\langle\rangle$, and velocity fluctuations shown by the lower-case letters u, v, and w, e.g. $U = \langle U \rangle + u$. The average wall-normal and spanwise velocities are negligible in channel flow; hence, for these two components, $V = v$ and $W = w$. Similar to Oliveira et al. [2015] and van Hout [2011], the velocity fluctuation of the beads is estimated as the difference between the instantaneous velocity of the bead and the average velocity of the liquid phase at the bead centroid, i.e., $u_b = U_b - \langle U_f \rangle$. The subscripts b and f refer to the bead and fluid phases, respectively.

5.3 Turbulent channel flow

To evaluate the uncertainty of the PTV system, measurements of the unladen flow are compared with the DNS results of Lee and Moser [2015]. The semilogarithmic profile of mean velocity from 3D-PTV in the unladen flow at $Re_\tau = 545$ ($Re = 20{,}000$), along with the DNS results of Lee and Moser [2015] at Re_τ of 543, are shown in Figure 5.1a. The measurements deviate from the law of the wall in the linear viscous sublayer ($y^+ < 5$), but the difference diminishes with increasing y^+. The discrepancy between 3D-PTV and DNS is smaller than 1.0% at $y^+ > 15$ ($y/h > 0.015$), which is equivalent to $0.1u_\tau$, or 0.02 pixel error in the estimation of particle displacement. The measurements agree with the logarithmic law, $\langle U_f \rangle^+ = 1/\kappa \ln(y^+) + B$, where the von Kármán constant, κ, is equal to 0.384 and $B = 4.6$. This agreement confirms the accuracy of mean velocity at $y^+ > 5$ and the fully developed state of the turbulent channel flow. The large uncertainty at the near-wall region of $y^+ < 5$ is associated with the smaller displacement of the particles between

the two laser pulses, maximum of 1 pix displacement. Another source of uncertainty in this region is due to glare spots caused by the reflection of the laser from the surface. These reflections interfere with particle detection and also skew the calibration map during the self-calibration process. The mean disparity for the first calibration plane above the wall is 0.039 pix with a standard deviation of 0.019 pix. This is larger than 0.026 pix mean disparity and 0.017 pix standard deviation for the entire domain.

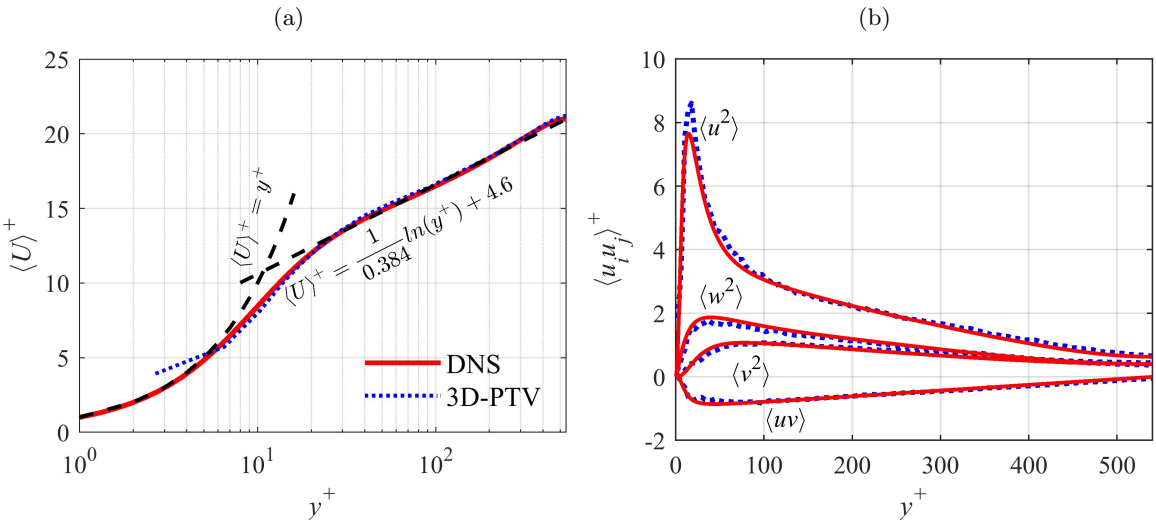

Figure 5.1: Profiles of the normalized (a) mean streamwise velocity and (b) Reynolds stresses for the unladen flow at $Re_\tau = 545$. The results are compared with the channel flow DNS results of Lee and Moser [2015] at $Re_\tau = 543$.

All four nonzero components of the Reynolds stress tensor for the unladen flow, obtained from 3D-PTV measurements, are shown in Figure 5.1b and are also compared with the DNS results of Lee and Moser [2015]. In general, the Reynolds stresses agree with the DNS. At $y^+ > 15$, the maximum absolute error relative to DNS is equivalent to 0.03, 0.02, and 0.02 pixels for $\langle u_f^2 \rangle$, $\langle v_f^2 \rangle$, and $\langle w_f^2 \rangle$, respectively. However, the smaller displacements in the y and z directions result in larger relative errors in $\langle v_f^2 \rangle$ and $\langle w_f^2 \rangle$. For example, the maximum discrepancy is 12.9% at $y^+ = 26$ for $\langle v_f^2 \rangle$. Overall, comparison of the 3D-PTV with the DNS results shows that measurements are accurate at $y^+ > 15$ ($y/h > 0.015$) with a maximum uncertainty of $0.1u_\tau$ (0.02 pixel) for the mean velocity and $0.15u_\tau$ (0.03 pixels)

for the Reynolds stresses.

Figure 5.2 shows the mean velocity and Reynolds stresses of the beads and the surrounding liquid phase obtained from the simultaneous 3D-PTV measurements. In Figure 5.2a, at $y^+ > 20$, the beads have a slightly lower mean velocity than the fluid. This suggests preferential accumulation of the beads in low-speed regions [Kiger and Pan, 2002], as will be discussed in the next section. At smaller distances from the wall ($y^+ < 20$), the bead velocity is higher than the fluid velocity, which is associated with the rolling and sliding motions of the beads along the wall. These motions relax the no-slip boundary condition, i.e., the beads have a finite slip velocity at the channel wall. Figure 5.2b shows that the beads have larger Reynolds stresses than the fluid phase across the bottom half of the channel, although the difference is smaller for $\langle v^2 \rangle$ and $\langle uv \rangle$. The larger Reynolds stresses are associated with the relaxation time and St of the beads, which allows them to maintain their velocity for a longer time when transported in the wall-normal direction. As a result, the beads have a wider velocity distribution, which results in larger Reynolds stresses. Figure 5.2b also shows that the difference between the intensities of the beads and the fluid phase decreases closer to the center of the channel. In this region, the local St is smaller and the beads follow the fluctuations more closely.

In addition to the comparison with DNS results described earlier, an uncertainty analysis based on statistical convergence is conducted (see Section 5.7) to estimate the random error. The estimated errors for the mean flow and Reynolds stresses are shown using error bars in Figure 5.2 at selected wall-normal locations.

5.4 Ascending and descending beads

In this section, the velocity of the beads and their surrounding fluid is investigated by applying conditional sampling based on the wall-normal bead motion (ascending or descending). The reason for this sampling is to explore the fluid motions responsible for the upward and downward bead motions, which are subsequently important in the entrainment and deposition processes. The conditionally averaged parameters are indicated by subscript c. From

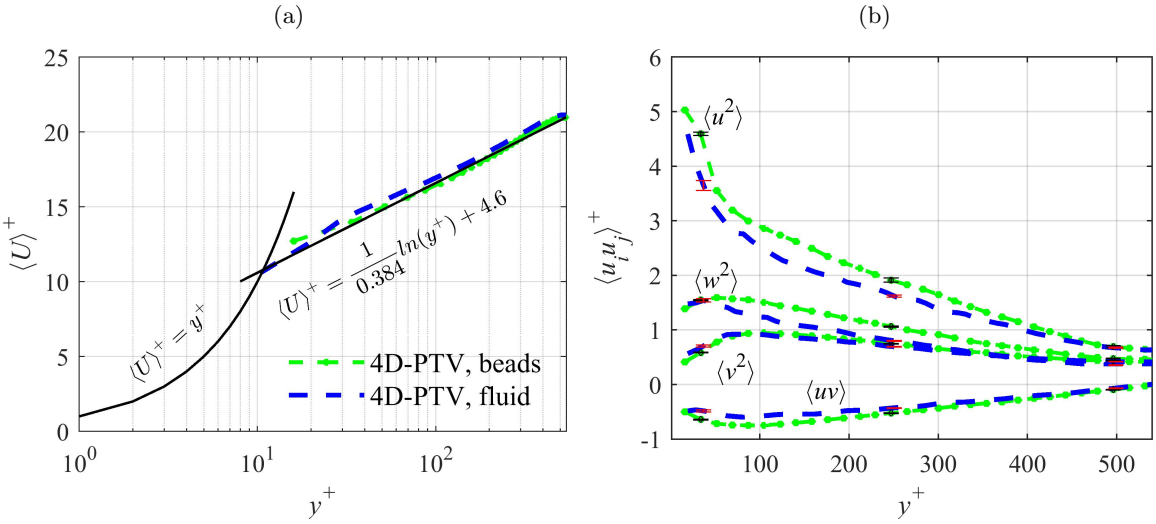

Figure 5.2: Profiles of the normalized (a) mean streamwise velocity and (b) Reynolds stresses for the beads and carrier fluid phase at $Re_\tau = 545$ and $\phi_v = 0.1\%$ measured by 3D-PTV. The error bars show the estimated uncertainty based on Section 5.7. Only three locations are chosen to show the error bars for clarity.

a total of 1.7×10^7 detected bead images, 54% had a descending motion and the remaining 46% were ascending, i.e. away from the wall. The slightly greater number of descending beads is hypothesized to be related to the fact that the beads are slightly heavier than the fluid phase ($\rho_b/\rho_f = 1.05$).

5.4.1 Conditionally averaged velocity

The conditionally averaged streamwise velocity of the beads and their surrounding fluid, based on ascending ($V_b > 0$) and descending ($V_b < 0$) beads, is shown in Figure 5.3a. The figure also shows the ensemble velocity of the fluid (without conditional sampling) as a baseline for comparison. The ascending beads and the surrounding fluid have a lower velocity than the ensemble fluid velocity. This velocity lag was also observed by Kiger and Pan [2000] and van Hout [2011] and suggests preferential accumulation of the ascending beads in the low-speed regions. On the other hand, the descending beads and their surrounding fluid have approximately the same velocity as the ensemble fluid velocity. This agrees with the observation of Kiger and Pan [2002] that the descending beads do not demonstrate

any preferential clustering and are evenly distributed in high- and low-speed regions. The comparison of the beads and the fluid velocity in Figure 5.3a also shows that the apparent slip velocity, defined as $\langle U_f \rangle_c - \langle U_b \rangle_c$, is positive and larger for the ascending beads. The maximum slip velocity of the ascending beads is about 8% of the ensemble fluid velocity and occurs at $y/h \sim 0.1$ ($y^+ \sim 100$), which is located in the outer layer.

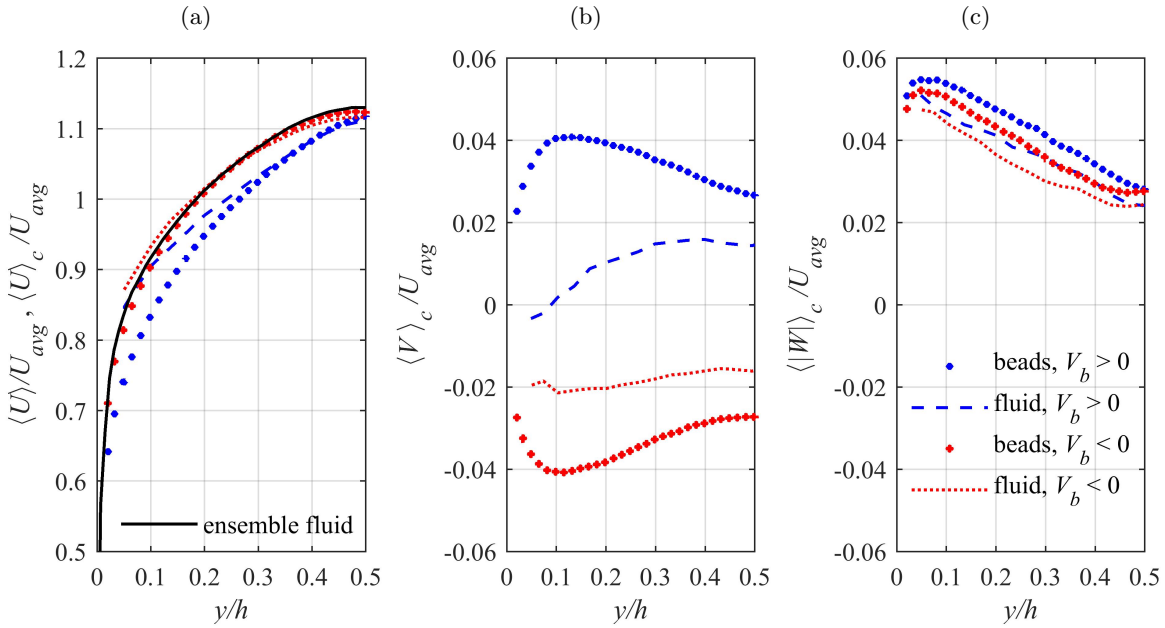

Figure 5.3: Conditional average of (a) streamwise, (b) wall-normal, and (c) absolute spanwise velocity of the beads and their surrounding fluid based on the wall-normal direction of the beads.

The conditional averages of wall-normal and spanwise velocities, based on ascending and descending beads, are presented in Figures 5.3b and 5.3c. The $\langle V_b \rangle_c$ profiles are symmetric for the ascending and descending beads with equal magnitudes but opposite sign. However, $\langle v_f \rangle_c$ is less than $\langle V_b \rangle_c$, which suggests a velocity lag or a reduced correlation between bead and fluid velocity in the wall-normal direction. Bead inertia (i.e., finite St) is expected to result in wall normal velocities that persist longer than those of the surrounding flow, which contributes to the larger values $\langle V_b \rangle_c$.

Figure 5.3c presents the conditional average of the absolute value of the spanwise velocity, $\langle |W| \rangle_c$, for ascending and descending beads and their surrounding fluid. The absolute

value is used to prevent zero averages caused by spanwise symmetry of the flow. For both ascending and descending beads, the spanwise velocity is higher than the wall-normal velocity. The $\langle|W|\rangle_c$ of both ascending and descending beads is higher than that of the surrounding fluid. The apparent spanwise slip velocity, $\langle|W_f|\rangle_c - \langle|W_b|\rangle_c$, is lower than the wall-normal counterpart, which suggests a higher correlation between spanwise motion of the beads and the fluid. The figure also shows that the ascending beads have a higher spanwise velocity than descending beads.

5.4.2 Correlation of beads and surrounding fluid motions

To further investigate the fluid-particle interaction, the correlation of ascending and descending beads with the surrounding fluid is estimated. The streamwise correlation is quantified using ρ_u, defined as

$$\rho_u = \frac{\langle u_b u_f \rangle}{\sqrt{\langle u_b^2 \rangle \langle u_f^2 \rangle}} \tag{5.1}$$

Similar correlation coefficients are also defined for the wall-normal and spanwise directions using the corresponding velocity fluctuations, and indicated as ρ_v and ρ_w, respectively. Variation of the correlation coefficients for the ascending and descending beads across the bottom half of the channel is shown in Figures 5.4a-c. With increasing distance from the bottom wall, the correlation coefficient of all the components increases. This occurs because the characteristic time scale of eddies increases with increasing distance from the wall [Tennekes and Lumley, 1972], which reduces the local values of the bead St, making their motion correlate more strongly with the fluid fluctuations.

For streamwise motions at $y/h < 0.2$ ($y^+ < 200$), the descending beads are more closely correlated with surrounding nearby fluid than are the ascending beads. This trend reverses for $y/h > 0.2$, and a stronger correlation is observed for the ascending beads. The relationship is further investigated in Figures 5.5a and 5.5b using quadrant analysis, in which the velocity fluctuations are considered in the four quadrants of a v versus u plot [Willmarth and Lu, 1972]. The quadrants of the plot are indicated by Q_1 ($u > 0$ and $v > 0$), Q_2 ($u < 0$ and $v > 0$), Q_3 ($u < 0$ and $v < 0$), and Q_4 ($u > 0$ and $v < 0$), and they

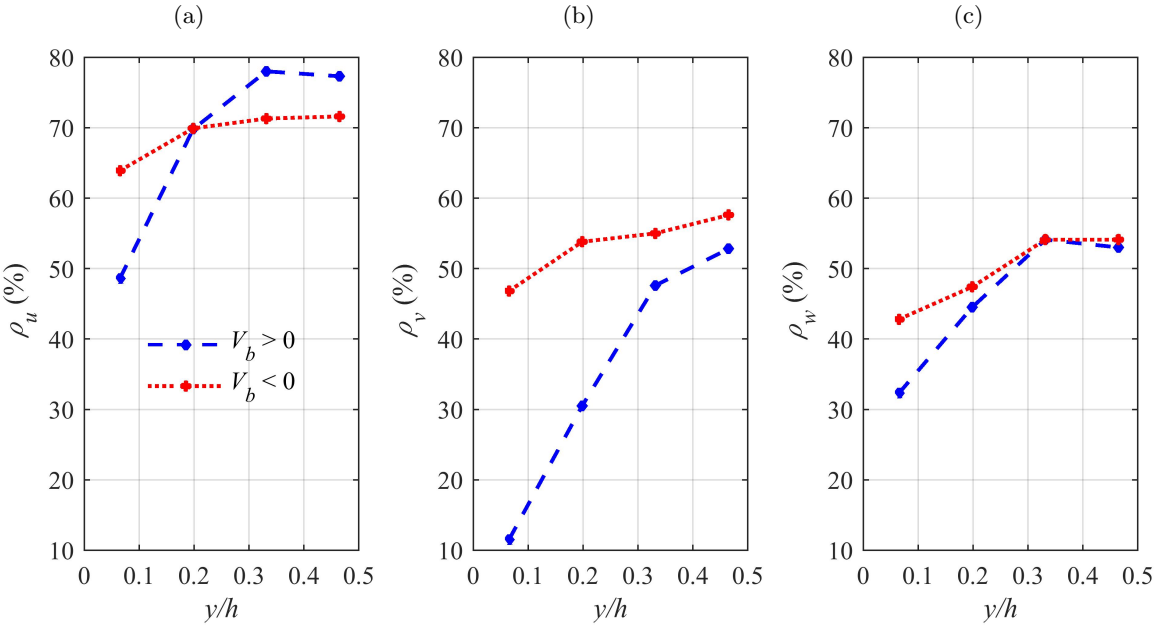

Figure 5.4: The correlation coefficients of ascending and descending beads with their surrounding fluid in (a) streamwise, (b) wall-normal, and (c) spanwise directions.

are referred to as outward interaction, ejection, inward interaction, and sweep, respectively. For each quadrant, the percentage of motion is calculated for the fluid surrounding the ascending and descending beads, and plotted in Figure 5.5. In Figure 5.5a, most of the ascending beads are surrounded by ejection fluid motions, and in Figure 5.5b most of the descending beads are found within sweep events. At $y/h = 0.06$, 33% of the ascending beads are situated in fluid ejections while 48% of the descending beads reside in sweep motions. At $y/h < 0.2$ of Figure 5.4a, this larger percentage of sweep motions by the descending beads results in their larger ρ_u with respect to the ascending beads. With increasing distance from the wall, the fraction of ejection motions around ascending beads increases, while a reduction in sweep events is observed for the descending beads, as shown in Figure 5.5. This explains the larger values of ρ_u for ascending beads at $y/h > 0.2$, shown in Figure 5.4b. Figure 5.4 also shows that ρ_u is stronger than ρ_v and ρ_w because of the greater momentum of streamwise fluid motions.

The correlation coefficient of the wall-normal velocity of the ascending beads and their

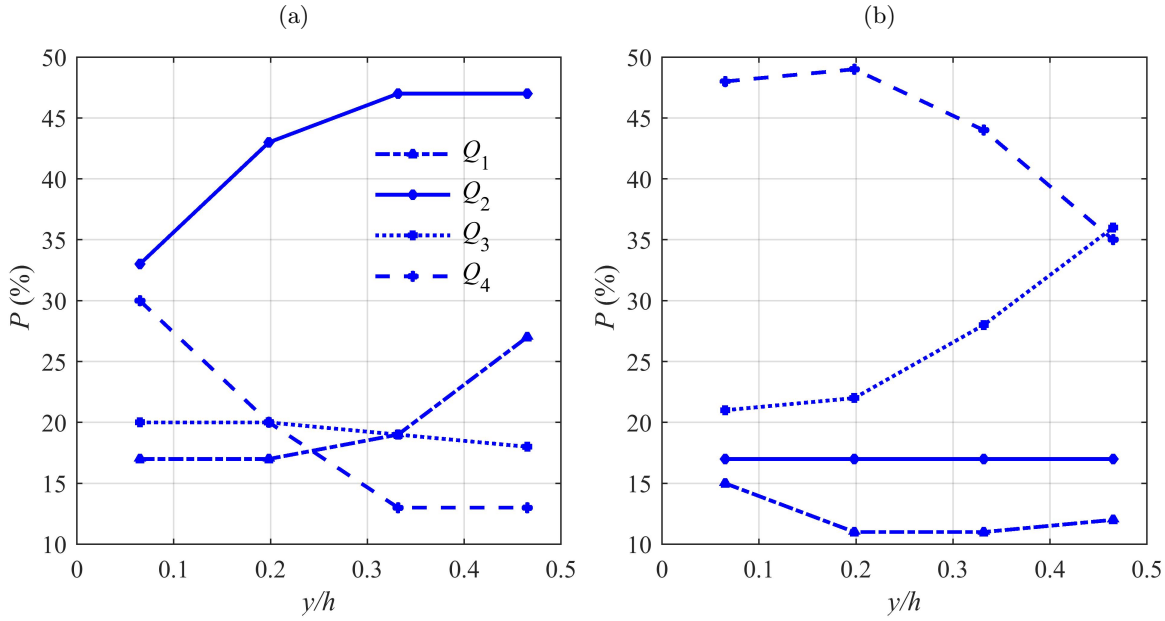

Figure 5.5: The fraction of the fluid surrounding the (a) ascending and (b) descending beads based on the four quadrants of velocity fluctuations.

surrounding fluid is small in the immediate vicinity of the wall (see Figure 5.4b). The small coefficient indicates that the beads do not follow the fluid ejection motions in the wall-normal direction. In Figure 5.4b, descending beads are shown to have larger values of ρ_v than the ascending beads. Comparison of the results of Figures 5.5a and 5.5b also shows that the total fraction of upward-moving fluid (i.e., the sum of fractions in Q_1 and Q_2) surrounding ascending beads is less than the fraction of downward flows (i.e., the sum of fractions in Q_3 and Q_4) around descending beads. This contributes to the larger ρ_v values of the descending beads. A similar trend is shown in Figure 5.4c for correlations in the spanwise direction. Descending beads have a stronger correlation with the surrounding fluid relative to the ascending beads, although the difference in ρ_w for ascending and descending beads is smaller.

To facilitate interpretation of Figure 5.4, the joint probability density function (JPDF) of velocity fluctuations for the ascending and descending beads is presented in Figure 5.6 for the data within $0 < y/h < 0.26$. The JPDFs of u_b and u_f are shown in Figure 5.6a, and the

JPDF of the wall-normal (v_b, v_f) and spanwise (w_b, w_f) velocity fluctuations are shown in Figures 5.6b and 5.6c, respectively. An assumed perfect correlation between the beads and the fluids would collapse the JPDF on the dashed lines shown in the figures (e.g., $u_b = u_f$), while a weak correlation would scatter the data around this line. In Figure 5.6b, as expected, the JPDF of beads with negative and positive v_b covers only half of the figure. A slightly narrower JPDF is observed for the streamwise component of descending beads relative to the ascending beads in Figure 5.6a, showing a stronger correlation of the descending beads with the surrounding fluid. In Figure 5.6a, as expected, the JPDF of ascending beads skews negatively; for ascending beads, u_b and u_f are more likely to be negative. Figure 5.6c shows that ascending and descending beads have a similar JPDF distribution, which agrees with the small difference between ρ_w of ascending and descending beads that is shown in Figure 5.4c. This shows that there is no spanwise preference for the ascending and descending beads.

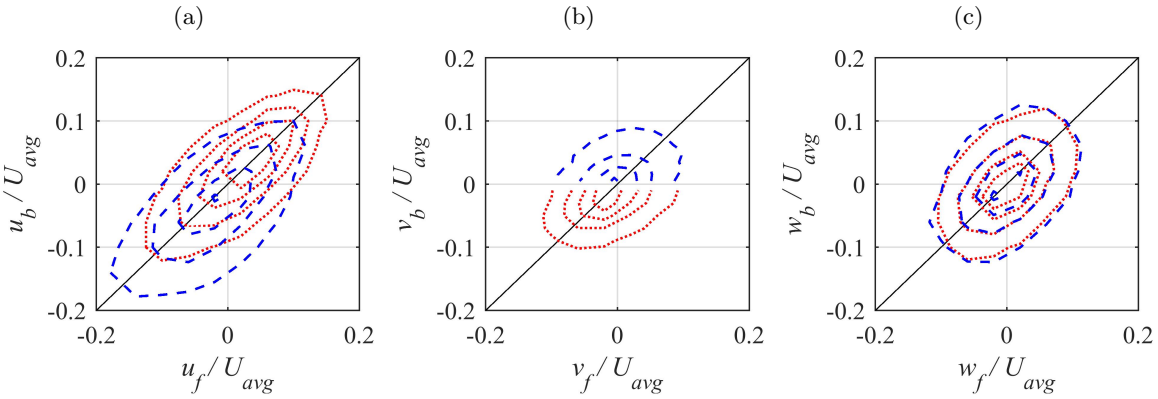

Figure 5.6: JPDF of (a) streamwise (u_f, u_b), (b) wall-normal (v_f, v_b), and (c) spanwise (w_f, w_b) velocity of beads and surrounding fluid for $0 < y/h < 0.26$. The blue dashed contours show the results related to the ascending beads, and red dotted contours represent JPDF of descending beads. The JPDF percentages vary from 1.0% to 8.0% in steps of 2.3% for the most inner to the most outer contour, respectively.

The flow field around particles was also studied by Lelouvetel et al. [2009] and van Hout [2011] using planar PIV. Lelouvetel et al. [2009] studied the accumulation of glass beads in ejection and sweep events in a free-surface channel flow without calculating any correlation

coefficients. The authors stated that the ejection motions of the fluid contribute significantly to the ascending motion of the beads. However, there is no clear correlation between the turbulent events and the descending beads. Their statement does not agree with our results for descending beads presented in this section. This discrepancy can be attributed to the higher density of the glass beads compared with the nearly neutrally buoyant polystyrene beads used in this study. Because of gravity, the glass beads descend independent of the fluid motion, which weakens their correlation with the surrounding flow. In the other study, van Hout [2011] performed experiments in a one-way coupled flow ($\phi_v = 0.014\%$) in a square channel at $Re = 15{,}000$. He observed that ascending polystyrene beads accumulate heavily in ejections at $y^+ > 50$, while descending beads show less accumulation in the sweeps. As presented in Figure 5.5, more ascending beads accumulate in fluid ejections at $y/h > 0.25$ ($y^+ > 250$).

5.4.3 Velocity field around the beads

In this section, the 3D velocity fields around ascending and descending beads are investigated by obtaining the conditionally averaged fluid field in streamwise-wall-normal and streamwise-spanwise planes. For this purpose, similar to the previous sections, the velocity of the surrounding fluid was sampled in a cubic volume of 1.4 $\times$ 1.4 $\times$ 1.4 mm^3 ($0.09h \times 0.09h \times 0.09h$) with the bead located at its center. The conditional samples of the surrounding fluid were then averaged across the bottom half channel $0 < y/h < 0.5$. The obtained conditional averages of fluid velocity fluctuations, $\langle u_f \rangle_c$ and $\langle v_f \rangle_c$, in the XY plane around ascending and descending beads are shown in Figures 5.7a and 5.7b, respectively. In these figures, the streamwise and wall-normal relative locations of the tracers with respect to the bead are indicated as X and Y. The blank region at $Y < 0$ results from the bead blocking the camera's line of sight. The blank region at $Y > 0$ is due to the overlap of the tracer images with the brighter bead image.

The conditional average of Figure 5.7a shows that ascending beads are surrounded by an ejection motion of the fluid phase, in agreement with Kiger and Pan [2002] and Vinkovic

et al. [2011]. The streamwise component of fluid velocity is also slightly larger than the wall-normal component. For the descending beads of Figure 5.7b, the fluid shows a strong motion toward the wall, and the wall normal velocity component of the fluid is significantly larger than its streamwise component. The small streamwise component is associated with a strong contribution of inward fluid motions (i.e., Q_3), which cancels out the streamwise component of the sweep motions. This is consistent with the observation of the results of Figure 5.5b, where both Q_3 and Q_4 were significant around the descending beads. However, this is in contrast to previous investigations that associated only the descending beads with the sweep motions [Kiger and Pan, 2002, Vinkovic et al., 2011]. The data also show that about 45% of descending beads across the bottom half-channel are surrounded by the sweeps, and 29% of descending beads are situated inside inward motions. The larger negative $\langle u_f \rangle_c$ in Figure 5.7a agrees with the results of Figure 5.3a, where the fluid surrounding ascending beads had a lower velocity than that of the ensemble fluid. The small positive $\langle u_f \rangle_c$ in Figure 5.7b also agrees with the slightly higher fluid velocity around descending beads relative to the ensemble fluid velocity. The positive $\langle v_f \rangle_c$ in Figure 5.7a and negative $\langle v_f \rangle_c$ in Figure 5.7b also agree with the $\langle v_f \rangle_c$ sign for ascending and descending beads in Figure 5.3b. The higher wall-normal fluid velocity around descending beads in Figure 5.7b also supports the larger ρ_v of descending beads relative to the ascending ones which was shown in Figure 5.4b.

The conditional average of fluid velocity fluctuations in the streamwise-spanwise plane is shown in Figure 5.8 for the ascending and descending beads. Again, since the average spanwise velocity is zero, the absolute value of the spanwise velocity, $\langle |w_f| \rangle_c$, is used. The figure shows a strong and uniform $\langle |w_f| \rangle_c$ around both ascending and descending beads. The magnitude of $\langle |w_f| \rangle_c$ is similar for both descending and ascending beads. Figure 5.8 shows that the ejection and sweep motions around the beads are accompanied by strong spanwise motions.

In Figures 5.7 and 5.8, the fluid velocity fluctuations were calculated with respect to the ensemble average of the fluid velocity. However, to obtain the instantaneous fluid

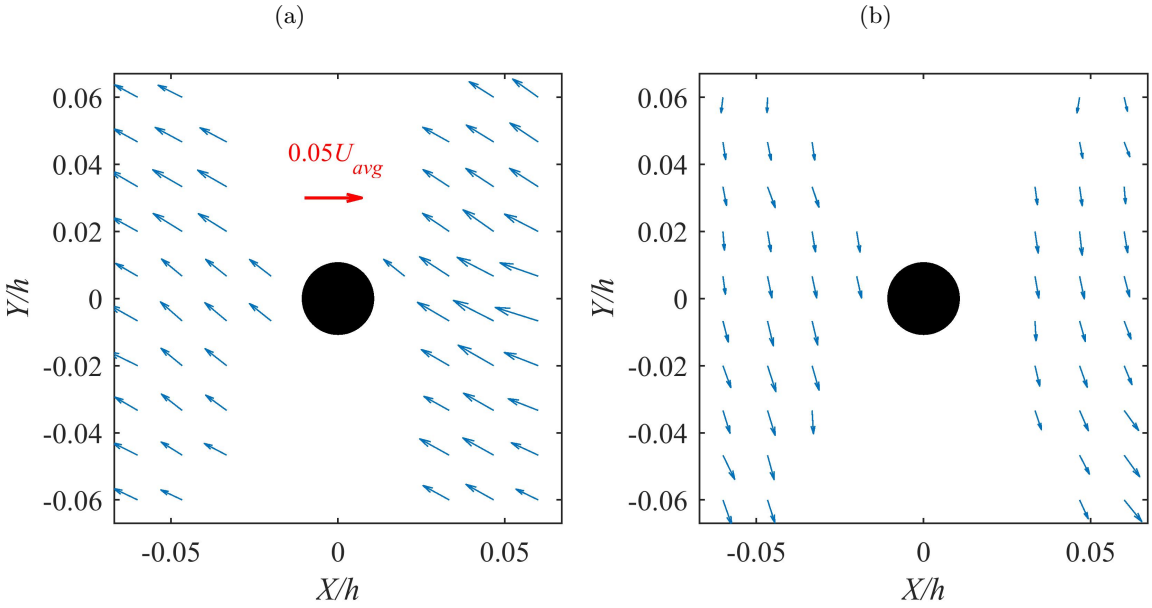

Figure 5.7: Conditional average of fluid velocity fluctuation, $\langle u_f \rangle_c$ and $\langle v_f \rangle_c$, surrounding (a) ascending and (b) descending beads in the XY plane. The red arrow shows the reference vector size.

velocity relative to the bead velocity, the instantaneous tracer velocity must be conditionally averaged with respect to the enclosed bead $\boldsymbol{U}_r = \boldsymbol{U}_f - \boldsymbol{U}_b$. The result produced, for the XY plane, is shown in Figure 5.9. For both ascending and descending beads, the relative streamwise velocity of the fluid is positive above the bead ($Y/h > 0$) and negative below the bead ($Y/h < 0$). This shear layer pattern stems from the positive wall-normal velocity gradient in the lower half of the channel.

In Figure 5.9, it can be seen that the surrounding fluid has a lower wall-normal velocity, i.e., negative $\langle V_r \rangle_c$, with respect to the ascending beads. In contrast, and shown in Figure 5.9b, the fluid has a higher wall-normal velocity with respect to the descending beads, i.e., positive $\langle V_r \rangle_c$, which indicates that descending beads approach the wall faster than does the fluid. This may appear contradictory since the fluid is expected to carry the bead, and not slow it down. A possible explanation is that the wall-normal motion of a bead is initiated by a strong ejection or sweep. The fluid ejection/sweep velocity decays while the bead motion persists because of its longer response time. Therefore, based on conditional

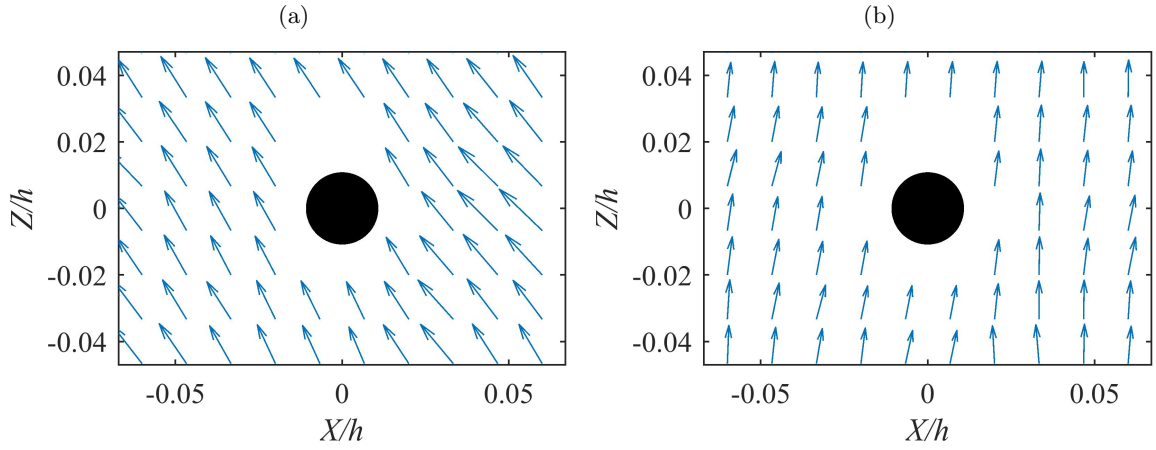

Figure 5.8: Conditional average of fluid velocity fluctuation, $\langle u_f \rangle_c$ and $\langle |w_f| \rangle_c$, around (a) ascending and (b) descending beads in the XZ plane. The vectors are scaled relative to the reference vector shown in Figure 5.7.

averaging, it appears that the beads lead the fluid in the wall-normal direction. A similar observation was made by Righetti and Romano [2004] for conditionally averaged Reynolds shear stress of ejection motions, i.e., $\langle uv \rangle_{Q_2}$. They observed that $\langle uv \rangle_{Q_2}$ of glass beads was larger than that of the fluid phase, which was also associated with the longer time scale of the beads, allowing them to maintain their motion after they are lifted up by strong fluid ejections.

A clockwise vortex is observed in the conditional averages of Figures 5.9a and 5.9b. The ascending beads are mostly located downstream of the vortex core, where $\langle V_r \rangle_c$ is negative, while the descending beads are at the upstream side of the vortex core, where $\langle V_r \rangle_c$ is positive. It is also interesting to note that the superposition of the velocity fields in Figures 5.9a and 5.9b results in a simple shear flow showing the fluid velocity relative to both ascending and descending beads. The velocity gradient of the superposed flow field is $d\langle U_r \rangle / dY = 35 s^{-1}$, which is smaller than $d\langle U_f \rangle / dY = 75 s^{-1}$ of the ensemble fluid velocity at $y/h > 0.02$ ($y^+ > 20$). This smaller gradient shows that the beads are transported by low-shear fluid motions.

The relative velocity fields around ascending and descending beads in the XZ plane are shown in Figure 5.10. The absolute value of the relative velocity is used for the spanwise

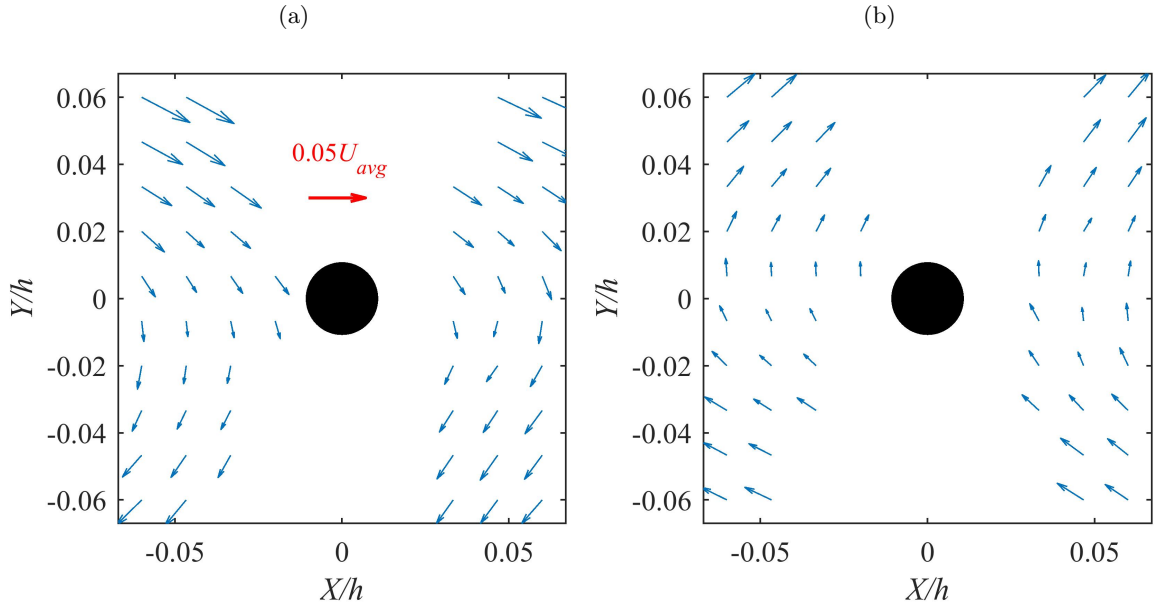

Figure 5.9: Conditional average of fluid velocity relative to the beads, $\langle \boldsymbol{U}_r \rangle_c = \langle \boldsymbol{U}_f - \boldsymbol{U}_b \rangle_c$, in the XY plane for (a) ascending and (b) descending beads. The red arrow shows the reference vector size.

direction, $\langle W_r \rangle_c = \langle |W_f - W_b| \rangle_c$. The figures show that $\langle |W_r| \rangle_c$ is uniform in the XZ plane, and its value, approximately $0.03U_{avg}$, is similar for both ascending and descending beads. The spanwise slip here has an important effect on bead suspension since it can produce a lift force in the wall-normal direction that is similar to the lift caused by the streamwise slip.

A slip velocity can be calculated by averaging the instantaneous relative velocity in the volume surrounding the beads. The average slip velocity for all the beads in the bottom half channel is $\langle |U_f - U_b| \rangle = 0.036U_{avg}$ in the x direction, $\langle |V_f - V_b| \rangle = 0.030U_{avg}$ in the y direction, and $\langle |W_f - W_b| \rangle = 0.033U_{avg}$ in the z direction, which corresponds to particle Reynolds numbers, Re_p, of 17.8, 14.7, and 16.3 in the x, y, and z directions, respectively. If conditional averaging is carried out at specific y/h locations, a larger Re_p of 33.5 is observed at $y/h = 0.06$ that gradually reduces to 11.8 at $y/h = 0.46$. The Re_p calculated based on apparent slip velocity, $\langle U_f \rangle - \langle U_b \rangle$, across the bottom half-channel is 6.0 in the streamwise direction, 1.7 in the wall-normal direction, and 2.1 in the spanwise direction.

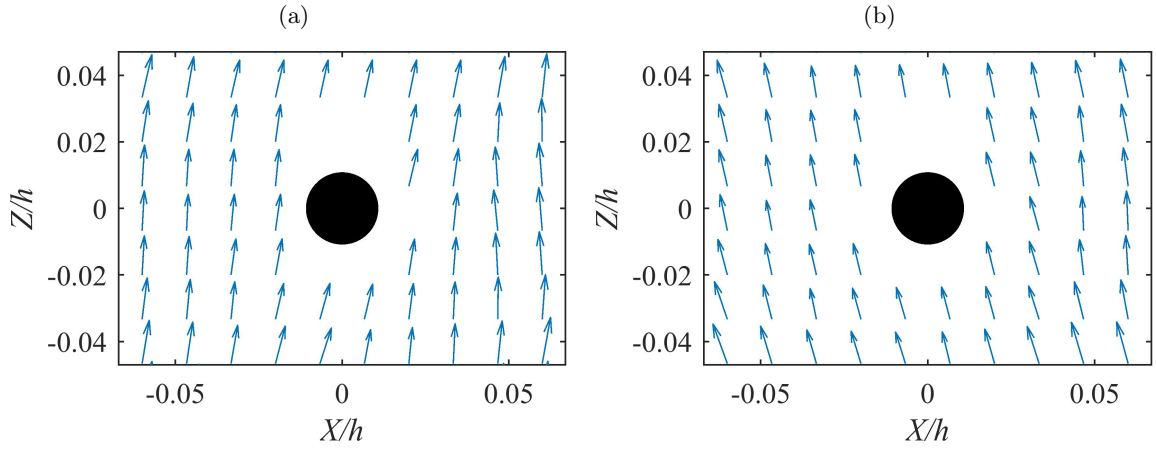

Figure 5.10: Conditional average of fluid velocity in the XZ plane relative to the (a) ascending and (b) descending beads. For the spanwise component, the absolute value of relative velocity, i.e., $\langle |W_f - W_b| \rangle_c$, is used. The vectors are scaled similar to Figure 5.9.

Therefore, use of the apparent slip velocity to calculate Re_p produces a value that is lower by a factor of one-half to one-third. This is an important result since Re_p is a key parameter in determining turbulence modulation in particle-laden flows.

5.5 Accelerating/decelerating beads

Acceleration or deceleration of a bead indicates momentum exchange with the fluid phase through different forces. For finite-size particles, these forces include drag force, added mass, and Basset history force. In this section, the flow pattern surrounding the beads is conditionally averaged based on whether a bead is subject to acceleration or deceleration in the streamwise direction. The conditional averages show the pattern of relative fluid velocity around the bead, and therefore they indicate the direction of the drag force. Such an analysis can be helpful for numerical simulations since in most cases only the drag force is considered. The instantaneous streamwise acceleration of a bead is referred to as a_b, which is obtained from the Lagrangian trajectories obtained using 3D-PTV.

5.5.1 Conditionally averaged velocity

The streamwise, wall-normal, and spanwise bead velocity and the surrounding fluid velocity are conditionally averaged based on the sign of a_b and are shown in Figure 5.11. The mean fluid velocity (ensemble average) is also shown in Figure 5.11a for comparison. In Figure 5.11a, $\langle U_b \rangle_c$ of accelerating beads is lower than the surrounding fluid velocity. Hence, on average, there is a positive slip velocity, which generates a force to accelerate the beads. The streamwise slip velocity increases slightly with decreasing distance from the wall. In Figure 5.11b, the accelerating beads are shown to have a positive $\langle U_b \rangle_c$, which indicates that they ascend toward the center of the channel as they accelerate.

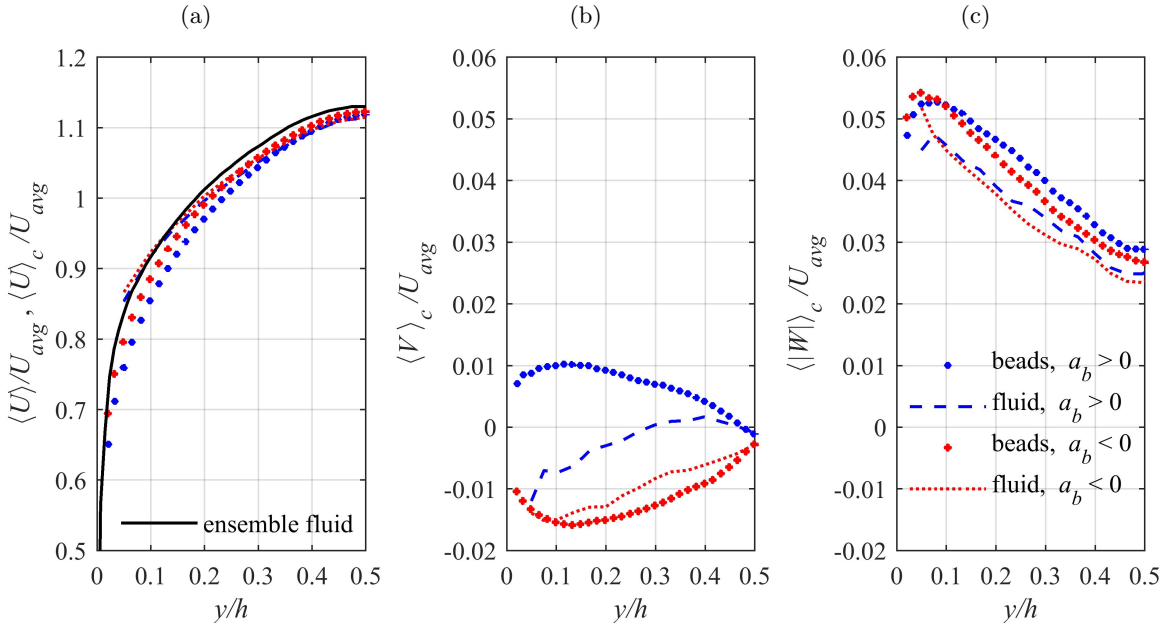

Figure 5.11: Conditional average of (a) streamwise, (b) wall-normal, and (c) absolute spanwise velocity of the beads and their surrounding fluid sampled based on the sign of a_b.

The decelerating beads at $y/h > 0.25$ ($y^+ > 250$) of Figure 5.11a have a slightly higher velocity than the surrounding fluid. The beads also have a negative $\langle V \rangle_c$ (Figure 5.11b), which shows that they move toward the wall and into the lower-velocity layers, and the resulting drag force decelerates the beads. However, at $y/h < 0.25$, decelerating beads are slower than the surrounding fluid, i.e., $\langle U_b \rangle_c - \langle U_f \rangle_c < 0$, while they still have a negative

$\langle V \rangle_c$. To further evaluate this observation, the average of instantaneous slip, $\langle U_f - U_b \rangle$, was also calculated. It was found to be positive and equal to $0.01U_{avg}$. A positive slip velocity means that deceleration of the beads is not associated with the drag force. Therefore, at $y/h < 0.25$, other forces such as added mass, Basset force, or friction due to collision and momentum exchange with the wall contribute to bead deceleration.

Values of $\langle |W| \rangle_c$ for accelerating and decelerating beads, and the surrounding fluid, are shown in Figure 5.11c. The beads have a higher spanwise velocity than the surrounding fluid, which is similar to the trend in the wall-normal direction. Again, as was the case for the wall-normal motions, it is hypothesized that the beads preserve their spanwise velocity for a greater duration than the fluid phase, which results in a higher average bead velocity. The spanwise velocity profiles are almost identical to the velocity profiles shown for ascending and descending beads in Figure 5.3c; the effect of sampling criterion on spanwise velocities is negligible.

5.5.2 Velocity fields around the beads

To relate the 3D flow field with the bead dynamics, the relative velocity fields, $\langle \boldsymbol{U}_r \rangle_c = \langle \boldsymbol{U}_f - \boldsymbol{U}_b \rangle_c$, around accelerating ($a_b > 0$) and decelerating beads ($a_b < 0$) are illustrated in Figure 5.12 for the XY plane and in Figure 5.13 for the XZ plane. The conditional averaging is carried out across the bottom half-channel. It was shown in Figure 5.11a that accelerating beads are slower than their surrounding fluid across the bottom half-channel, and as a result the drag force contributes to their streamwise acceleration. However, the relative velocity is not uniform around the bead. In Figure 5.12a, a net positive streamwise $\langle U_r \rangle_c$ is seen above the bead at $Y > 0$ and a negative relative velocity is present below the bead at $Y < 0$. The relative velocity field is uniform and has a positive value in the whole XZ plane, as shown in Figure 5.13a. Comparing Figures 5.9 and 5.12, we see that the relative velocity fields around accelerating and decelerating beads have a structure that is similar to the flow pattern around ascending and descending beads in the XY plane, but with a lower wall-normal velocity. The velocity field around decelerating beads, shown in

Figure 5.12b, has a positive relative velocity at $Y > 0$ and a negative relative velocity at $Y < 0$. The averaged relative velocity in this plane is negative. Despite the presence of accelerating beads, no uniform trend is observed in the XZ plane of Figure 5.13b.

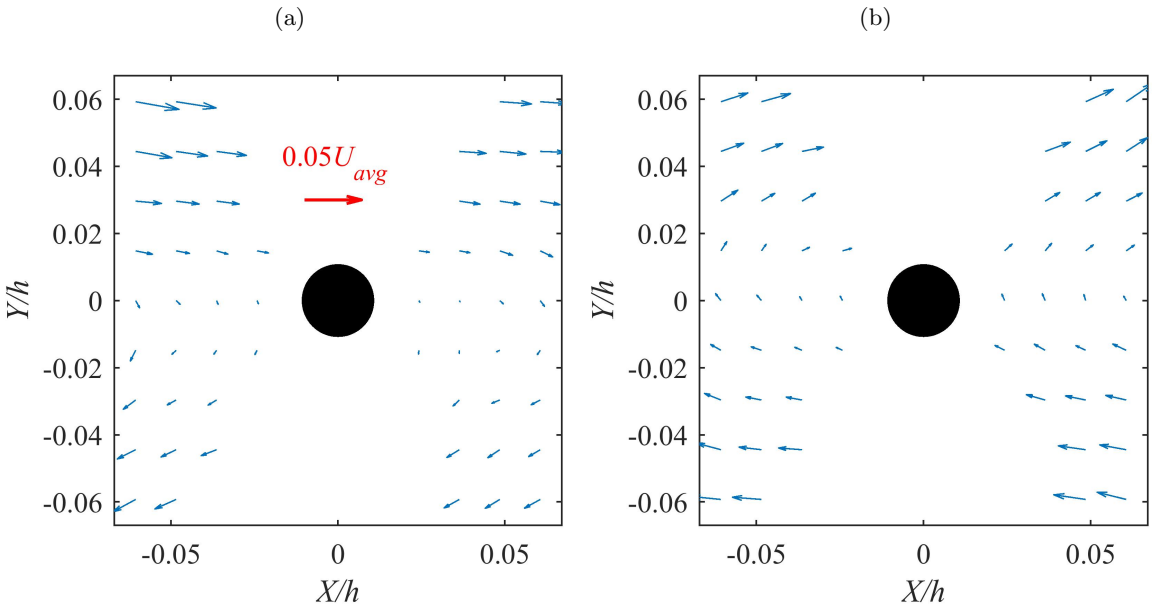

Figure 5.12: Conditional average of relative fluid velocity, $\langle \boldsymbol{U}_r \rangle_c = \langle \boldsymbol{U}_f - \boldsymbol{U}_b \rangle_c$, in the XY plane surrounding (a) accelerating ($a_b > 0$) and (b) decelerating beads ($a_b < 0$). The red arrow shows the reference vector size.

5.6 Bead pathlines

The previous sections showed that bead motion is accompanied by a significant spanwise velocity component, which is higher closer to the wall. To understand the phenomenon that produces this spanwise motion, bead pathlines are examined here. Figure 5.14 shows four sample pathlines and their projection on the xy, yz, and xz planes, within the field of view of the 3D-PTV setup. The selected pathlines are representative of different pathline patterns observed by visual inspection, and they are numbered in the yz plane of Figure 5.14. Pathlines (1) and (2) do not show frequent change in their wall-normal and spanwise motions; pathline (1) is inclined 4° toward the wall, and pathline (2) has an angle of 5° away from the wall. These pathlines are usually located in the outer layer, closer to the channel

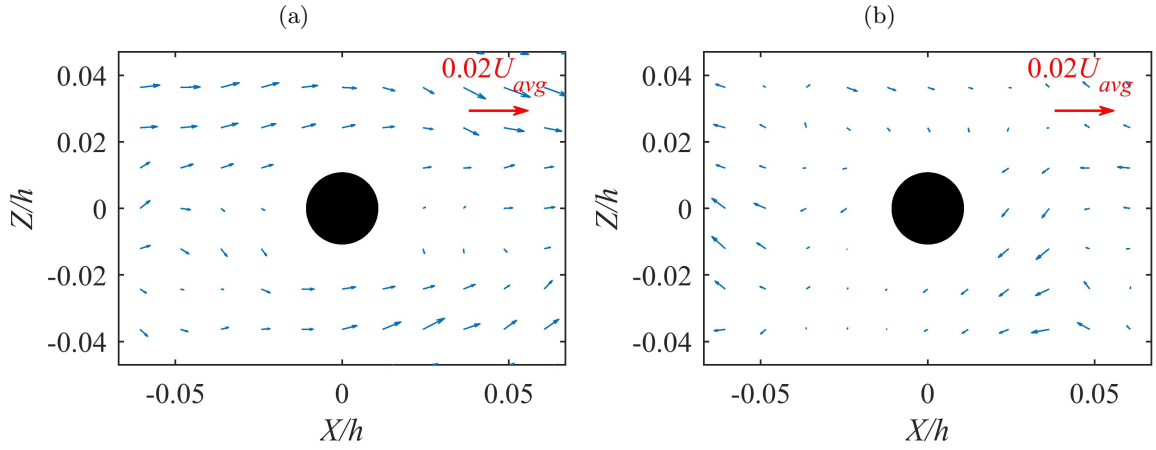

Figure 5.13: Conditional average of relative velocity field, $\langle \boldsymbol{U}_r \rangle_c = \langle \boldsymbol{U}_f - \boldsymbol{U}_b \rangle_c$, in the XZ plane surrounding (a) accelerating beads ($a_b > 0$) and (b) decelerating beads ($a_b < 0$). The red arrow shows the reference vector size.

center. Pathlines (3) and (4), on the other hand, show frequent changes in the direction of their wall-normal and spanwise motions, which result in a spiral motion around the x axis. The beads shown by pathlines (3) and (4) move forward by a distance of $x/h \sim 3.5$ as they undergo two full spins around a streamwise axis.

The frequent change in the bead wall-normal motion was also observed in the experimental studies of Sumer and Oguz [1978] and Rashidi et al. [1990], but the bead spanwise motion was not revealed by their 2D measurements. Pathlines (3) and (4) spiral in the yz plane and result in the observed spanwise bead velocity. The spiral motion of the beads and the change in their direction of motion are more apparent closer to the wall since the flow time scale is smaller and the spiral motions are captured within the measurement domain. Pathlines (1) and (2) are associated with motions having a longer time scale since they are farther away from the wall. It should also be noted that the axes in Figure 5.14 do not have the same scale, and the displacements are magnified in the y and z directions.

Inspection of the pathlines shows that the majority of descending beads approach the wall and change direction when they reach $y/h \sim 0.05$ ($y^+ = 50$). To characterize this change in direction statistically, the local maxima (y_{max}) and minima (y_{min}) in the y position are detected using the slope (dy/dt) of the trajectories. An example is indicated by points

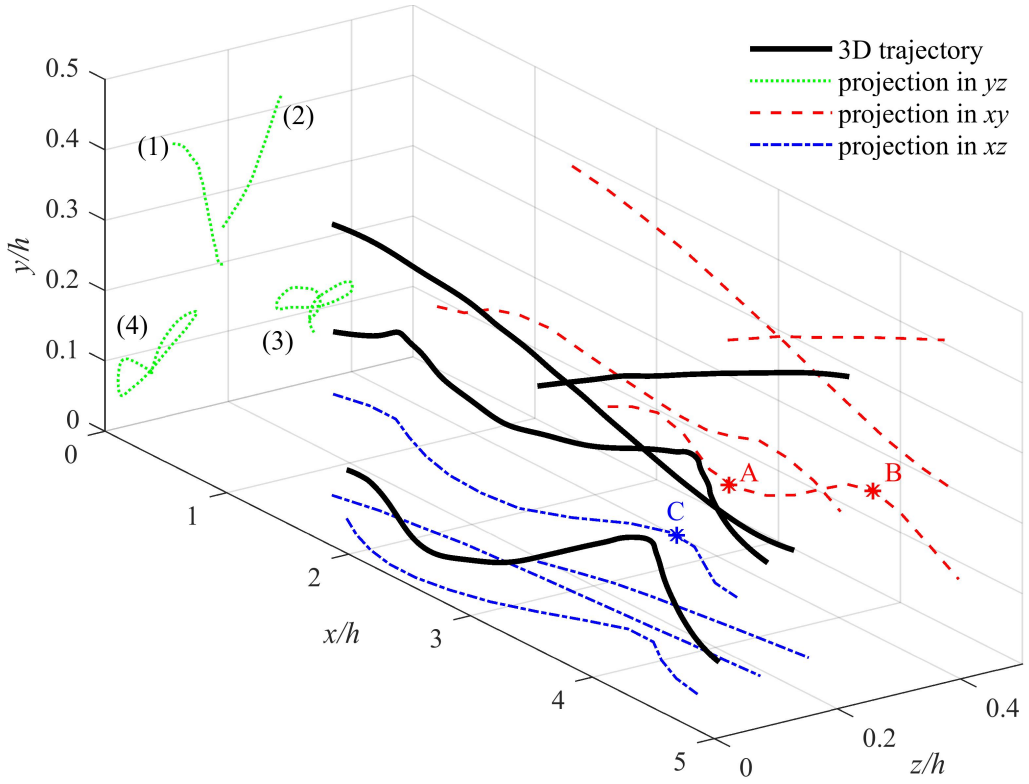

Figure 5.14: Sample 3D trajectories of beads (shown in black) and their projection on xy, yz, and xz planes. The spiral of the pathlines (3) and (4) about the x direction can be recognized as they move forward. For better representation, y and z axes are magnified by a factor of 3.5 with respect to the x axis.

A and B in Figure 5.14. The same analysis is also conducted to detect the points where the beads' spanwise motion changes direction; that is, extrema in the z direction indicated at z_{ext}, like point C in Figure 5.14. The probability density function (PDF) of the number of detected y_{min}, y_{max}, and z_{ext} is presented in Figure 5.15. It is observed that the PDF of y_{min} is larger close to the wall, confirming that most of the descending paths change direction in this region. In contrast, the PDF of y_{max} increases with distance from the wall; that is, with increasing distance from the wall, a greater number of ascending motions change direction and approach the wall. The change in the direction of motion from descending to ascending is hypothesized to result from ejection motions of the fluid, or collision of the beads with the wall. Because the ejections are stronger near the wall, the changes in the descending motions occur more frequently in this region. On the other hand, the upward-moving beads

usually change direction because of gravitational and drag forces, as highlighted in Figure 5.9a. This results in the gradual PDF increase for y_{max} with an increase of y. Figure 5.15a also shows that the number of spanwise extrema reduces with decreasing y, which is associated with stronger spiral motions in the near-wall region.

To identify the effect of particle concentration and potential particle-particle collisions, the number density profile of the beads is shown in Figure 5.15b. In this figure, the number of beads in each bin (y_{bin} = 0.4 mm) is normalized by the average number of beads per bin (N_{avg}). It can be seen that the distribution is almost uniform; the maximum number density is only 17% larger than the minimum number density ($N_{max}/N_{min} = 1.17$). Hence, variation in the number density of particles is small and is not expected to be associated with an increased probability of particle-particle collisions.

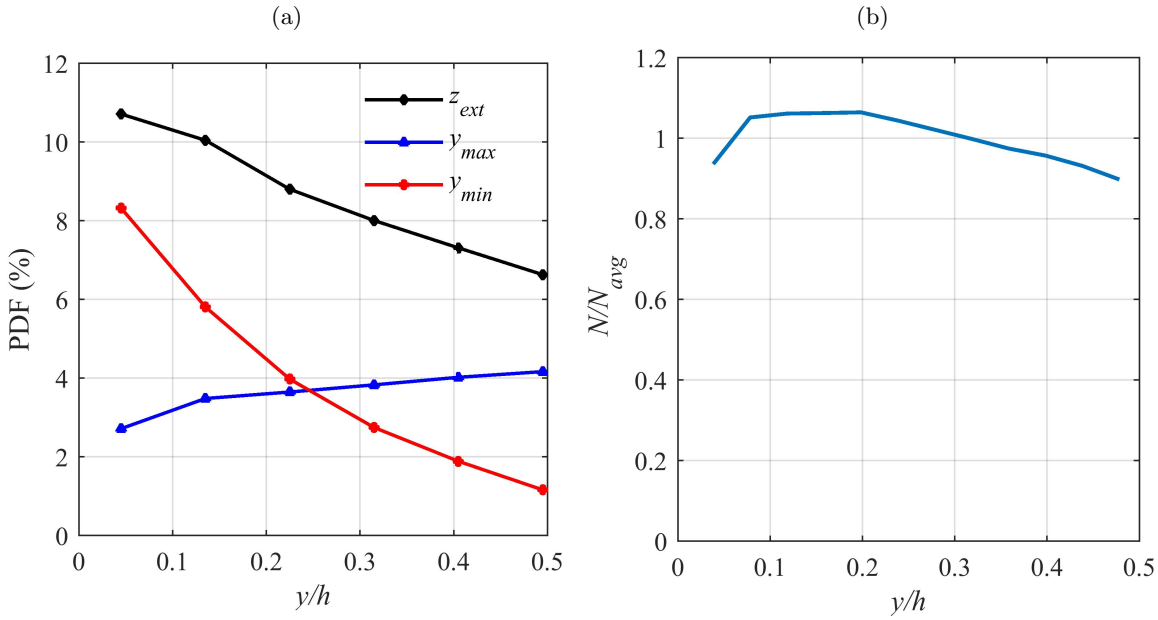

Figure 5.15: (a) The PDF of the number of local maxima (y_{max}) and minima (y_{min}) in the wall-normal position of the beads, and the number of local extrema in the spanwise position of the beads (z_{ext}). (b) Normalized number density profile of the beads across the bottom-half channel.

5.7 Uncertainty analysis

The random errors in the velocity statistics for the beads and the fluid phase are evaluated here based on the statistical convergence of the data at $y^+ = 30$, 250, and 500 (which corresponds to $y/h = 0.03$, 0.23, and 0.46). Figure 5.16 shows the statistical convergence of the velocity statistics of the beads at $y^+ = 500$. The horizontal axis of the figure shows the number of data points used for averaging (n) normalized by the total number of data in the bin (N). The random error is estimated as the difference between the maximum and minimum of the averaged quantity using the last 20% of the data points. The results are presented in Table 5.1 for the beads and in Table 5.2 for the fluid phase.

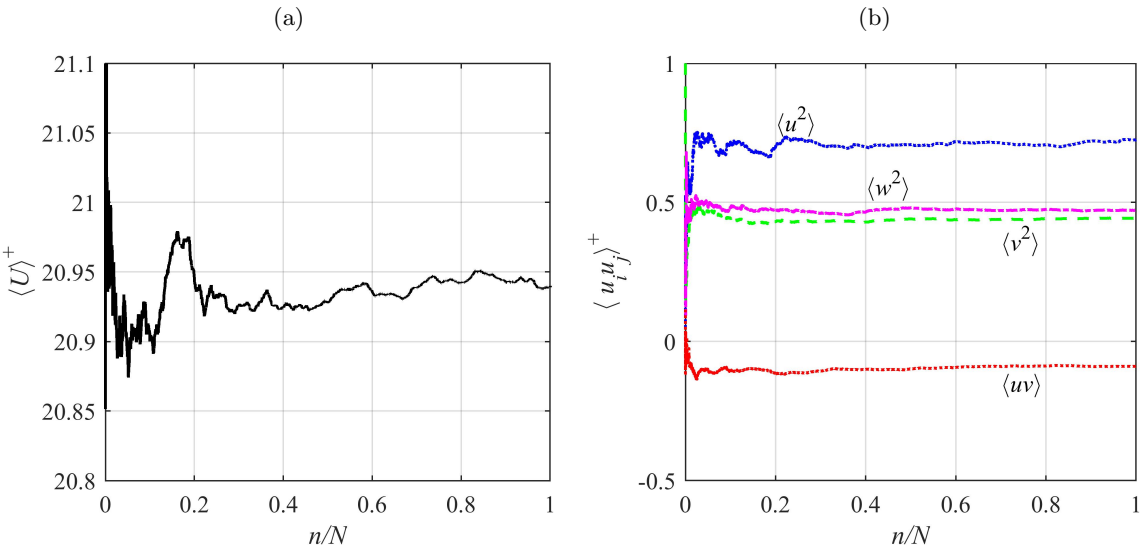

Figure 5.16: Statistical convergence of (a) the mean velocity and (b) Reynold stresses of the beads at $y^+ = 500$ ($y/h = 0.46$). The maximum and minimum values for n/N of 0.8 to 1 are used to estimate the random error.

5.8 Conclusion

The interaction between the beads and the fluid phase was investigated in a particle-laden turbulent channel flow at $Re = 20{,}000$. The particulate phase consisted of nearly neutrally buoyant beads with $d_b = 370$ µm and $St^+ = 40.0$ at a volumetric concentration of

Table 5.1: Estimated random error for the beads' statistics.

Parameter	$y^+ = 30$	$y^+ = 250$	$y^+ = 500$
$\langle U_b \rangle^+$	0.025	0.011	0.013
$\langle u_b^2 \rangle^+$	0.030	0.040	0.020
$\langle v_b^2 \rangle^+$	0.006	0.006	0.003
$\langle w_b^2 \rangle^+$	0.011	0.010	0.006
$\langle u_b v_b \rangle^+$	0.010	0.006	0.004

Table 5.2: Estimated random error for velocity statistics of the fluid phase.

Parameter	$y^+ = 30$	$y^+ = 250$	$y^+ = 500$
$\langle U_f \rangle^+$	0.021	0.012	0.007
$\langle u_f^2 \rangle^+$	0.090	0.020	0.009
$\langle v_f^2 \rangle^+$	0.020	0.003	0.004
$\langle w_f^2 \rangle^+$	0.030	0.006	0.004
$\langle u_f v_f \rangle^+$	0.020	0.005	0.007

0.1%. Three-dimensional time-resolved particle tracking velocimetry (3D-PTV), based on the shake-the-box method, was used to measure the instantaneous velocities of the beads and the fluid phase simultaneously. The beads' velocity and the surrounding flow were conditionally sampled based on the wall-normal velocity (ascending versus descending beads) and the streamwise acceleration of the beads (accelerating versus decelerating beads).

The conditional averaging, based on the wall-normal velocity, showed that the streamwise velocity of the ascending beads and the surrounding fluid is lower than the ensemble fluid velocity. This velocity deficit is associated with the preferential accumulation of the ascending beads in the low-speed regions. In contrast, the descending beads and their surrounding fluid had nearly the same average velocity as the ensemble fluid. The apparent slip velocity, based on the difference of the average bead and flow velocity, was higher for the ascending beads. It was also observed that the spanwise bead velocity was higher than the wall-normal bead velocity. At $y/h < 0.25$ ($y^+ < 250$), the streamwise velocity of descending beads showed a strong correlation with the nearby fluid. However, this correlation decreased

with increasing wall-normal distance since the preferential accumulation of descending beads in sweep motions decreased. The descending beads also had a stronger correlation with the wall-normal flow velocity. For the ascending beads, with increasing wall-normal distance, both their correlation with surrounding flow and the extent of accumulation in ejection motions increased.

The conditional sampling based on bead acceleration showed that accelerating beads move away from the wall and have a lower velocity than the surrounding flow. Away from the wall, at $y/h > 0.25$, the decelerating beads also have a higher streamwise velocity than the surrounding fluid. Therefore, for both cases, the drag force caused by slip velocity contributes to their acceleration/deceleration. However, at $y/h < 0.25$, decelerating beads have a lower velocity than the surrounding flow, suggesting that the drag force alone is not sufficient to model the dynamics of nearly buoyant beads.

The simultaneous measurements of bead and carrier phase velocities showed that the slip velocity calculated from the difference between the average bead and fluid velocities, $\langle U_f \rangle_c - \langle U_b \rangle_c$, significantly underestimates the actual instantaneous slip velocity. The conditionally averaged flow fields also showed a remarkable spanwise slip velocity. The flow velocity pattern with respect to an enclosed bead appeared as a clockwise vortex in the XY plane, with a significant wall-normal velocity gradient. The conditionally averaged wall-normal velocity of the fluid appeared to oppose the motion of ascending and descending beads. This observation supported the notion that the motion of a bead begins with fluid ejection that quickly decays, while the bead sustains its motion for a longer time.

The beads' pathlines showed successive upward and downward motions, and also successive changes in the direction of spanwise motion. The latter resulted in a spiral motion around the x direction with a shorter turnover time in the near-wall region ($y/h < 0.25$). The descending beads frequently changed direction in the near-wall region when approaching the wall, while ascending beads frequently changed direction farther away from the wall.

Chapter 6

Distribution of Inertial Particles in Horizontal Channel

Distribution of the glass beads in the near-wall region of a horizontal turbulent channel flow is studied in this chapter. Glass beads with a diameter of 210 µm are used to make suspensions at bulk volumetric concentrations (ϕ_v) of 0.05% to 0.27%. The measurements are performed at Reynolds number (Re) of 20,000, 40,000, and 60,000. The measurement technique explained in Section 3.4 is used to measure the Lagrangian velocity and determine the position of the particles.

6.1 Introduction

Turbulent flows laden with solid particles frequently occur in slurry pipelines, fluidized beds, and pneumatic conveying systems. In these systems, the particles are transported through several mechanisms including gravitational settling, dispersion by turbulence, turbophoresis [Caporaloni et al., 1975], inter-particle collisions [Abrahamson, 1975], and shear-induced lift [Saffman, 1965, Auton, 1987]. These mechanisms may oppose each other and their strength varies with several conditions including fluid velocity and turbulence, particulate size and density, and bulk particle concentration [Kussin and Sommerfeld, 2002, Picano et al., 2015, Capecelatro and Desjardins, 2015, Capecelatro et al., 2018, Zade et al., 2018]. As a result, the particles may not uniformly disperse in the carrier phase. This is specifically important in the near-wall region since the local particle concentration directly affects the wear-rate

of the surface material [Roco and Addie, 1987].

In a horizontal flow, the gravity tends to settle down the particles and increase their concentration close to the lower wall. On the other hand, the carrier-phase turbulence suspends the particles and disperses them in the flow. A few investigations modeled the particle dispersion by turbulence as a diffusion mechanism [Karabelas, 1977, Nasr-El-Din et al., 1987, Gillies and Shook, 1994]. In these models, the wall-normal flux of particles is equal to a particle diffusivity coefficient, ε_b, times the wall-normal gradient of particle concentration. Similar to the eddy diffusivity, since the characteristic length-scale of the turbulent dispersion is comparable with the size of the particles, ε_b needs to be empirically determined for each flow condition. Assuming that only gravity and turbulence diffusion dominate particle transport, the profile of particle concentration has been approximated by a power-law distribution in horizontal flows [Chien and Wan, 1999, Kiger and Pan, 2002]. In this case, the concentration reduces with increasing wall-normal distance, and it mainly depends on the Rouse number, $V_s/\kappa u_\tau$ where V_s is the terminal settling velocity of the particles, κ is the von Kármán constant, and u_τ is the friction velocity [Sumer and Oguz, 1978, Marchioli et al., 2008]. However, on the contrary, a few experiments and simulations have shown that the particle concentration can increase with increasing wall-normal distance [Nasr-El-Din et al., 1987, Capecelatro and Desjardins, 2015, Fornari et al., 2016]. Such a trend has been associated with large Re and bulk volumetric concentration (ϕ_v), and cannot be predicted by the diffusion-based model. The deviation has been associated with other mechanisms such as turbophoresis, shear-induced lift, particle-wall lubrication, and inter-particle collisions.

The turbophoresis mechanism refers to the migration of particles toward regions with lesser turbulence intensity [Caporaloni et al., 1975, Reeks, 1983, Marchioli and Soldati, 2002]. Since the particle transport in the wall-normal direction is studied, turbophoresis is assumed to be proportional to the wall-normal gradient of wall-normal Reynolds stress, $d\langle v_b^2\rangle/dy$. Here, v_b is the wall-normal velocity fluctuation of the beads and $\langle\rangle$ refers to the ensemble averaging. The strength of turbophoretic drift also changes with the Stokes

number which is defined as the ratio of the particle relaxation time to the time scale of the flow. The turbophoresis effect is most significant when the time scales of flow and particles are comparable [Sardina et al., 2012, Lillo et al., 2016]. Turbophoresis typically causes accumulation of particles in the near-wall region because of the steep gradient of $\langle v_b^2 \rangle$ [Caporaloni et al., 1975]. This type of concentration profile is usually referred to as a wall-peaking profile.

An increase of particle concentration toward the channel centerline has been observed in numerical simulations [Li et al., 2001, Marchioli et al., 2007, Capecelatro and Desjardins, 2015, Fornari et al., 2016] and experimental investigations [Shokri et al., 2017]. The DNS of Fornari et al. [2016] demonstrated a concentration peak at the center of a channel at volumetric concentration of 5.0%, and normalized bead diameter of $d_b^+ = 10$ with $St_K = 8.8$. The peak that forms about the channel centerline is usually referred to as core-peak. Here, d_b^+ is bead diameter normalized by the inner scaling. They attributed the core-peaking to the beads migration toward the conduit core due to the shear-induced lift force.

The shear-induced lift is proportional to the volume of particle, slip velocity between the solid and the liquid phase, and velocity gradient [Auton, 1987]. In a vertical solid-liquid flow, Shokri et al. (2017) experimentally observed core-peaking only for the largest investigated beads with $d_b^+ = 540$ and $St_K = 14.0$. They also conjectured that this particle migration is due to shear-induced lift. Marchioli et al. [2007] also observed this trend in their numerical simulation. The negative slip velocity in their upward flow created a lift force which shifted concentration peak toward the center of channel.

In addition to the aforementioned transport mechanisms, inter-particle collisions can also contribute to particle transport and affect the mean concentration profile. Different statements are given on whether particle collisions contributed to core-peaking or wall-peaking. Kussin and Sommerfeld [2002] stated that in a horizontal gas-solid flow, inter-particle collisions can result in the ejection of particles from a high concentration near-wall region to the outer flow. The particles approaching the concentrated near-wall region may also collide with the particles and rebound toward the central region. Therefore, the inter-

particles collisions were believed to promote core-peaking.

On the other hand, Picano et al. [2015] stated inter-particle collisions make it difficult for a particle to move away from the concentrated near-wall region, and therefore it contributes to formation of a wall-peaking profile. The lubrication effect is critical in solid-liquid flows. This force acts as a repulsive force when a particle approaches the wall or another particle, and as an attractive force when they move away from each other. This makes the lubrication force as a cohesion that tends to stabilize the motion of particles. It is believed that a combination of lubrication effect and inter-particle collision traps the particles in near-wall region of solid-liquid flows [Baker and Coletti, 2019].

In this study, the local concentration and velocity statistics of glass beads are investigated in the near-wall region of a horizontal liquid channel flow. For this purpose, time-resolved three-dimensional particle tracking velocimetry (3D-PTV) based on the shake-the-box algorithm [Schanz et al., 2016] is applied. The experiments included suspensions at bulk volumetric concentrations of 0.05, 0.12, and 0.27%, and at Re of 20,000, 40,000, and 60,000. This range of flow conditions results in both wall-peaking and core peaking concentration profiles, and allows to evaluate the contribution of particle transport mechanisms.

6.2 Flow conditions

Spherical glass beads with nominal diameter, d_b, of 210 µm and a narrow distribution with a standard deviation of about 20 µm were used as the particulate phase. The beads had a density, ρ_b, of 2.6 g/cm^3. Nine sets of experiments were conducted at bulk volumetric concentrations, ϕ_v, of 0.05%, 0.12%, and 0.27%, each at three Re of 20,000, 40,000, and 60,000. The Re is calculated based on the channel height (h) and average velocity (U_{avg}) across the test section. Due to the blockage of the imaging system and the laser sheet of the 3D measurements, it was not feasible to increase the concentration beyond 0.27%. Assuming a uniform dispersion, for ϕ_v = 0.05%, 0.12%, and 0.27%, the ratio of the mean distance between the beads to d_b were 12.0, 9.2, and 6.4, respectively.

A set of experiments were also performed in unladen flow to characterize the turbulence

Table 6.1: The unladen flow conditions obtained from 3D-PTV.

Re	Re_τ	u_τ (m/s)	λ (µm)	τ_f (ms)	τ_K (ms)
20,000	525	0.056	14.3	0.25	7.4
40,000	985	0.105	7.6	0.07	2.6
50,000	1,435	0.153	5.2	0.03	1.4

in the channel. In these experiments, the liquid flow was seeded with 2 µm silver-coated glass beads (SG02S40, Potters Industries) with a density of 4 gr/cm^3. The tracers were smaller than the wall unit for all investigated Re and had a response time of 1.0 µs. Their St was 4.4×10^{-3} at $Re = 20{,}000$ and increased to 0.036 at $Re = 60{,}000$. The St is calculated using the inner time scale of the turbulent flow, as will be discussed in the following paragraphs.

The results presented in this chapter are normalized using inner scales of the unladen turbulent channel flow, which are estimated from the mean velocity profiles of the unladen flow using the Clauser method [Clauser, 1956]. The estimated friction velocity, u_τ, and inner length scale, λ, are presented in Table 1 for different Re. In this table and the rest of the manuscript, Re_τ is calculated based on the friction velocity and half-channel height ($h/2$). The quantities normalized using inner scaling of the unladen flow are indicted by superscript '+' in the following sections.

The beads relaxation time (τ_b) and the characteristic time scale of the flow (τ_f) are also estimated to calculate the Stokes number, $St = \tau_b/\tau_f$. The beads relaxation time is calculated using Eqs. 2.29 and 2.20. Here, $f_d = 1.64$ which gives $\tau_b = 5.0$ ms. In these equations, the dynamic viscosity of the water is considered 7.7×10^{-4} kg/m.s at 30 °C. The time scale of the flow can be estimated using the inner time-scale $\tau_f = \nu/u_\tau^2$, where ν is the kinematic viscosity of the fluid. The flow time-scale for different Re is provided in Table 6.1. The time-scale of flow increases toward the channel centerline, and this estimation of τ_f only applies to the near-wall region. Table 6.1 also provides the Kolmogorov time scale of the flow (τ_K) at the channel centerline that is calculated using the relations introduced by Milojević [1990].

Using the unladen flow conditions provided in Table 6.1, the dimensionless numbers of

Table 6.2: The dimensionless numbers of the particle-laden flow.

Re	d_b^+	St^+	St_K	P
20,000	14.6	20.16	0.68	1.30
40,000	27.6	72.00	1.93	0.69
50,000	40.3	168.00	3.60	0.47

the particle-laden flow including $d_b^+ = d_b/\lambda$, $St^+ = \tau_b/\tau_f$, $St_K = \tau_b/\tau_K$, and Rouse number $P = V_s/\kappa u_\tau$ are presented in Table 6.2.

6.3 Evaluation of the unladen flow

To obtain the inner scaling of the turbulent flow, the unladen velocity profile is analyzed. The uncertainty of the 3D-PTV is also investigated by comparing the statistics of the unladen flow of water at $Re = 20{,}000$ ($Re_\tau = 525$) with the DNS of Lee and Moser [2015] at Re_τ of 543 and 1000. The semi-logarithmic mean velocity profiles are presented in Figure 6.1a. The 3D-PTV results deviate from the law of the wall in the viscous sublayer ($y^+ < 5$ at $Re = 20{,}000$, $y^+ < 7$ at $Re = 40{,}000$, and $y^+ < 12$ at $Re = 60{,}000$). The discrepancy is associated with larger errors in the disparity map of the self-calibration process; the near-wall region has larger disparity error compared with layers at a farther distance from the wall. The deviation from the DNS decreases with increasing y^+ and becomes smaller than 2.5% at $y/h > 0.005$ ($y^+ > 5$ at $Re = 20{,}000$, $y^+ > 9$ at $Re = 40{,}000$, and $y^+ > 14$ at $Re = 60{,}000$). This deviation is equivalent to 0.03 pixel in estimating the particle displacement between two consecutive image frames. The mean velocity profile agrees well with the logarithmic law of the wall, $\langle U_f \rangle^+ = 1/\kappa ln(y^+) + B$, with the von Kármán constant κ of 0.38 and $B = 4.6$. This agreement confirms the accuracy of the 3D-PTV and the fully developed state of the turbulent channel flow.

The 3D-PTV measurement of the non-zero components of the Reynolds stress tensor for the unladen flow are compared with DNS of Lee and Moser [2015] in Figure 6.1b. For $y^+ > 3$ at $Re = 20{,}000$, the maximum difference between 3D-PTV and DNS is about 0.03, 0.02,

and 0.02 pixels for $\langle u_f^2 \rangle$, $\langle v_f^2 \rangle$, and $\langle w_f^2 \rangle$, respectively. Because of the smaller displacement of the beads and tracers in the wall-normal direction, this uncertainty translates into a larger relative error for $\langle v_f^2 \rangle$, which is 12.2% at $y^+ = 26$. In general, the unladen flow measurements of the 3D-PTV agrees with the DNS at $y/h > 0.005$ with maximum uncertainty of $0.15u_\tau$ (0.03 pixel) for mean velocity and Reynolds stresses. This analysis is also performed for $Re = 40{,}000$, and the $y/h > 0.005$ range is also valid for this Re. Our investigations shows that the $y/h > 0.005$ range also applies to other Re number and corresponds $y^+ > 15$ at $Re = 60{,}000$. This evaluation of uncertainty also applies to the 3D-PTV measurement in the particle-laden flow since the image of the beads and the tracers both form a Gaussian intensity profile with approximately 3 pixel diameter.

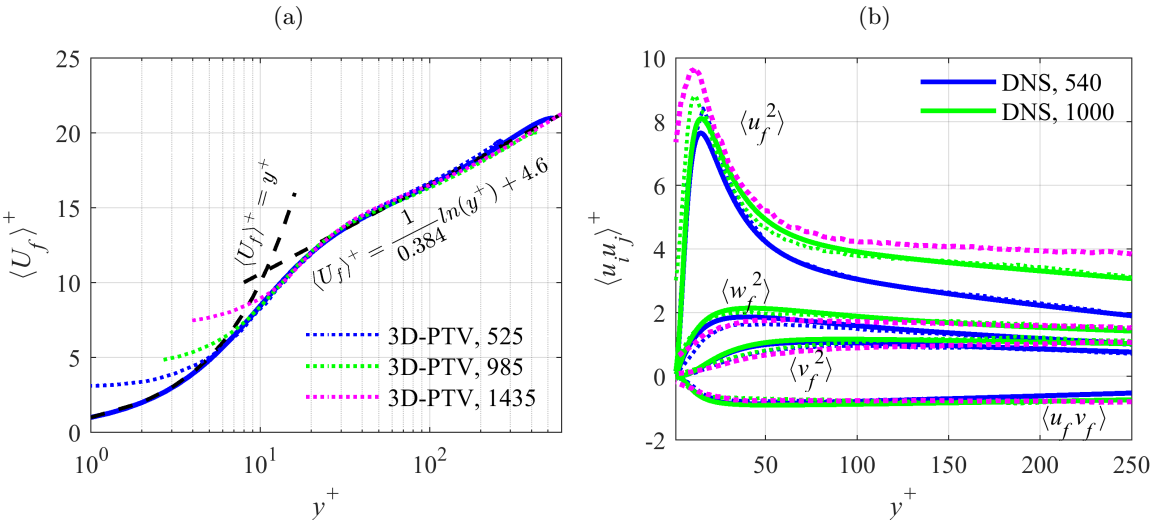

Figure 6.1: Profiles of the normalized (a) mean streamwise velocity, and (b) Reynolds stresses for the unladen flow at $Re_\tau = 525$. The results are compared with the DNS of channel flow by Lee and Moser [2015] at Re_τ of 543 and 1000.

6.4 Local particle distribution

The effect of Re and ϕ_v on the mean concentration profile of the glass beads is investigated in Figure 6.2. The number of beads detected in each bin (N) is normalized by the average number of beads per bin (N_{avg}). Normalizing by N_{avg} makes the profiles independent of

the bin size since the average value across the domain equals unity.

Figure 6.2a presents the normalized concentration profiles at Re = 20,000. This Re has the largest Rouse number of 1.30. The stronger effect of settling than the turbulence dispersion results in the significantly larger concentration of the beads near the bottom wall. However, the beads stay fully suspended in the flow and particle bed does not form in the channel. Starting from the middle of the channel, the concentration profiles of Figure 6.2a increase monotonically toward the wall and reach a maximum at $y^+ = 12$ ($y \sim d_b$). This location of the maximum concentration corresponds to the bin with $d_b/2 < y < 3d_b/2$. The thin layer at the immediate vicinity of the wall with lower bead concentration is associated with the lubrication effect as stated by Picano et al. [2015]. The ratio of the maximum concentration to the average concentration in the measured volume is 2.6 for $\phi_v = 0.05\%$ which slightly increases to 2.75 for $\phi_v = 0.12\%$ and 2.85 for $\phi_v = 0.27\%$.

At Re = 40,000, the Rouse number reduces to 0.69, and turbulence dispersion becomes more effective than gravity. Strong dispersion of the beads due to turbulence tends to flatten the concentration profile and reduce its peak value. The maximum concentration occurs at $y^+ = 25$ ($y \sim d_b$), and the peak values are 1.38, 1.44, and 1.58 for the smallest to the largest ϕ_v, respectively. Figure 6.2b also shows that with increasing y^+ for $\phi_v = 0.05\%$, the concentration does not monotonically reduce from the wall after $y^+ > 25$. The number density profile reaches a minimum at $y^+ = 210$, and local concentration increases toward the channel centerline beyond this point. This trend vanishes at higher concentrations of 0.12% and 0.27%.

The distribution profiles at Re = 60,000 in Figure 6.2c show a similar trend as Re = 40,000. The Rouse number is 0.47 at this Re. At $\phi_v = 0.05\%$, with increasing y^+, a shallow near-wall peak forms at $y^+ = 40$ ($y \sim d_b$) followed by a flat section and then a steep increase toward the channel centerline. The distribution profiles of $\phi_v = 0.12\%$ and $\phi_v = 0.27\%$ are similar with a wall-peaking trend.

The measurements show a wall-peaking concentration profile for all the cases with ϕ_v = 0.12 and $\phi_v = 0.27\%$. However, for $\phi_v = 0.05$, such a concentration is only observed at the

lower Re. A core-peaking profile is observed for $\phi_v = 0.05$ at both Re = 40,000 and 60,000.

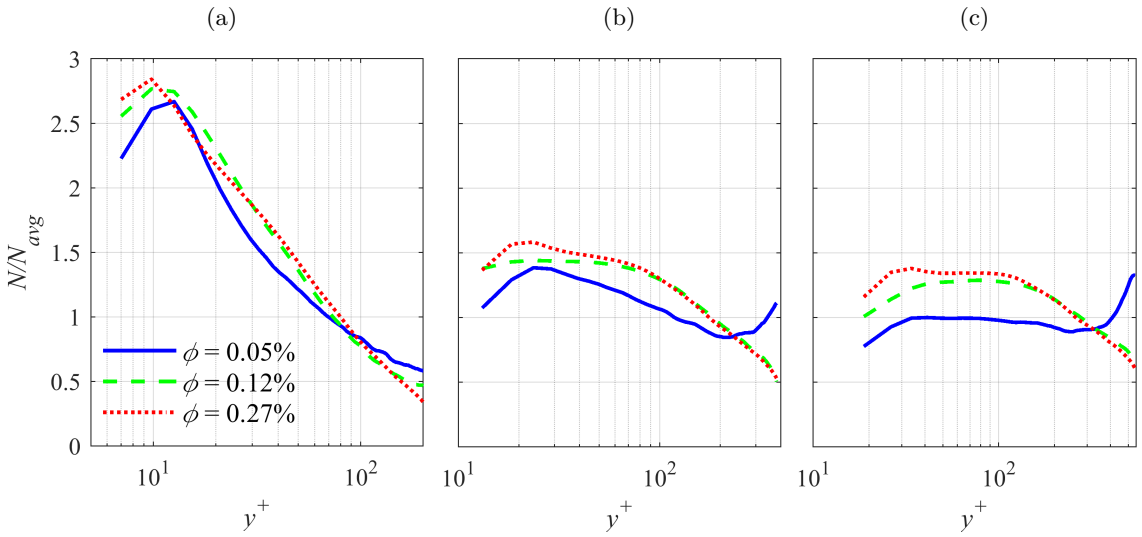

Figure 6.2: Distribution profiles of the beads at (a) Re = 20,000, (b) Re = 40,000, and (c) Re = 60,000 for $\phi_v = 0.05\%$, 0.12%, and 0.27%.

The local concentration of particles (ϕ_l) as a function of y^+ is shown in Figure 6.3. It is noteworthy that the actual concentration may be larger from the results presented here since the measurement technique was not able to track all the image particles in the domain. However, our evaluation showed that in all measurements, about 70% of the 2D particle images are tracked. Hence, the underestimation is consistent among all data set.

6.5 Mean velocity and Reynolds stresses

The mean velocity and Reynolds stresses of the beads are studied in this section. The normalized mean streamwise velocity of the beads are plotted in Figure 6.4 for Re of 20,000, 40,000, and 60,000, respectively. Each figure also presents the results for $\phi_v = 0.05\%$, 0.12%, and 0.27%. The velocity profiles of unladen flow are also shown for comparison. These figures present the mean velocity in the range of $y^+ > d_b^+/2$ which are reliable based on the uncertainty analysis performed in Section 6.3.

In the vicinity of the wall, the beads have a larger velocity than the unladen flow. This larger velocity is due to the sliding and rolling motions of the beads over the wall as they

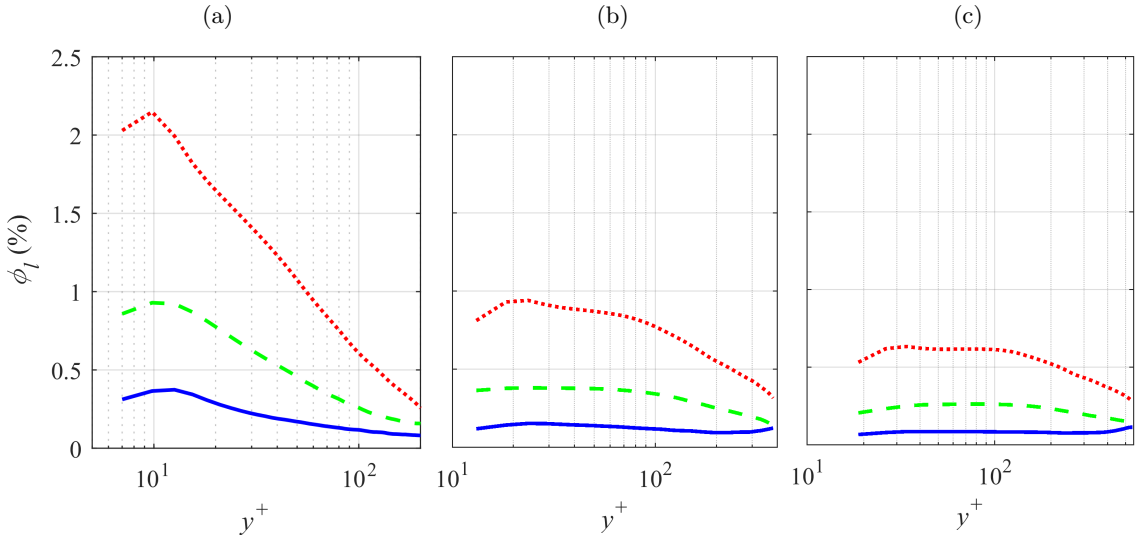

Figure 6.3: Local concentration profiles of the beads at (a) Re = 20,000, (b) Re = 40,000, and (c) Re = 60,000 for ϕ_v = 0.05%, 0.12%, and 0.27%.

do not adhere to the no-slip boundary condition. With increasing ϕ_v, a noticeable increase in the mean streamwise velocity of the beads is observed at $y^+ < 40$. This flattening of the velocity profile at higher ϕ_v can be attributed to a greater number of inter-particle collisions. Farther away from the wall, the velocity of the beads is smaller than the fluid. It is also observed that with increasing ϕ_v and Re, the point where the velocities of the beads and the unladen flow are the same, moves toward the channel centerline. In general, the beads have a smaller mean streamwise velocity than the unladen flow at $y^+ > 30$, which has been associated with the larger concentration of the inertial particles in the low-speed regions of a turbulent flow [Kiger and Pan, 2002].

The effects of Re and ϕ_v on the Reynolds stresses of the beads are presented in Figure 6.5. At all the Re, $\langle u^2 \rangle$ reduces with increasing ϕ_v. This reduction can be due to the larger number of non-elastic inter-particle collisions [Kussin and Sommerfeld, 2002]. Comparison of Figures 6.5a-c demonstrates that, with the increase of Re, $\langle u^2 \rangle^+$ reduce. The same trend was also observed in the 2D-PTV measurement of Ahmadi et al. [2019]. This observation was associated with the larger St at higher Re, which reduces the response of the beads to the turbulent fluctuations of the fluid.

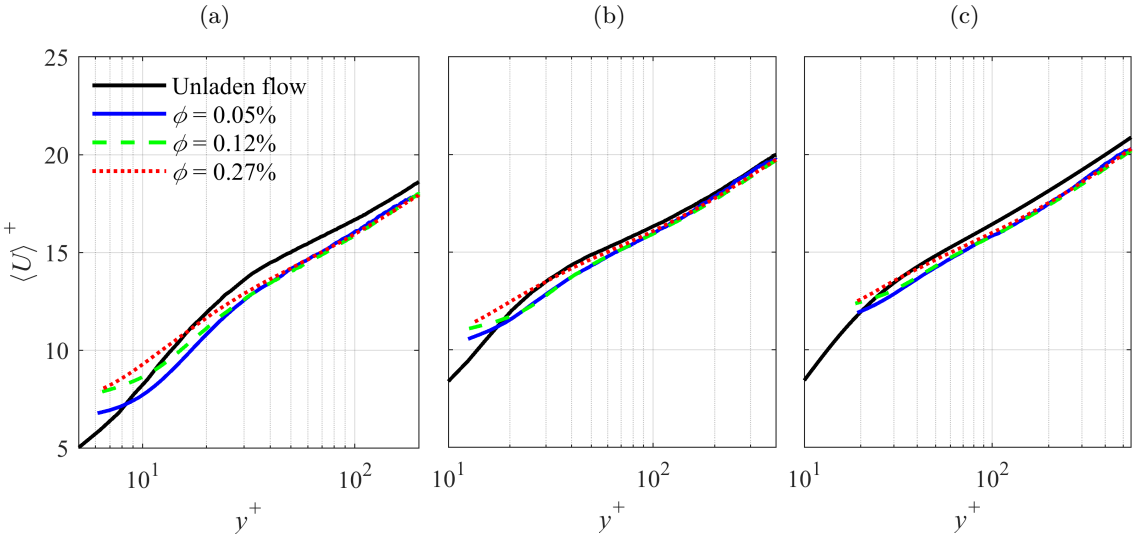

Figure 6.4: Mean streamwise velocity profile of the beads at (a) Re = 20,000, (b) Re = 40,000, and (c) Re = 60,000 at various bulk volumetric concentrations. The velocity profile of unladen flow from 3D-PTV at the same Re is also shown for comparison.

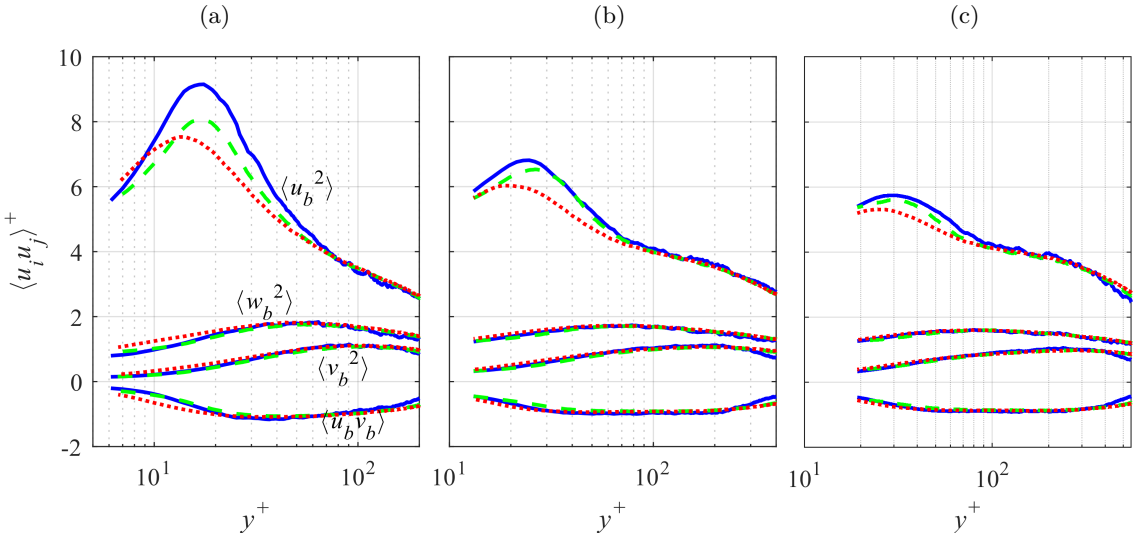

Figure 6.5: Reynolds stresses of the beads at (a) Re = 20,000, (b) Re = 40,000, and (c) Re = 60,000 at various volumetric concentrations. For legends, see Figure 6.4.

6.6 Shear-induced lift force

It is intended in this section to evaluate the shear-induced lift force, also called the Saffman lift force, and its potential effects on the distribution of the beads in turbulent channel flow.

It was observed in Figure 6.2 that at $\phi_v = 0.05\%$ and Re of 40,000 and 60,000, the number density of the beads increased toward the channel centerline at $y^+ > 200$. The role of the shear-induced lift force in this observation is investigated in this section.

A bead that moves in a shear flow experiences a lift force proportional to the slip velocity between the fluid and bead, the diameter of the bead, and the fluid velocity gradient. The shear-lift force calculated analytically by Saffman [1965] for small beads in a uniform simple shear flow and extended to larger particle Reynolds number (Re_p) by Mei and Adrian [1992]. The Re_p is defined based on the slip velocity, $U_f - U_b$. In a channel flow at moderate Re_p of about 40, the lift force is proportional to [Sommerfeld, 2003]

$$F_{SL} \sim \rho_f d_b^3 \left(\langle U_f \rangle - \langle U_b \rangle\right) \frac{d\langle U_f \rangle}{dy}. \tag{6.1}$$

The subscript SL in this equation refers to the 'shear lift' term. The term $d\langle U_f \rangle/dy$ is estimated here by the velocity gradient of the unladen flow since the fluid phase velocity is not measured in this study. Investigation of the results presented in Figure 6.4 shows that the gradient of the streamwise velocity of the beads at $y^+ > 70$ is almost equal to $d\langle U \rangle/dy$ of the unladen flow. Hence, it is quite reasonable to assume that the fluid phase in laden flow also has the same streamwise velocity gradient as unladen flow in this region. The mean velocity in this region follows the logarithmic law and the gradient term in Eq. 6.1 can be estimated as

$$\frac{d\langle U_f \rangle}{dy} = \frac{u_\tau}{\kappa y}. \tag{6.2}$$

Equation 6.2 shows that the velocity gradient term varies linearly with the friction velocity in the log-law region. Hence, the magnitude of the lift force becomes larger at larger Re which is the reason that core-peaking only occurs at Re of 40,000 and 60,000. At Re = 20,000, the gradient term is small, and the lift force is not strong enough to create a net migration of the beads toward the core region.

The beads usually have larger velocity than the fluid phase in the near-wall region, while they become slower at further distances from the wall in solid-liquid turbulent flows [Rashidi et al., 1990, Shokri et al., 2017, Ahmadi et al., 2019]. This implies that the wallward

direction of the shear-lift force in the near-wall region changes toward the channel centerline at some distances from the wall. This can create a local minimum at number density profiles as shown in Figures 6.2b and 6.2c at $y^+ \sim 200$. Intensive shear-induced migration of the beads was also observed in DNS of Fornari et al. [2016] at $\phi_v = 5.0\%$ and $Re_\tau = 180$ for density ratios of the order of 10 that led to a concentration peak at the channel centerline. This trend became weaker with the increase of the density ratio and completely disappeared at the density ratio of 1000.

It was observed in Figures 6.2b and 6.2c that the increase of local concentration toward the channel centerline at $y^+ >\sim 200$ does not happen at relatively larger concentrations of 0.12% and 0.27%. This is due to the larger number of inter-particle collisions at larger considerations and the wall-lubrication effect as discussed in the following sections. The other reason may be the weakening of the lift force at larger concentrations.

6.7 Relative velocity between the beads

The inter-particle collision frequency is proportional to the radial relative velocity between the nearby beads. The pressure build-up between the particles approaching each other, and consequently, the lubrication force also depend on the magnitude of the radial relative velocity. The collision between the beads can modify the distribution of the beads in different ways. A frequent inter-particle collision at dense suspensions reduces the mean-free path of the beads which prevents remarkable migration of the beads away from the wall. This can confine the beads in concentrated regions and increase the local concentration near the wall as observed in Figures 6.2b and 6.2c at $\phi_v = 0.12\%$ and 0.27%.

In a monodispersed system with a number density of n, the collision frequency is proportional to [Wang et al., 2000]

$$f_c \sim 2\pi d_p^2 \langle |v_r| \rangle n, \tag{6.3}$$

where n stands for the number density (particle/m^3) that was investigated in previous sections. In this equation, v_r is the radial component of the relative velocity between the beads that shows the velocity at which the beads approach each other. In order to obtain

v_r, pairs of the beads that have a smaller distance than $5.0d_b$ are detected (called beads a and b), and their relative velocity vector ($\boldsymbol{v}_r = \boldsymbol{v}_a - \boldsymbol{v}_b$) is projected on the vector connecting bead a to the bead b ($\boldsymbol{x}_r = \boldsymbol{x}_a - \boldsymbol{x}_b$). It should be noted that the threshold chosen for the distance between the beads does not affect the trends presented in this section.

A larger relative velocity between pairs of the beads intensifies the frequency of the collision [Sommerfeld, 2003]. Variation of $\langle|v_r|\rangle$ as a function of wall-normal distance at Re of 20,000, 40,000, and 40,000 are shown in Figure 6.6. Results are normalized using the inner scales of flow at Re = 20,000 ($u_{\tau,20}$, λ_{20}). The profiles reach a peak at $y/\lambda_{20} \sim 20$ and then reduce toward the channel centerline. The peak of $\langle|v_r|\rangle$ is located near the wall where the turbulent kinetic energy of the beads are maximum. The magnitude of $\langle|v_r|\rangle$ also increases with increase of Re as can be seen in the figure. These trends imply that the turbulence in the flow is the main source of relative velocity between the beads, and consequently, inter-particle collisions.

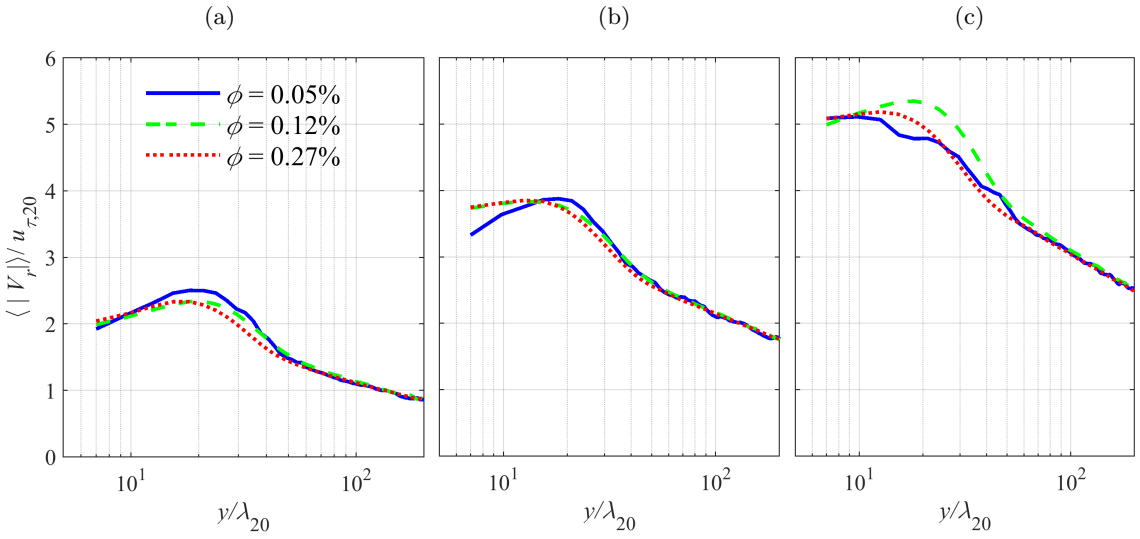

Figure 6.6: Variation of $\langle|v_r|\rangle$ as a function of λ_{20} at (a) Re = 20,000, (b) Re = 40,000, and (c) Re = 60,000.

The probability density functions (PDF) of the radial relative velocity between the detected pairs at $0 < y/h < 0.2$ and Re of 20,000, 40,000, and 60,000 are presented in Figure 6.7. The relative velocities at all Reynolds numbers are normalized by the friction

velocity at Re = 20,000 ($u_{\tau,20}$). The effect of volumetric concentration is also shown in this figure. The PDFs are calculated as the ratio between the number of data in each bin (Δv_r = 0.1 m/s) and the average number of data per bins. Because of the normalization, the areas under all plots are the same. Negative values of v_r correspond to the pairs of the beads approaching one another where collision is likely to occur. On the other hand, positive values of v_r represent the beads departing from each other and may belong to the state after the collision.

The PDFs show symmetric distribution with a peak at zero. It can be seen in Figure 6.7 that the peak has the largest value at $\phi_v = 0.05\%$ for all the Re. At larger concentrations of 0.12% and 0.27%, the PDFs become wider with smaller peak value at $v_r = 0$ compared to ϕ_v = 0.05%. However, the comparison of Figures 6.7a-c shows that the effect of Re on $\langle|v_r|\rangle$ is more noticeable than the effect of volumetric concentration. The relative velocity between the beads becomes larger at higher Re due to the strengthening of the energetic eddies which are the dominant factor in creating the relative velocity between the beads [Wang et al., 2000]. Figure 6.7 represents the PDF of v_r for all the detected pairs at $0 < y/h < 0.2$. The PDFs may stretch or shorten as the y location varies. However, scrutiny of the data shows that the PDF becomes invariant when it is normalized by $\langle|v_r|\rangle$. The results of this normalization are shown in 6.8.

Estimation of $\langle|v_r|\rangle$ is required to predict the collision frequency in a turbulent flow. An analytical model was developed by Zhou et al. [1998] and Wang et al. [2000] to calculate this term for isotropic stationary turbulent flows using the eddy-particle interaction model and assuming that v_r has a Gaussian distribution. This model gives $\langle|v_r|\rangle$ as a linear function of the mean turbulent kinetic energy of beads (k_b), namely, $\langle|v_r|\rangle \sim \alpha k_b$. The constant α is a function of the beads relaxation time. Variation of $\langle|v_r|\rangle$ as a function of k_b is plotted in Figure 6.9 for the current experiments in horizontal turbulent channel flow. The quantities are normalized by $u_{\tau,20}$ and specified by the superscript '*'. It can be seen that the effect of concentration is much smaller than the effect of k_b. Hence, it is reasonable to consider $\langle|v_r|\rangle$ as a sole function of k_b that can be estimated as $(1.10 \pm 0.06)k_b$. The model developed

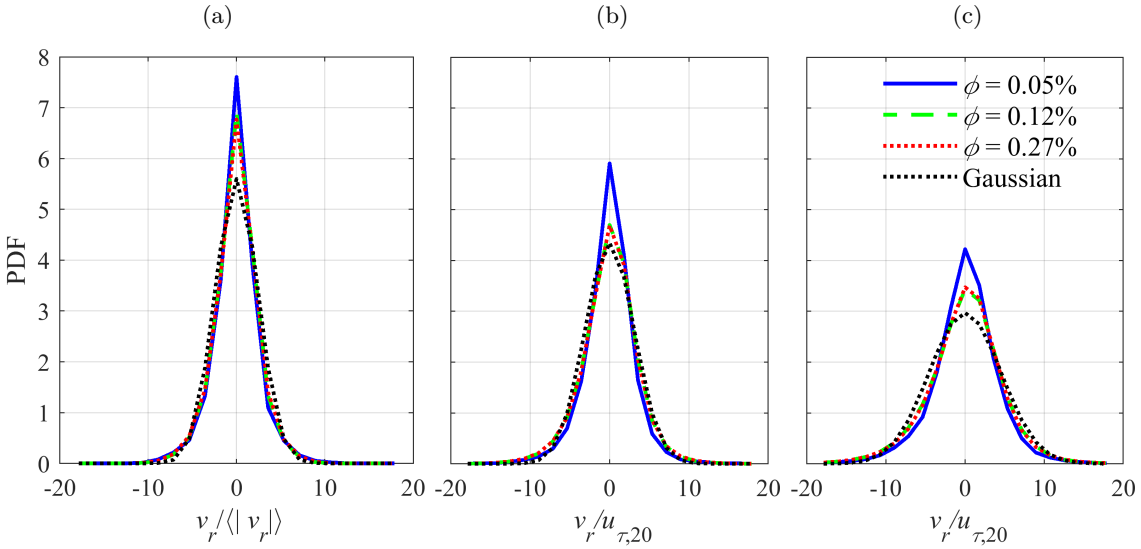

Figure 6.7: Distribution of the radial relative velocity at (a) Re = 20,000, (b) Re = 40,000, and (c) Re = 60,000 for volumetric concentrations of 0.05%, 0.12%, and 0.27%. The Gaussian distributions with standard deviation corresponds to $\phi_v = 0.05\%$ at each Re are added to the plots for comparison.

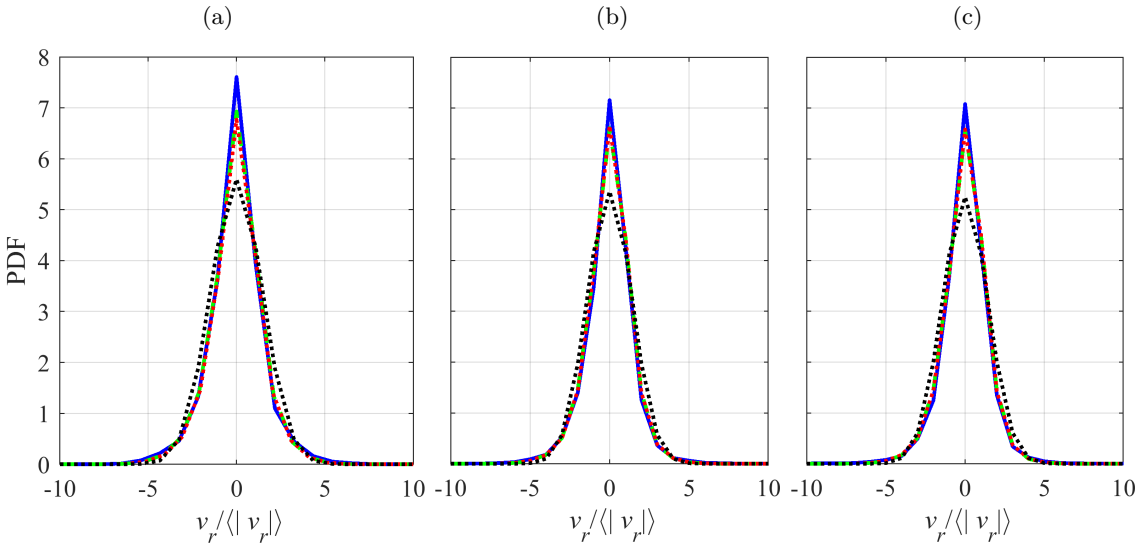

Figure 6.8: Distribution of the radial relative velocity normalized by $\langle|v_r|\rangle$ at (a) Re = 20,000, (b) Re = 40,000, and (c) Re = 60,000. For legends see Figure 6.7.

by Zhou et al. [1998] and Wang et al. [2000] with assumption of Gaussian distribution for radial relative velocity predicts $\langle|v_r|\rangle = 0.62k_b$ for the current flow conditions. In a Gaussian

distribution $\langle|v_r|\rangle/\langle|v_r^2|\rangle^{1/2} = 0.8$, while $\langle|v_r|\rangle/\langle|v_r^2|\rangle^{1/2}$ for the data presented in Figure 6.7 is 0.73 ± 0.02. The deviation from Gaussian distribution, as can be seen in Figure 6.7, and also the non-isotropic nature of the channel flow explains the discrepancy from the aforementioned analytical model.

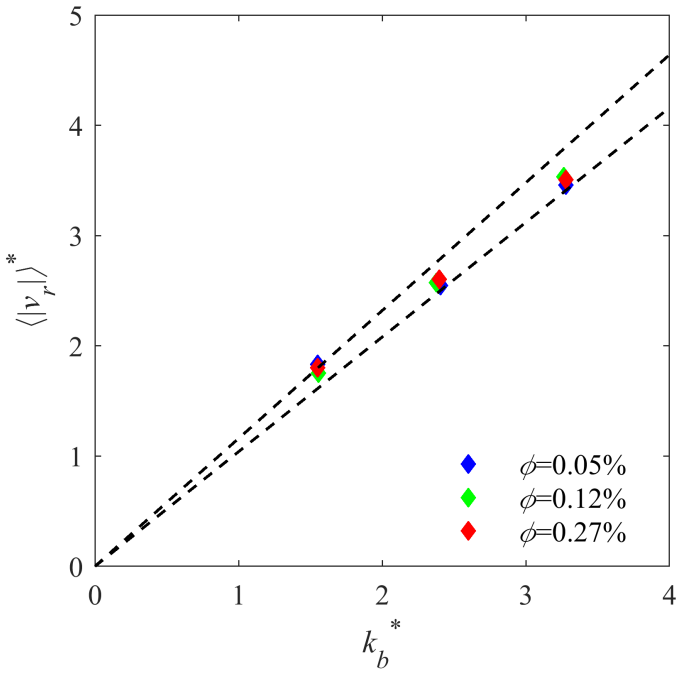

Figure 6.9: Mean value of the absolute radial relative velocity as a function of mean velocity fluctuation of particles in the measured volume ($0 < y < 3.0$ mm). The presented quantities are normalized by the friction velocity at $Re = 20{,}000$.

Only a fraction of the detected pairs in the measurement volume ($0 < y/h < 0.2$) will have collision. If the required time for the collision between a detected pair is large, the beads have sufficient time to respond to the flow and adjust themselves. Hence, the collision has less probability to occur. The estimated time required for the collision, with the assumption that the relative velocity remains constant as the beads approach each other, is calculated as

$$\tau_c = \frac{|\boldsymbol{x}_r - d_b|^2}{\boldsymbol{v}_r . (\boldsymbol{x}_r - d_b)}. \tag{6.4}$$

The estimated collision time for the beads approaching each other is normalized by the time scale of the beads, $\tau^+ = \tau_c/\tau_b$, and its PDF is presented in Figure 6.10. The bin

size for τ^+ is considered 0.2, and the number of data in each bin is divided by the average number of data in all the bins. Here, zero τ^+ means the beads are in contact with each other. It was noted in Section 3.4 that the pathlines with a distance smaller than 2.0 pix (or 180 µm) to each other are removed from the data set. This threshold is smaller than the distance between the centroid of two beads when touching each other. Hence, applying this criterion has no significant effect on the results presented in Figure 6.10. The profiles reach a peak at a small τ^+ and become very small at $\tau^+ \sim 6$. Figure 6.10 shows that the PDF of τ^+ is narrower at larger Re; the peaks move toward zero and its value becomes larger. The peak occurs at $\tau^+ = 0.35$ for Re = 20,000, $\tau^+ = 0.25$ for Re = 40,000, and $\tau^+ = 0.15$ for Re = 60,000. The peak location is almost independent of the concentration. When τ^+ is about one and smaller, the beads do not have sufficient time to respond to the local flow, and the collision is more probable to occur.

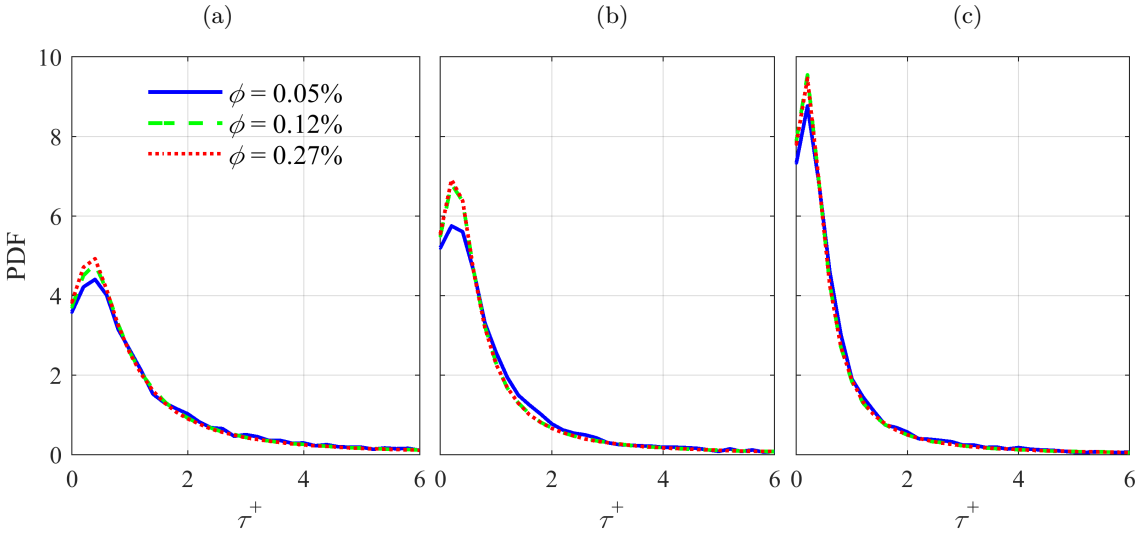

Figure 6.10: Distribution of the estimated time before collision for the beads with centroid distance smaller than $5.0d_b$ at (a) Re = 20,000, (b) Re = 40,000, and (c) Re = 60,000 for volumetric concentration of 0.05%, 0.12% and 0.27%.

The cumulative distribution of $|\tau^+|$ and its variation with Re and bulk concentration is shown in Figure 6.11. The results show that increasing the Re improve the chance of collision for a pair of nearby beads. Around 60% of the pairs at Re = 20,000 has $\tau^+ < 1.0$;

this fraction rises to 70% at $Re = 40{,}000$ and 77% at $Re = 60{,}000$.

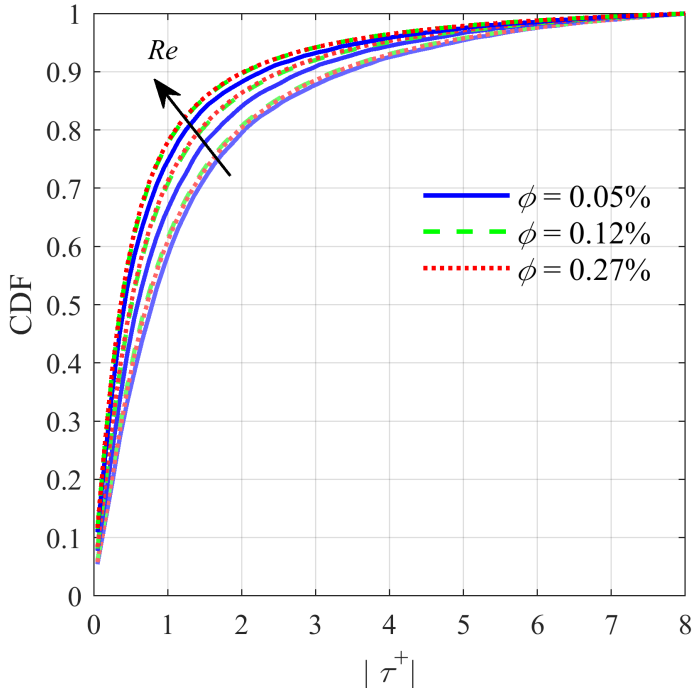

Figure 6.11: Cumulative distribution of $|\tau^+|$ for Re of 20,000, 40,000, and 60,000.

6.8 Particle trajectory

The coherence of the beads motions is investigated in this section. For this purpose, the temporal autocorrelation of the velocity fluctuation of the beads is calculated from their Lagrangian trajectory. This autocorrelation function is defined as $\rho_{uu}(s) = \langle u(t)u(t+s)\rangle / \langle u(t)^2\rangle$. Variation of ρ_{uu} as a function of $t^+ = s/\tau_{f,20}$ are shown in Figure 6.12 for Re of 20,000, 40,000, and 60,000. The coefficients are calculated for the pathlines originated at two wall-normal intervals: an inner interval at $y/h < 0.02$, and an outer interval at $0.16 < y/h < 0.18$. For each Re, the intervals correspond to a different y^+ zone as can be seen in the figures. For each data set, 10,000 pathlines with a minimum length of 70 time steps are used to calculate the coefficients.

In general, the autocorrelation coefficients reduce with increasing time distance. Figure 6.12 also show that the correlation coefficients, and consequently the time scale of the

beads' motion, become larger at farther distances from the wall. This is due to the larger length and time scales of turbulent structures at larger distances from the wall. The results represented in Figure 6.12 show a general trend for the effect of concentration on the ρ_{uu}. The autocorrelation coefficients become larger with the increase of concentration. One reason is the dampening of the turbulence at larger concentrations as discussed in Section 6.5. At smaller turbulence intensities, the beads can keep their motion for a longer time, consequently, show a larger time scale or autocorrelation coefficient.

Larger ρ_{uu} at higher concentrations in the near-wall region corresponds to a larger integral time scale of the beads motion, T_b. Larger T_b refers to a more coherent motion in the near-wall region for $\phi_v = 0.12\%$ and 0.27% at Re of 40,000 and 60,000. This can indicate that the beads motion are stabilized in a narrower region due to the lubrication effect. This can lead to an accumulation of the particles in the near-wall region as observed in Figures 6.2b and 6.2c for $\phi_v = 0.12\%$ and 0.27%.

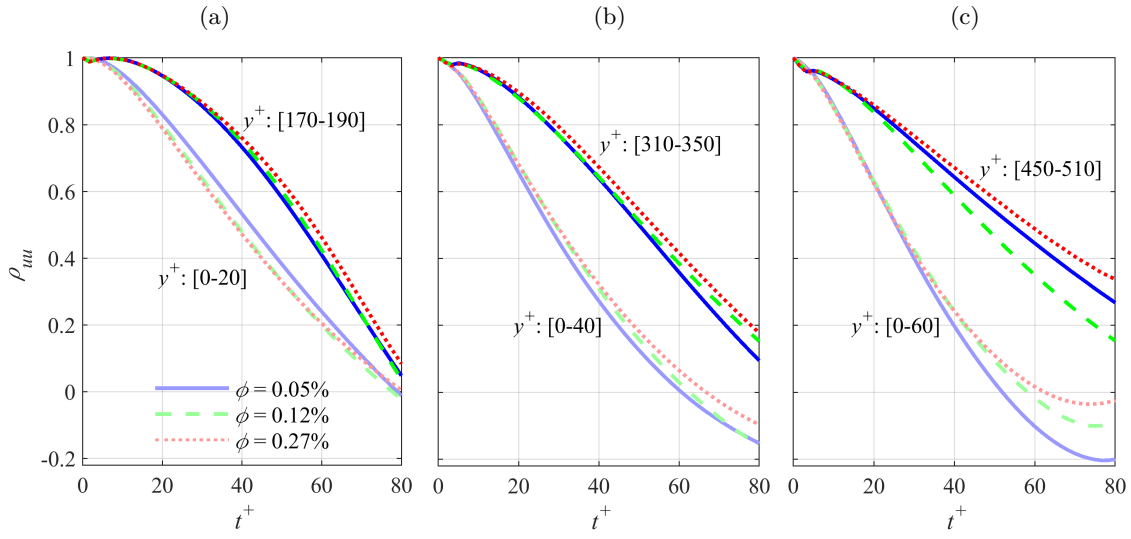

Figure 6.12: Temporal autocorrelation of streamwise velocity fluctuation of the beads at Re of (a) 20,000, (b) 40,000, and (c) 60,000.

6.9 Conclusion

Distribution of glass beads in the near-wall region of a turbulent channel flow was investigated using a time-resolved three-dimensional particle tracking velocimetry (3D-PTV) based on the shake-the-box method. Beads with a diameter of 210 µm were used to produce suspensions with the bulk volumetric concentrations of 0.05%, 0.12%, and 0.27%. The measurements were carried out at three Re of 20,000, 40,000, and 60,000. The Re was calculated based on the channel height and average velocity in the channel.

The Rouse number, $P = V_s/\kappa u_\tau$, was 1.30 at Re = 20,000. The stronger effect of gravitational settling than turbulence dispersion at this Re resulted in a monotonic increase of local concentration toward the wall. Number density profiles reached a maximum at $y \sim d_b$. The effects of shear-induced lift force became more important at larger Re. At Re of 40,000 and 60,000, the lift force due to the mean shear in the flow created a net migration of the beads toward the channel centerline at small concentrations ($\phi_v = 0.05\%$). In these cases, the distribution profile showed a minimum at $y^+ \sim 200$, and the local concentration increased beyond this point. This trend vanished at denser suspensions with $\phi_v = 0.12\%$ and 0.27% due to the action of inter-particle collisions and lubrication effects. The larger number of collisions reduced the mean-free path of beads between collisions that did not allow the beads to escape from the concentrated regions near the wall. This trend also did not happen at Re = 20,000 since the gradient term was small, and the lift force was not strong enough to create a net migration of the beads toward the core region.

It was observed that the normalized concentration of the beads increases near the wall with the increase of volumetric concentration. This can be due to the action of inter-particle collisions and wall-lubrication force. At higher concentrations, the beads experience a larger number of inter-particle collisions. This confined the beads in concentrated regions and increased the local concentration near the wall. The collision frequency in particle-laden flows is proportional to the average relative velocity between neighbor beads ($\langle|v_r|\rangle$). Pairs of the beads with the central distance smaller than $5.0d_b$ were detected to study v_r. The investigation of radial relative velocity between the beads showed that $\langle|v_r|\rangle$ was mainly a

function of the turbulent kinetic energy of the beads. Investigating the variation of $\langle|v_r|\rangle$ as a function of y^+ revealed that $\langle|v_r|\rangle$ reaches a maximum at $y^+ \sim 20$. This is the region where the turbulent kinetic energy also has its maximum magnitude.

It was also observed that the beads motion in the near-wall region had a larger integral time scale for $\phi_v = 0.12\%$ and 0.27% at Re of 40,000 and 60,000. Larger integral time scale means a more coherent motion which can be the result of the wall-lubrication effect. The lubrication force can stabilize the beads motion in the near-wall region. This is in agreement with the observed near-wall accumulation of particles for larger concentrations of $\phi_v = 0.12\%$ and 0.27% at Re of 40,000 and 60,000.

Chapter 7

Particle-Turbulence Momentum Coupling

A remarkable effort has been made by many researchers during the past decades to understand the physics of particle transfer in turbulent flows. The dispersion of inertial particles plays an important role in both environmental and industrial processes. Accurate prediction of different forces acting on a particle is crucial in the modeling and simulation of the beads dynamic in particle-laden flows. The quasi-steady drag is the main component in momentum coupling between the particle and fluid. The viscous-unsteady force (also called Basset history force) is another force that contributes to the beads' acceleration. This force is not investigated sufficiently despite its importance in solid-liquid turbulent flows. It is aimed in this chapter to investigate the quasi-steady and viscous-unsteady terms using the measured instantaneous velocity of the particles and their surrounding fluid.

7.1 Introduction

The equation of motion for a small rigid bead was developed by Tchen [1947] and Maxey and Riley [1983] and is known as the Basset-Boussinesq-Oseen (BBO) equation. Neglecting the body forces, this equation can be written for finite particle Reynolds number, Re_p, as

$$m_b \frac{d\boldsymbol{U}_b}{dt} = \underbrace{3\pi d_b \mu f_d \left(\boldsymbol{U}_f - \boldsymbol{U}_b\right)}_{F_{qs}} + \underbrace{m_f \frac{D\boldsymbol{U}_f}{Dt}}_{F_{sg}} + \underbrace{m_f C_M \left(\frac{D\boldsymbol{U}_f}{Dt} - \frac{d\boldsymbol{U}_b}{dt}\right)}_{F_{am}} + \underbrace{3\pi d_b \mu \int_{-\infty}^{t} K_B(t-\tau) \frac{d(\boldsymbol{U}_f - \boldsymbol{U}_b)}{d\tau} d\tau}_{F_{vu}} . \tag{7.1}$$

The left-hand side of the equation represents the net force on a bead as a product of the net acceleration and mass of the bead (m_b). Here, the velocity vector is specified by $\boldsymbol{U}$ and the subscripts f and b refer to the fluid phase and the beads, respectively. It should also be noted that $\boldsymbol{U}_f$ refers to the undisturbed fluid velocity at the bead position. The right-hand side of the equation shows the contribution of quasi-steady force F_{qs} (often called the Stokes drag), the stress-gradient force F_{sg}, the added-mass force F_{am}, and the viscous-unsteady force F_{vu} (also known as the Basset history force) from left to right. In this equation ρ, μ, and ν stand for density, viscosity, and kinematic viscosity of the fluid, and d_b is the diameter of the bead. In this equation, C_M is the added-mass coefficient, and m_f is the mass of fluid displaced by the particle. The added-mass term arises from the temporal acceleration of the particle and its surrounding fluid. The last term in the equation is the Basset history force which accounts for the unsteady viscous effects.

The early researches on the particle dynamics focused on an isolated particle usually located in a uniform flow at small particle Reynolds number [Mei, 1992, Bagchi and Balachandar, 2002, Limacher et al., 2018]. The analysis becomes more complicated at the presence of the wall which creates spatial nonuniformity in the flow. Presence of other particles, such as the case in particle-laden flows, also affects the situation through the inter-particle interaction and backward coupling at relatively dense flows [Ling et al., 2013]. The quasi-steady force is the most dominant one on the particles in gas-solid flows where $\rho_b/\rho_f \gg 1$. However, the inertial forces (added-mass and stress-gradient) and history force become important in solid-liquid flows where $\rho_b/\rho_f \sim 1$. The scaling analysis of Bagchi and Balachandar [2002] showed that the ratio of the inertial and history forces to the quasi-

steady force are

$$\frac{F_{am} + F_{sg}}{F_{qs}} = \frac{1}{\rho_b/\rho_f + C_M}, \tag{7.2}$$

and

$$\frac{F_{vu}}{F_{qs}} = \frac{1}{\sqrt{\rho_b/\rho_f + C_M}}. \tag{7.3}$$

For the simplest situation of one spherical particle in a free stream $C_M = 0.5$, which often serves as a reference value in two-phase applications. Simcik and Ruzicka [2013] calculated the added-mass coefficient in different flow situations including isolated and array of spherical and ellipsoidal particles. It was observed that C_M is smaller than 0.5 away from the wall and reduces slightly with the increase of the volumetric concentration of particles. This coefficient for a single particle moving parallel to the wall also reaches 0.58 at very small distances from the wall.

Several numerical and experimental evidence has shown that the viscous-unsteady force has a significant contribution to the acceleration of the particles moving close to a surface [Armenio and Fiorotto, 2001, Olivieri et al., 2014]. Olivieri et al. [2014] investigated the effect of this force on particle clustering in an isotropic homogeneous turbulent flow. It was observed that this force is responsible for about 10% of the total acceleration of the particles. Numerical analysis of Armenio and Fiorotto [2001] also showed that in a solid-liquid flow with a density ratio of 2.65, the ensemble average of the ratio of viscous-unsteady force to quasi-steady drag over time is about 0.4 that remains almost constant with an increase in density ratio. Traugott and Liberzon [2017] found out that the magnitude of the viscous-unsteady force is approximately one-half of that of the lift force that results in the suspension of buoyant particles in the liquid flow. However, the viscous-unsteady force is often neglected in numerical investigations since a history integral needs to be calculated which is computationally time and memory consuming.

The viscous-unsteady force arises due to the temporal delay in the development of the boundary layer around suspended particles. This term contains a kernel, $K_B(t)$, that decays as $t^{-1/2}$ in the limit of zero particle Reynolds number [Basset and Strutt, 1888]. It was later observed that the kernel of the Basset force at finite Re_p has a decay rate of -1/2 at small

times and a decay rate of -2 at larger times. The relation proposed by Mei and Adrian (1992) for Basset kernel was provided in Eqs. 2.26 and 2.27 which are repeated here

$$K_B(t-\tau) = \left\{ \left[\frac{4\pi\nu(t-\tau)}{d_b^2} \right]^{1/4} + \left[\frac{\pi |\boldsymbol{U}_f - \boldsymbol{U}_b|^3 (t-\tau)^2}{d_b \nu f_h} \right]^{1/2} \right\}^{-2}, \tag{7.4}$$

where

$$f_h = \left[0.75 + 0.105 \left(\frac{d_b |\boldsymbol{U}_f - \boldsymbol{U}_b|}{\nu} \right) \right]^3. \tag{7.5}$$

The review of the literature reveals that very little information is available on nature of the flow field and the resulting forces in turbulent channel flow where the turbulence is non-homogeneous and non-isotropic. In the current investigation, The quasi-steady and viscous unsteady forces on the particles in a horizontal turbulent channel flow at the bulk Reynolds number of 20,000 are calculated. Glass beads with a diameter of 210 µm are used to produce suspension at a volumetric concentration of 0.05%. The magnitude of the Basset kernel and the time interval required for its calculation are also investigated at various particle Reynolds numbers. The contribution of the quasi-steady drag to the particle acceleration is calculated. For this purpose, the three-dimensional instantaneous velocity of the beads and their surrounding fluid is measured using time-resolved volumetric particle tracking velocimetry based on the shake-the-box (STB) algorithm [Schanz et al., 2016].

7.2 Experimental Design

A set of spherical glass beads with nominal diameter (d_b) of 210 µm was used as the particulate phase. The beads had a density (ρ_b) of about 2600 kg/m^3. The beads had a narrow distribution with a standard deviation of about 20 µm. The experiments were conducted at the bulk volumetric concentrations (ϕ_v) of 0.05% and Re of 20,000. The Re is calculated based on the channel height (h) and average velocity (U_{avg}) at the test section.

A set of experiment was also performed in unladen flow to characterize the turbulence in the channel. The results of this experiment were provided in Section 6.3. In these experiments, the liquid flow was seeded with 2 µm silver-coated glass beads (SG02S40

Potters Industries) with a density of 4.0 gr/cm^3. The tracers were smaller than the wall unit with a small response time of 1.0 µs. This results in the St^+ of 4.4×10^{-3}. The inner time scale of the turbulent flow is used to calculate St^+. The experimental conditions remain the same as Chapter 6, and the flow conditions and inner scales can be found in Tables 6.1 and 6.2 for Re = 20,000.

The measurement system and imaging setup were detailed in Section 3.4. The pathlines of the beads and fluid tracers were obtained using a Lagrangian three-dimensional particle tracking velocimetry based on the STB method [Schanz et al., 2016]. Quadratic regression was applied to the detected trajectories to enhance the accuracy of particle positioning and to obtain the particle velocity using a script developed in MATLAB (R2018a, MathWorks). The kernel size of the regression was selected based on the method used by Voth [2000] and Ebrahimian et al. [2019]. It was observed that the variance of streamwise acceleration deviates from the fitted exponential function and increases noticeably due to particle positioning errors for the kernel size smaller than 7 time steps. Therefore, the kernel size of 7 was selected for regression, and the instantaneous velocity of the beads was obtained from the coefficients of the fitted quadratics.

7.3 Estimation of undisturbed fluid velocity

The quasi-steady and viscous-unsteady terms contain the slip velocity term, $U_f - U_b$, which is the difference between the beads velocity and fluid velocity estimated at the centroid of the beads. In optical measurements, the tracers in the vicinity of the beads are usually used to estimate the flow velocity at the beads centroid. Meller and Liberzon [2015] and Traugott and Liberzon [2017] used the inverse distance weighting interpolation method to estimate the fluid velocity at the bead position. They used the velocity of surrounding tracers obtained from 3D-PTV and estimated the undisturbed fluid velocity as

$$U_f = \frac{\Sigma_i U_i r_i^{-n}}{\Sigma_i r_i^{-n}}. \tag{7.6}$$

Here, n should be determined empirically, and r_i is the distance between the tracer and bead centroid as depicted in Figure 7.1. Traugott and Liberzon [2017] proposed $n = 3$ based

on their 3D-PTV data in a turbulent boundary layer.

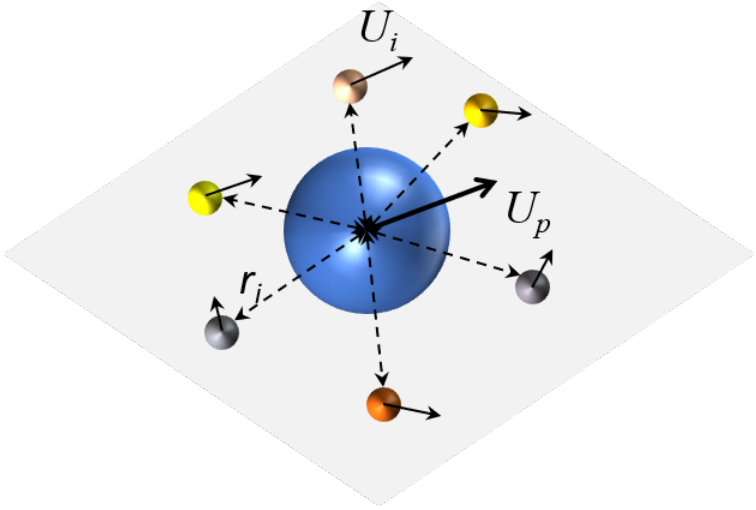

Figure 7.1: Interpolation of fluid velocity at the beads centroid using the velocity of surrounding tracers.

This method is computationally simple and accurate if enough number of tracers exist in the vicinity of the beads. However, it is difficult to have enough tracers in a small volume around a bead due to the limitation on the particle image density. This challenge becomes more serious in case of calculating the Basset force since it needs tracking of a bead and its surrounding tracers through successive time steps. The beads may cover the tracers or the tracers may leave the close vicinity of the bead during the tracking. This condition reduces the number of successfully tracked beads required for statistical convergence.

In this study, the vortex-in-cell plus (VIC+) method developed by Schneiders and Scarano [2016] was used to reconstruct the instantaneous velocity field of the liquid phase from the time-resolved PTV data. This technique employs both instantaneous velocity and Lagrangian derivative of velocity to reconstruct the velocity field on a regular fine grid. Here, a two-dimensional median filter was first applied to separate the image of particles and tracers as explained in Section 3.2. After the phase discrimination and applying STB, the velocity of liquid tracers was employed to reconstruct the velocity fields using VIC+. This process was performed in Davis 10 (LaVision GmbH). The reconstructed velocity was

considered as the undisturbed velocity field, and U_f was interpolated at the location of beads centroids. The grid size was considered equal to 8 voxels (0.64 mm) which discretized the field of view into 6 vectors in the wall-normal direction.

7.4 Results and discussions

The momentum transfer between the beads and their surrounding fluid arises due to the velocity difference between them. The forces acting on the beads mainly depends on the slip velocity and Re_p. The mean velocity profile of the beads and the fluid phase is presented in Figure 7.2a. It is shown that the beads have a smaller mean velocity than the fluid phase at $y/h > 0.12$ which is due to the preferential accumulation of the beads in the low-speed regions. The beads migrating from the central regions toward the wall retain their streamwise velocity for a longer time than the fluid phase because of their larger inertia. This result in a larger mean velocity of the beads than the fluid phase in the near-wall region.

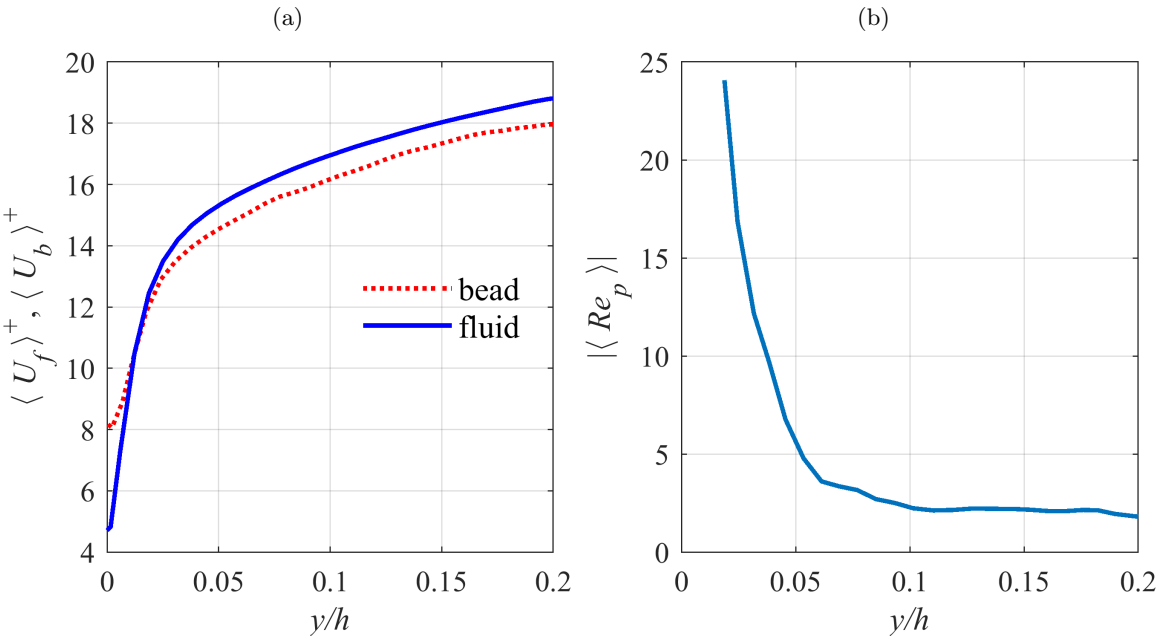

Figure 7.2: Variation of (a) mean velocity of the beads and the fluid phase normalized by the friction velocity, and (b) absolute value of the mean particle Reynolds number as a function of y/h.

The kernel of the Basset force and the correction factor in the quasi-steady term (f_d) is a function of the Re_p. Particle Reynolds number is defined based on the difference between the velocity of the bead and fluid velocity interpolated at the centroid of the beads (also called undisturbed fluid velocity). Variation of the absolute value of Re_p at $0 < y/h < 0.2$ is shown in Figure 7.2b. It can be seen that it reduces from ~ 25 in the near-wall region to ~ 2.0 at $y/h = 0.2$. The larger value of Re_p near the wall is due to the larger St in this region that reduces the velocity fidelity of the beads to the local flow. The finite value of Re_p implies the deviation of the flow field around the beads from the Stokes regime and highlights the necessity of using the correction factor (f_d) for quasi-steady force and the modified version of the Basset kernel.

Probability density function (PDF) of the acceleration of the beads and the fluid phase in the streamwise, wall-normal, and spanwise directions normalized by their standard deviations (σ_{a_i}) are shown in Figure 7.3. The distributions are scaled to have a maximum value of the PDF equal to unity. This lets an easier comparison of the PDFs between various values of a_i/σ_{a_i}. The figure shows that all PDFs are almost identical at $|a_i/\sigma_{a_i}| \leq 6$, and the PDF values reduce below 10^{-4} beyond this range. The similarity between the distribution of normalized acceleration of tracers and inertial beads was observed before in homogeneous and isotropic turbulent flows. The experimental investigation of Meller and Liberzon [2015] in a quasi-homogeneous and quasi-isotropic turbulent flow showed that the acceleration PDF of relatively small particles is independent of the particle size and density. Experiments of Qureshi et al. [2007] in an isotropic flow also showed that normalized acceleration PDF has a universal behavior in the size range of $d_b = 12 - 25\eta$. Here, η refers to the dissipative or Kolmogorov length scale.

The distributions fit a stretched exponential function which is shown in Figure 7.3. The exponential function was proposed by Voth [2000] for PDF of acceleration in turbulent flow between counter-rotating disks as

$$P(a) = Cexp\left(\frac{-a^2}{(1 + |a\beta/\varepsilon|^\gamma)\,\varepsilon^2}\right). \tag{7.7}$$

For the current set of data, $C = 1.0$, $\beta = 0.52$, $\varepsilon = 0.75$, and $\gamma = 1.47$. Parameter C is

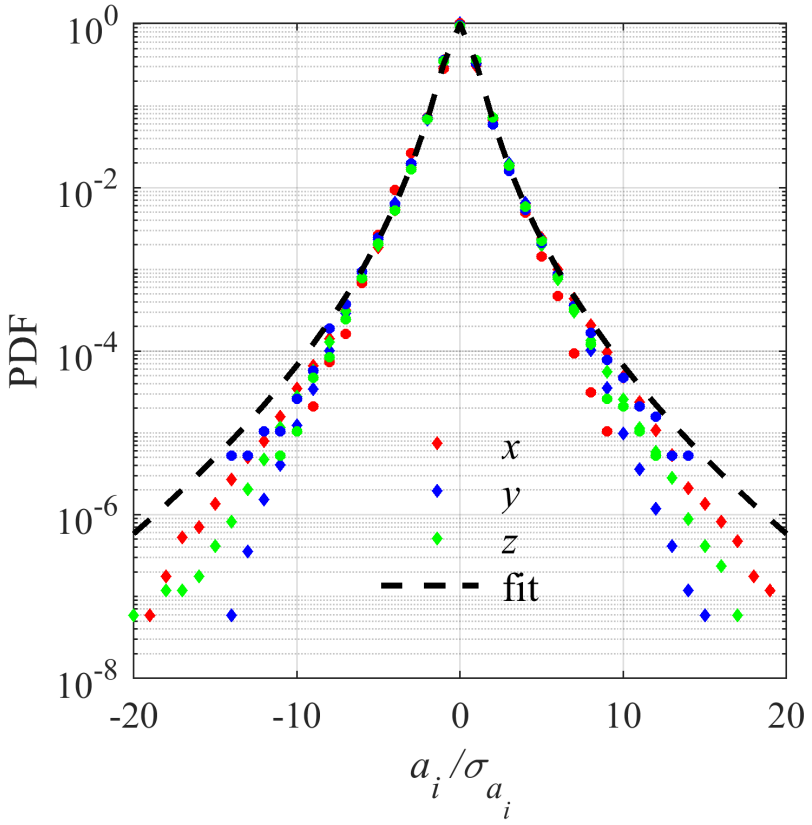

Figure 7.3: Probability density function of the acceleration of the beads and fluid phase in the x, y, and z directions normalized by their standard deviations. The beads and fluid data are presented by the filled circle and diamond markers, respectively. Different directions are specified by different colors as shown in the legend.

chosen equal to unity to get $P(0) = 1.0$. Other parameters are obtained using a nonlinear least square method.

7.4.1 Viscous-unsteady force

The acceleration due to the viscous-unsteady force on the beads is calculated in this section. This quantity will be referred to as viscous-unsteady acceleration in the rest of the chapter. This term contains an indefinite integral which includes the derivative of the relative velocity between the phases as can be seen in Eq. 7.1. It was shown later that the viscous-unsteady force only requires integration over a finite temporal range [Dorgan and Loth, 2007]. In other words, the integration converges to the solution after a finite time interval. The

other issue is that the integrand is singular when the upper integration limit is enforced, $(t-\tau) \to 0$.

In order to overcome the singularity of the integrand at $t = \tau$, the trapezoidal-based method is used to approximate the integral [van Hinsberg et al., 2011]. The integral term after the temporal discretization becomes

$$
\begin{aligned}
I(n) = \int_0^t \frac{\dot{U}}{K(t-\tau)} d\tau = \int_0^{n\Delta t} \frac{\dot{U}}{K(t-\tau)} d\tau = \\
\frac{\Delta t}{6} \Sigma_{i=1}^{n-1} \left[\frac{\dot{U}_{i-1}}{K\left(n\Delta t - (i-1)\Delta t\right)} + \frac{2\left(\dot{U}_{i-1} + \dot{U}_i\right)}{K\left(n\Delta t - (i-0.5)\Delta t\right)} + \frac{\dot{U}_i}{K\left(n\Delta t - i\Delta t\right)} \right] + \\
\frac{0.9\Delta t}{6} \left[\frac{\dot{U}_{n-1}}{K\left(\Delta t\right)} + \frac{2\left(\dot{U}_{n-1} + \dot{U}_n\right)}{K\left(0.55\Delta t\right)} + \frac{\dot{U}_n}{K\left(0.1\Delta t\right)} \right] + \\
\frac{0.1\Delta t}{2} \left[\frac{8\sqrt{2}}{3} \frac{\dot{U}_n}{K\left(0.05\Delta t\right)} - \frac{4}{3} \frac{\dot{U}_n}{K\left(0.1\Delta t\right)} \right].
\end{aligned}
\tag{7.8}
$$

The above relation estimates the integral for a finite time interval of $n\Delta t$. In this equation, the $\dot{U}$ term is used instead of $d(U_f - U_b)/d\tau$ and $K = K_B^{-1}$. The term Δt refers to the time step between the frames which is equal to the reciprocal of the image acquisition frequency, $1/f$, where $f = 2,400$ Hz. This integral is calculated for pathlines with different Re_p as a function of n to find a proper kernel size that yields converged results. The results for three sample pathlines are shown in Figure 7.4. The average Re_p along these patlines are 12.8, 35.0, and 60.0. The average Re_p for most of the detected pathlines falls within this range.

Figure 7.4 shows that the integral term approaches the converged solution with 2% accuracy after $n = 30$ for all pathlines. Consequently, $n = 30$ is chosen to calculate the viscous-unsteady term in this research. This is equivalent to $n\Delta t = 12.5$ ms. Scrutiny of the data shows that the required time interval for the calculation of the Basset force term is about $1.5\tau_{uv}$. Here, τ_{uv} is the viscous-unsteady time-scale. This time scale is defined as the time where the transition from the slower to the faster decay rate of the Basset kernel occurs. By equating the first and second terms of the Kernel term provided in Eq. 7.4, τ_{uv}

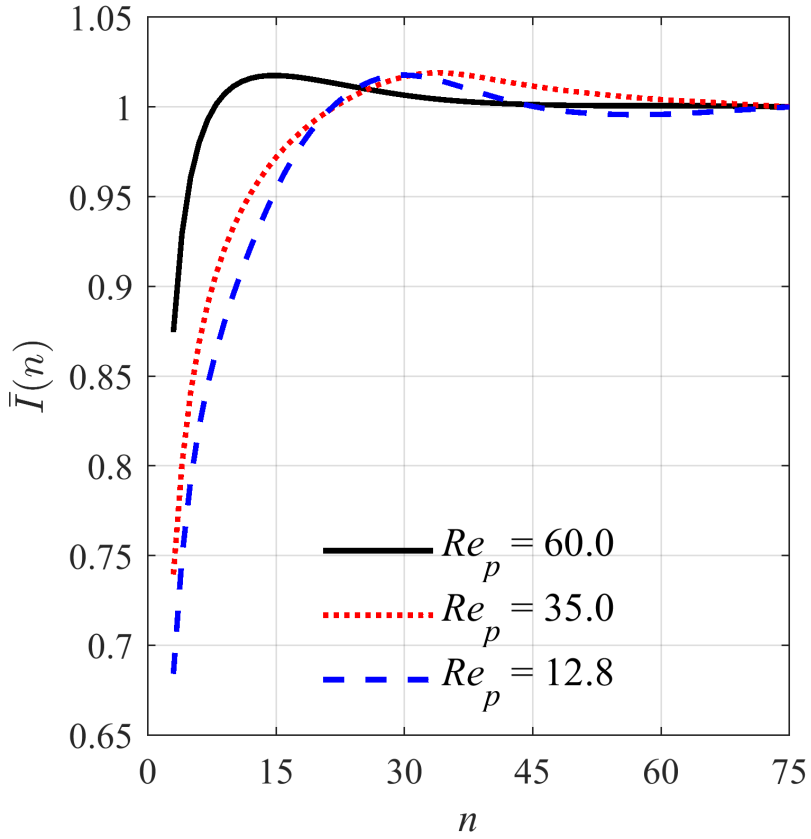

Figure 7.4: Variation of the integral term as a function of n. The results are normalized by the I ($n_{max} = 75$).

can be estimated as

$$\tau_{vu} = \left(\frac{4d_b^2}{\pi\nu}\right)^{1/3} \left(\frac{0.75 + 0.105Re_p}{Re_p}\right)^2 . \tag{7.9}$$

Variations of the Basset kernel term as a function of $t/\tau_{uv} (= n\Delta t/\tau_{uv})$ for the three selected pathlines are shown in Figure 7.5. At small values of $t/\tau_{uv} < 0.1$, Basset kernel decays as $\sim t^{-1.0}$ and the decay rate changes to -2.5 at $t/\tau_{uv} \sim 4$. It is also shown in the figure that the transition from the slower to the faster decay of the kernel occurs at $t/\tau_{uv} \sim 1.0$. At the intermediate values of $0.1 < t/\tau_{uv} < 4.0$, the effect of instantaneous Re_p on the kernel size is significant which affects the magnitude of the Basset force.

The PDF of normalized acceleration due to the Basset force in the x, y, and z directions are shown in Figure 7.6. The standard deviation, skewness, and kurtosis of the data are provided in Table 7.1. The statistics are close together in the y and z directions. The

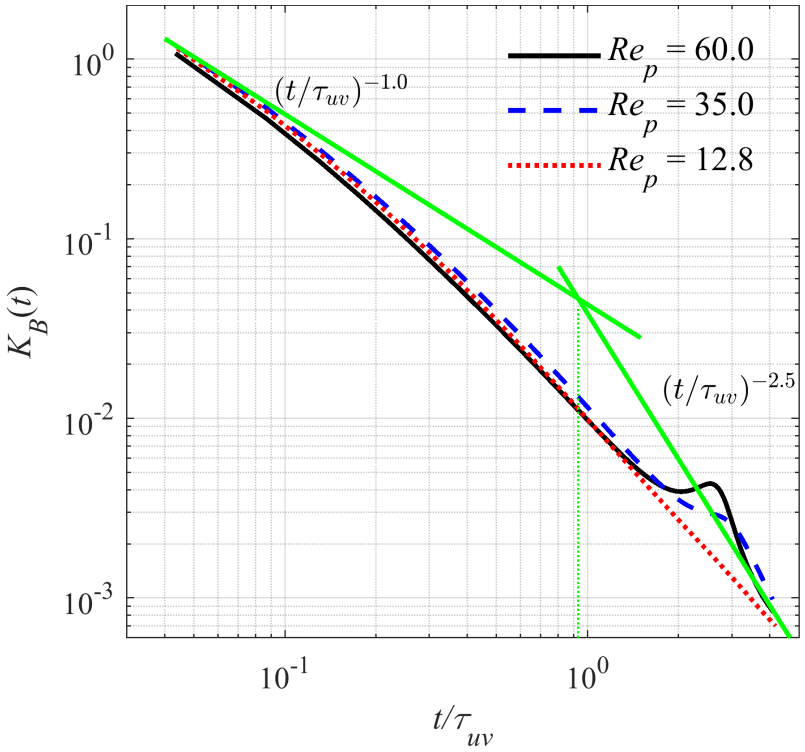

Figure 7.5: The Basset kernel (K_B) as a function of t/τ_{uv} where $t = n\Delta t$ is the kernel size used for calculation of K_B.

distributions are almost symmetrical, and the skewness of the data is close to zero. The directional preference becomes apparent in the x direction. The viscous-unsteady acceleration in x direction has larger statistical moments than other directions. This is due to the larger relative velocity in the streamwise direction. The exponential function provided in Eq. 7.7 is also used here to fit the data. The constants are $C = 1.0$, $\beta = 0.44$, $\varepsilon = 0.75$, and $\gamma = 1.47$. The fitting coefficients ε and γ remain the same for the viscous-unsteady and total acceleration. Comparison of Figures 7.3 and 7.6 also shows that the PDFs of Basset force has a weaker tail than the PDFs of the total acceleration.

The correlation of the Basset acceleration (a_B) with the total acceleration (a_T) is investigated here. For this purpose, the joint probability density function (JPDF) of a_B and a_T in the x, y, and z directions are shown in Figure 7.7. A line is also fitted to the data using the least-square method that reveals how $\langle a_B \rangle$ varies with a_T. The fitted lines have negative slopes of -0.29, -0.49, and -0.45 in the x, y, and z directions, respectively. The negative

Table 7.1: Summary of statistical moments of the viscous-unsteady force on the beads.

Direction	standard deviation	skewness	kurtosis
streamwise	1.1×10^{-7}	0.17	6.6
wall-normal	8.8×10^{-8}	-0.02	5.1
spanwise	8.1×10^{-8}	-0.02	5.0

slopes show that the Basset force tends to reduce the magnitude of the accelerations. In other words, the Basset acceleration is generally negative when the total acceleration is positive and vice versa. The bin size is considered equal to 0.2×0.2 in Figure 7.7, and the JPDF percentages vary from 1.0% to 7.0% in steps of 1.5% for the most inner to the most outer contour, respectively.

To investigate the temporal behavior of the viscous-unsteady acceleration, the power spectral density (PSD) of a_B in the x, y, and z directions are shown in Figure 7.8a. It can be seen that at small frequencies of $f < 40$ Hz, the streamwise viscous-unsteady acceleration, a_{Bx}, has a larger energy content than a_{By} and a_{Bz}. The Basset acceleration fluctuates due to the velocity fluctuation of the beads and fluid phase. It was observed by Kulick et al. [1994] that the turbulent energy is contained at higher frequencies in the transverse directions compared to the streamwise direction. The PSD plots are also normalized by the area under their curves ($\int E_a df$) and the results are shown in Figure 7.8b. The trends are almost the same as Figure 7.8a. However, the the curves cross at $f \sim 30$.

7.4.2 Quasi-steady force

The acceleration due to the quasi-steady force is calculated and scrutinized in this section. This quantity will be referred to as quasi-steady acceleration. The correction factor $f_d = 1 + 0.15Re_p^{0.687}$ is used to incorporate the effect of finite Reynolds number [Schiller and Naumann, 1933]. The scaling analysis of Bagchi and Balachandar [2002] implies that the quasi-steady force has the largest contribution to the total acceleration among all the forces included in Eq. 7.1. The PDF of the quasi-steady acceleration (a_S) in the x, y, and z directions on all the particles particles at $0 < y/h < 0.2$ are shown in Figure 7.9. The

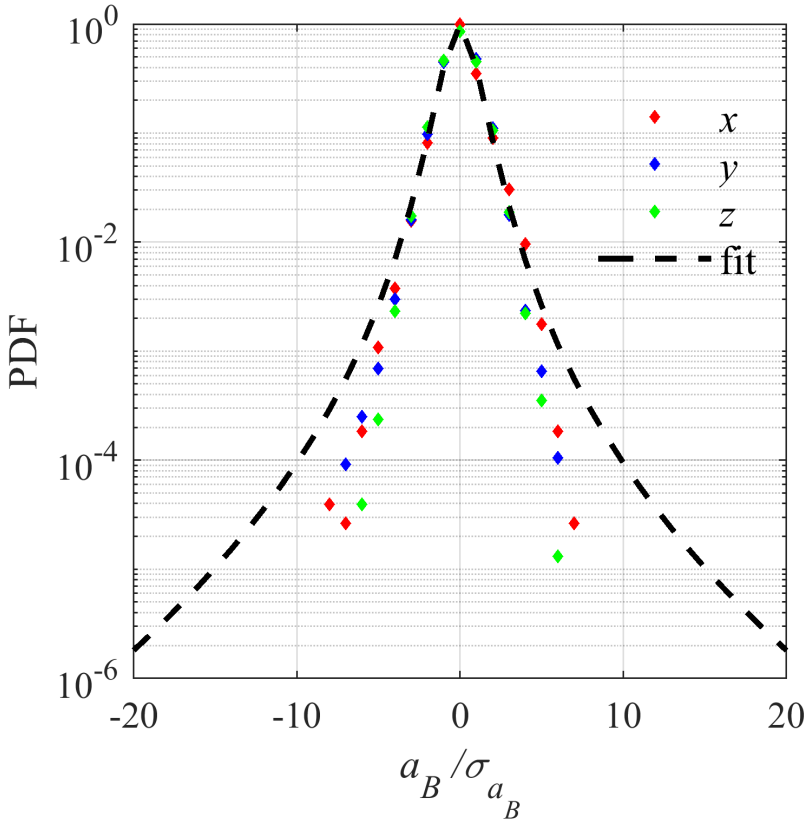

Figure 7.6: Probability density function of the viscous-unsteady acceleration of the beads in the x, y, and z directions normalized by their standard deviations.

standard deviation, skewness, and kurtosis of the data are provided in Table 7.2. The standard deviation of acceleration in the streamwise direction is around two times of that in the wall-normal and spanwise directions. This is due to the larger slip velocity in the x direction.

The streamwise quasi-steady acceleration shows a positive skewness which is larger than the skewness in transverse directions. It was shown in Figure 5.3a that the beads move slower than their surrounding flow in the near-wall region. This causes the slip velocity, and consequently, the quasi-steady force, be skewed to the right. It was also stated by Ebrahimian et al. [2019] that the fluid applies a net positive force on the beads to accelerate them in the streamwise direction. They showed that the mean streamwise acceleration is positive at $y^+ > 20$. Their experiment was performed in the same channel flow setup as

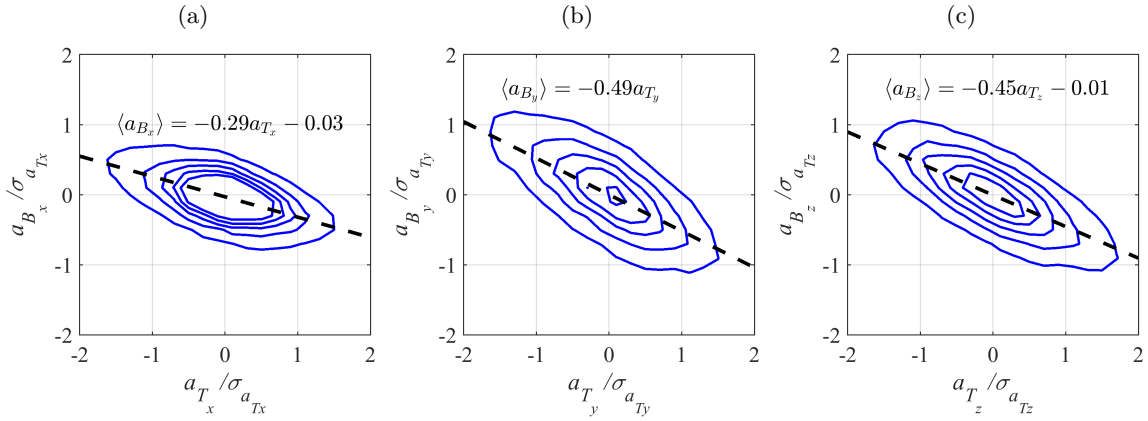

Figure 7.7: Joint probability density function of the beads total acceleration and its Basset component in (a) streamwise, (b) wall-normal, and (c) spanwise directions. The linear variations of a_B as a function of a_T are also presented in the plots.

the current study at the bulk Re of 29,000.

The stretched exponential function fitted to the data is also shown in the figure. The fitting parameters are $C = 1.0$, $\beta = 0.50$, $\varepsilon = 0.62$, and $\gamma = 1.67$.

Table 7.2: Summary of statistical moments of the quasi-steady force on the beads.

Direction	standard deviation	skewness	kurtosis
streamwise	4.2×10^{-7}	1.04	10.0
wall-normal	1.7×10^{-7}	-0.12	5.5
spanwise	2.1×10^{-7}	-0.01	5.6

The JPDFs of the quasi-steady acceleration and net acceleration in the x, y, and z directions are provided in Figure 7.10. The data is more scattered around the line calculated based on the least-square method compared to the JPDFs presented in Figure 7.7. This is due to the larger standard deviation of a_S than a_B. It can be seen in Figure 7.10a that the data are scattered around the line $\langle a_{S_x} \rangle = 1.44 a_{T_x} + 0.01$. This means that, on average, the quasi-steady force is 1.44 times of the net force applied by the fluid on a bead in the streamwise direction. This shows that the quasi-steady force is the main source of acceleration in the streamwise direction in turbulent channel flow.

Figures 7.10b and 7.10c show that the correlation between a_S and a_T becomes weaker

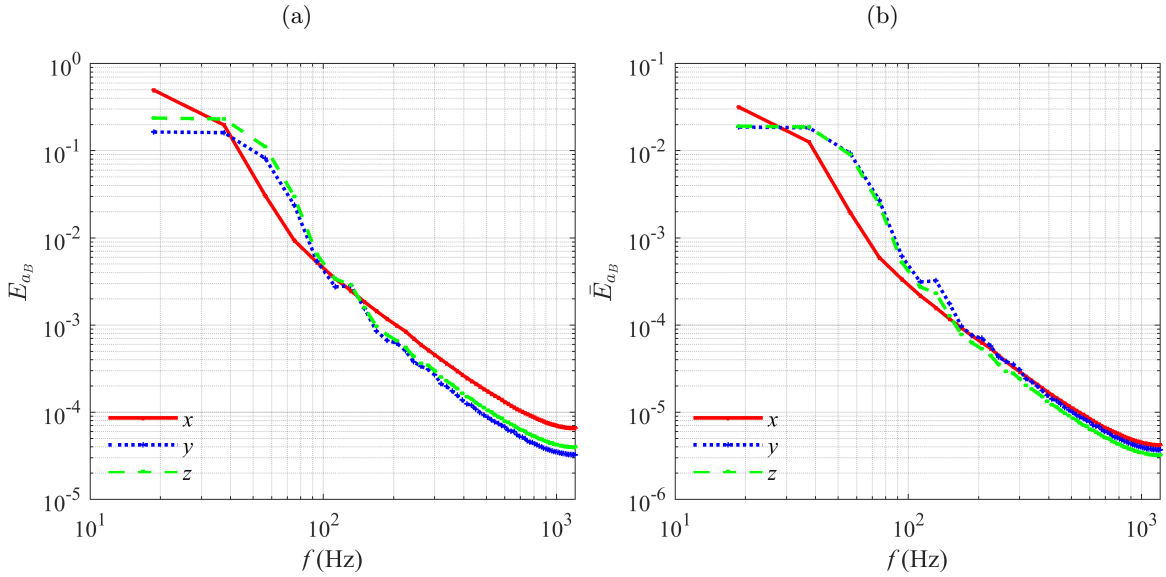

Figure 7.8: (a) Power spectral density and (b) normalized PSD ($\bar{E}_{a_B}$) of the viscous-unsteady acceleration in the streamwise, wall-normal, and spanwise directions.

in the y and z directions. The slope of the fitted line reduces to 0.15 and 0.16 in the y and z directions, respectively. The slip velocity is smaller in the y and z directions than x direction which reduces the significance of the quasi-steady force. Hence, the effect of other forces become more important. For example, the shear-induced lift force, which is neglected in Eq. 7.1, is important in the y direction near the wall. The velocity gradient is large near the wall which makes the shear-induced lift force significant. The JPDF plot in the spanwise direction is symmetrical around the origin to a considerable extent as can be seen in Figure 7.10c. This is because of the flow symmetry in the z direction.

The frequency content of the quasi-steady acceleration is shown in Figure 7.11a using spectral analysis. The acceleration has the largest energy content over the whole frequency range in the x direction. The energy content becomes smaller in the z direction and reduces to a minimum in the y direction. This trend was expected since the fluctuation in quasi-steady acceleration is directly related to the velocity fluctuation in the flow field. Since the velocity fluctuation is larger in the x direction, it generates stronger fluctuation in the streamwise acceleration. The results are also normalized by the area under the curves

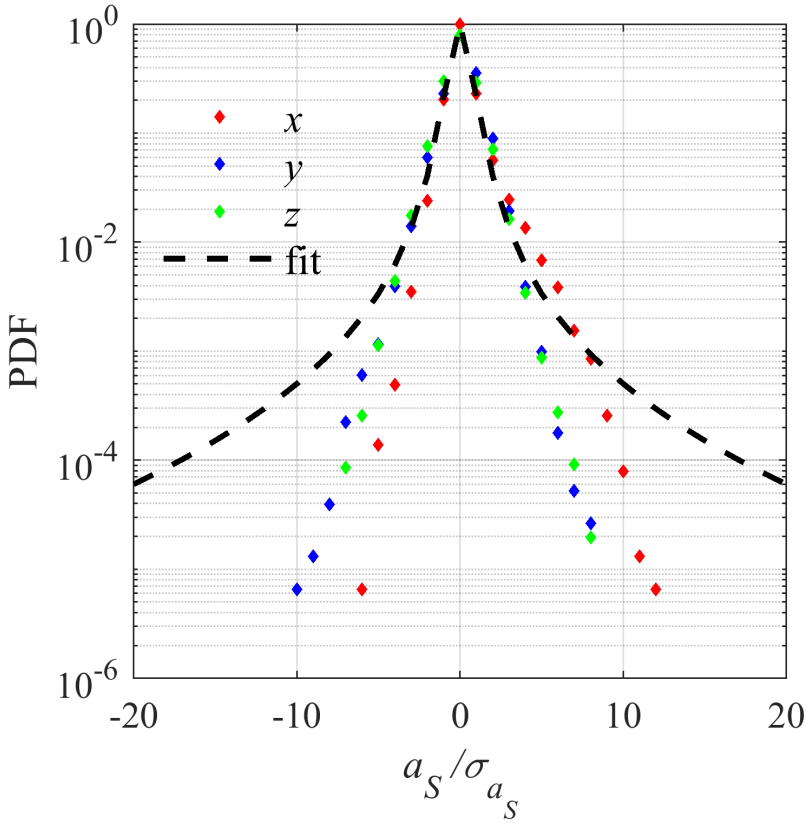

Figure 7.9: Probability density function of the quasi-steady acceleration in the x, y, and z directions normalized by their standard deviations. The stretched exponential function fitted to the data is also presented.

($\int E_a df$), and the results are provided in Figure 7.11b. The normalized energy content ($\bar{E}_{a_S}$) is larger in the streamwise direction than wall-normal and spanwise directions at small frequencies ($f < 30$ Hz). Turbulent coherent structures have a smaller size in the y and z directions than the x direction. This corresponds to a smaller time scale (larger frequency) in the fluctuation in the y and z directions. Hence, $\bar{E}_{a_S}$ in the y and z directions become larger at higher frequencies.

7.5 Conclusion

The beads dynamic was investigated in a particle-laden turbulent channel flow at $Re =$ 20,000. The particulate phase consisted of glass beads with a diameter of 210 µm and St^+ of 20.16 at a volumetric concentration of 0.05%. Three-dimensional time-resolved

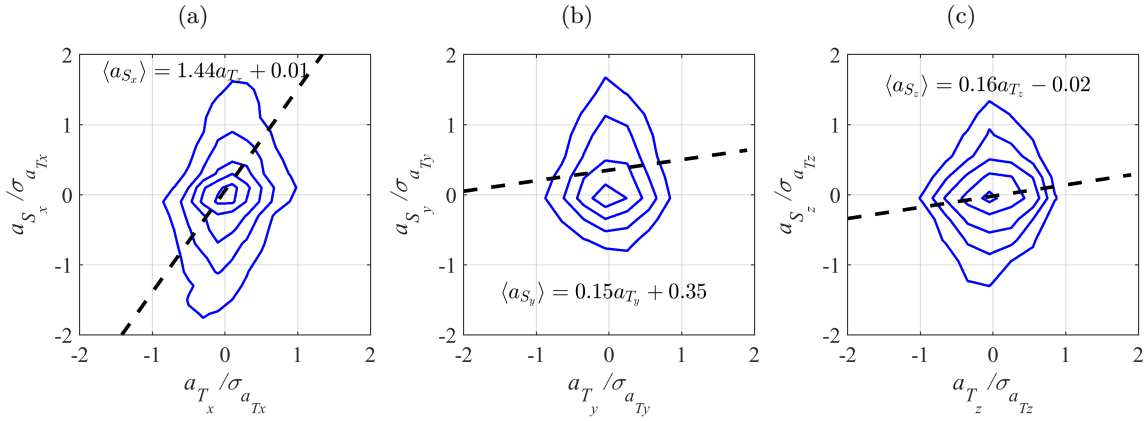

Figure 7.10: Joint probability density function of the beads total acceleration (a_T) and the quasi-steady acceleration (a_S) in the (a) streamwise, (b) wall-normal, and (c) spanwise directions. The fitted lines to the scattered data are also presented.

particle tracking velocimetry, based on the shake-the-box method, was used to measure the instantaneous velocity of the beads and the fluid phase simultaneously. The velocity of the fluid phase was used to reconstruct the fluid velocity field on a regular fine grid. The reconstructed field was then used to find the fluid velocity at the centroid of the beads to calculate the quasi-steady and viscous-unsteady forces.

A trapezoidal-based method was used to calculate the integral in the viscous-unsteady term. The effect of kernel size on the magnitude of the force was investigated for pathlines with different Re_p. The results converged when the integral calculated over 30 time steps (equal to 12.5 ms or $1.5\tau_{vu}$). The viscous-unsteady acceleration has almost identical normalized PDF and statistical moments in the y and z directions. The statistical moments became a bit larger in the x direction.

Investigation of the correlation between the viscous-unsteady acceleration and total acceleration revealed that the viscous-unsteady force mainly tends to reduce the magnitude of the acceleration. The line fitted to scattered plot of a_B and a_T had negative slopes of -0.29, -0.49, and -0.45 in the x, y, and z directions, respectively. The spectral analysis of viscous-unsteady acceleration showed that at $f < 40$ Hz, a_B has a larger energy content in the streamwise direction than transverse directions.

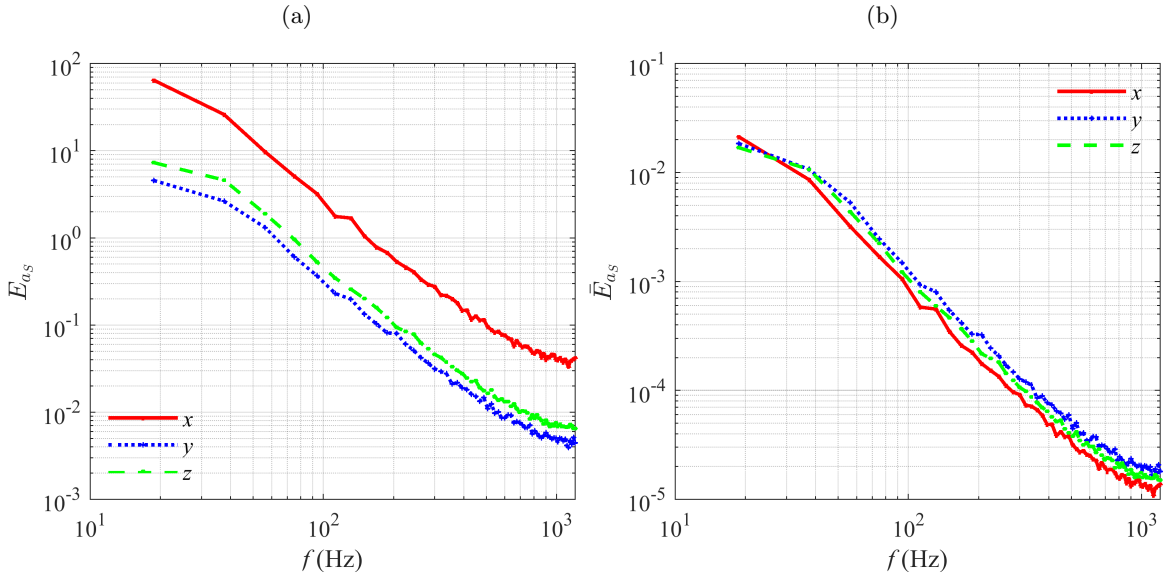

Figure 7.11: (a) Power spectral density and (b) normalized PSD ($\bar{E}_{a_S}$) of quasi-steady acceleration in the streamwise, wall-normal, and spanwise directions.

The quasi-steady force on the beads was calculated in the x, y, and z. The PDF of a_S in the y and z directions were almost symmetrical, while it showed a positive skewness in the x direction. The reason is that the beads move slower than their surrounding fluid. Therefore, the slip velocity and quasi-steady force are more likely to be positive. The statistical moments were also larger in the x direction which is due to the larger magnitude of the slip velocity in this direction.

It was shown that $\langle a_{S_x} \rangle = 1.44 a_{T_x} + 0.01$ which means that, on average, the quasi-steady force is 1.44 times the net force applied on a bead. This showed the importance of quasi-steady force in the acceleration of the beads in the streamwise direction. The significance of the quasi-steady force reduced in the y and z directions. The spectral analysis of a_S was performed to compare the frequency content of a_S in different directions. It was observed that the normalized energy content is larger in the x direction than y and z directions at small frequencies of $f < 30$ Hz.

Chapter 8

Conclusions and recommendations

The transport of particles dispersed in a horizontal turbulent channel flow was experimentally investigated. This research began with the study of velocity statistics of the solid and liquid phases and their variation with particle size, flow Re, and solid-phase volumetric concentration. Distribution of the beads over different turbulent events and also as a function of their wall-normal location were studied in the next step. The main forces acting on the beads in solid-liquid turbulent flows were also investigated. The main conclusions of these studies are presented in the first part of this chapter. The second part provides a few recommendations for further investigations in this field.

8.1 Conclusion

Investigation of turbulence modulation was performed at large Re due to the greater relevance to industrial flows. Smaller beads (d_b = 285 µm) were slower than the liquid phase over the region $0.03 < y/h < 0.5$ where the measured velocities were reliable. The velocity of particulates in the near-wall region increased with the increase of St, and the particles lead the flow. The crossing point, at which the velocity of the liquid phase and particles are the same, moves toward the channel centerline with an increase of St. Larger Re_p was also observed at larger St. When Re_p was large enough to produce vortex shedding, the augmentation of the carrier phase turbulence was significant. A maximum turbulence modulation of 7.6% was observed in the case with maximum St. In this case, Re_p reached

about 250 in the near-wall region.

The turbulence intensity of the particles mainly depended on the St. There was a St_{cr}, of the order of unity, which divided the variation of particle turbulence into two regimes. For $St < St_{cr}$, the turbulence intensity of the solid phase increased with St while it decreased for $St > St_{cr}$. When St is large, the particles do not respond quickly to the carrier phase fluctuations and less turbulent kinetic energy transfers to the particles.

The conditional averaging, based on the wall-normal velocity of the particles, showed that the streamwise velocity of the ascending beads and the nearby fluid is lower than the ensemble fluid velocity. This was associated with the preferential accumulation of the ascending beads in the low-speed regions. In comparison, the descending beads and their surrounding fluid had almost the same average velocity as the ensemble fluid. In the near-wall region, the streamwise velocity of descending beads showed a strong correlation with the surrounding fluid due to their accumulation in sweep motions. However, this correlation did not increase remarkably with increasing wall-normal distance since the preferential accumulation of descending beads in sweep motions decreased. The descending beads also had a stronger correlation with the wall-normal flow velocity. For the ascending beads, both their correlation with surrounding flow and the extent of accumulation in ejection motions increased with increasing wall-normal distance. The conditionally averaged wall-normal velocity of the fluid appeared to oppose the motion of ascending and descending beads. This observation supported the notion that the motion of a bead begins with fluid ejection that quickly decays, while the bead sustains its motion for a longer time.

A conditional sampling based on the bead acceleration showed that accelerating beads mainly move toward the channel centerline and are slower than the surrounding flow. At $y/h > 0.25$, the decelerating beads also had a larger streamwise velocity than the surrounding fluid. Hence, for both cases, the quasi-steady drag force caused by slip velocity contributed to their acceleration/deceleration. However, at $y/h < 0.25$, decelerating beads had a smaller velocity than the surrounding flow, implying that the quasi-steady force is not sufficient to model the dynamics of the nearly buoyant beads used in this study.

When the Rouse number was larger than unity (d_b = 210 µm and Re = 20,000), the effects of gravitational settling were greater than turbulence dispersion forces, which resulted in a monotonic increase of the local concentration toward the wall with a maximum at $y \sim d_b$. Other factors became important as the Rouse number reduced. At Re = 40,000 and 60,000, the shear-induced lift force created a net migration of the particles away from the wall at low concentrations ($\phi = 0.05\%$). Consequently, a core-peaking profile of local concentration was observed. This trend vanished at larger bulk concentrations of ϕ = 0.12% and 0.27%. The increased number of inter-particle collisions prevented the particles from leaving the region near the wall. Hence, a wall-peaking profile of local concentration was observed at these concentrations. The particles in denser suspensions showed a larger velocity autocorrelation coefficient compared to the particles at $\phi = 0.05\%$. This observation implied that the wall-normal position of the beads was stabilized in the vicinity of the wall at higher concentrations, and confirms the tendency of the particles to accumulate in the near-wall region.

The average relative velocity between the particles was mainly dependent on their turbulent kinetic energy. The profiles of $\langle |v_r| \rangle$ as a function of y^+ reached a maximum at $y^+ \sim 20$ where the turbulent kinetic energy also had its maximum value. The relative velocity in channel flow had a non-Gaussian distribution, and its average at $0 < y/h < 0.2$ was estimated by $(1.10 \pm 0.06)k_b$.

Investigation of the correlation between the viscous-unsteady acceleration and total acceleration revealed that the viscous-unsteady force mainly tends to reduce the magnitude of the acceleration. The line fitted to the scattered plot of a_B versus a_T had negative slopes of -0.29, -0.49, and -0.45 in the x, y, and z directions, respectively. The spectral analysis of viscous-unsteady acceleration showed that a_B had a larger energy content in the streamwise direction than transverse directions at $f < 40$ Hz.

On average, the quasi-steady force on d_b = 210 µm beads at Re =20,000 was 1.44 times of the net force on the beads. This indicates the importance of quasi-steady force in the acceleration of the beads in the streamwise direction. The importance of the quasi-steady

force reduced in the y and z directions. The spectral analysis of quasi-steady acceleration showed that at small frequencies of $f < 30$ Hz, the normalized energy content was larger in the x direction than y and z directions.

8.2 Recommendations for future studies

The research presented in this thesis has advanced the understanding of particle transport in turbulent flows. Particle-laden flow has a complex nature, and there are still many aspects which are poorly understood. A few recommendations are provided below to improve and expand the studies performed in this thesis.

Turbulent characteristics at higher concentrations

The particle volumetric concentration in industrial applications is considerably higher than the concentrations investigated in this thesis. The blockage of the line-of-sight of the cameras by the particles (i.e., occlusion) limits the concentration in optical measurements. The velocimetry algorithms are also accurate at low particle image density which further limits the concentration. One way to overcome this limitation is to match the refractive index of both the solid and liquid phases. The refractive index matching (RIM) technique can be used in combination with PIV and PTV.

Particle-fluid interaction forces in solid-liquid flows

The quasi-steady force is the main source of particle acceleration in gas-solid flows. However, other forces such as added-mass and viscous-unsteady forces become important in solid-liquid flows. There are only a few measurements of these forces in the literature, and they are limited to isotropic and homogeneous turbulent flows. Hence, it is necessary to perform more experiments to characterize the particle-fluid interaction forces in non-homogeneous and non-isotropic liquid turbulent flows.

It has been also observed in some experimental investigations (including this thesis) that the PDF of particle acceleration, when normalized by its standard deviation, is independent of the particle size. The mechanism responsible for this invariance is not explained

yet. Different forces acting on the particles should be more investigated to explain this observation.

Near-wall vortical structures in particle-laden flow

Experimental investigation of the vortical structures in the near-wall region of particle-laden turbulent flows is incomplete. Numerical simulations are also mostly performed in the one-way coupled regime using a point-particle approach. Resolving the vortical structures requires highly-resolved velocity data of the carrier phase. It was not possible to reach the required resolution in this thesis. The phase discrimination method used in this study eliminated some fluid tracers. In addition, some of the tracers were covered by the inertial particles in the images. Hence, the liquid velocity field was relatively sparse. It is suggested to seed the fluid with fluorescent particles and equip the cameras with band-pass filters to record only the fluorescent emitted light. In this method, more than four cameras are required for accurate measurement of the velocity of the solid and liquid phases simultaneously.

8.3 Industrial Relevance

An efficient transportation of slurries are crucial in a diverse range of sectors, from food to minerals processing; and oil sands processing to nuclear waste management. The characterization of solid-liquid turbulent flows is required for the design, optimization, and control of the processes involving slurry flows.

Experimental investigation of this type of flow is necessary to understand the mechanisms of particle transportation, suspension, and deposition. Providing experimental data could also provide useful data for developing and optimizing numerical multiphase flow models. This would help manage the flow to reduce the degree of erosion on pipe walls.

The erosion often leads to a reduction of hydraulic performance and affects the life of the pipes and other equipment such as the pumps. Maintenance, inspection, and replacement of the equipment result in an enormous cost. Failure of the parts due to erosion may also lead

to the shutdown of the whole transportation system. Hence, the solid transport in conduits and the resultant erosion requires an extensive investigation. However, the knowledge is still limited due to the complex nature of turbulent two-phase flows and erosion mechanism.

The erosion is mainly depends on the particle velocity, particle impingement angle, and frequency of particle impact on the surfaces. These parameters are influenced by the turbulence in the carrier phase and the local concentration of the particles near the walls. Therefore, it was aimed in the current research to investigate the particle-turbulence interaction and distribution of the particles in the near-wall region. However, it should be noted that the current investigation is conducted at concentrations smaller than the industrial pipelines. This is due to the limitation of the applied measurement system. Investigation at larger concentration of particles is recommended for future studies. To investigate particles motion in dense particle-laden flows one can use a large number of particles that their refractive index is matched with the carrier fluid along with a few particles with a different refractive index than the fluid.

References

J. Abrahamson. Collision rates of small particles in a vigorously turbulent fluid. *Chemical Engineering Science*, 30(11):1371–1379, nov 1975. ISSN 0009-2509. doi: 10.1016/0009-2509(75)85067-6. URL https://www.sciencedirect.com/science/article/pii/0009250975850676.

F. Ahmadi, M. Ebrahimian, R. Sanders, and S. Ghaemi. Particle image and tracking velocimetry of solid-liquid turbulence in a horizontal channel flow. *International Journal of Multiphase Flow*, 112, 2019. ISSN 03019322. doi: 10.1016/j.ijmultiphaseflow.2018.12.007.

A. Alajbegovic, A. Assad, F. Bonetto, and R. Lahey. Phase distribution and turbulence structure for solid/fluid upflow in a pipe. *International Journal of Multiphase Flow*, 20(3):453–479, jun 1994. ISSN 0301-9322. doi: 10.1016/0301-9322(94)90021-3. URL https://www.sciencedirect.com/science/article/pii/0301932294900213.

S. L. Anderson and E. K. Longmire. Interpretation of PIV autocorrelation mesurements in complex particle-laden flows. *Experiments in Fluids*, 20(4):314–317, 1996. ISSN 1432-1114. doi: 10.1007/BF00192676. URL https://doi.org/10.1007/BF00192676.

V. Armenio and V. Fiorotto. The importance of the forces acting on particles in turbulent flows. *Physics of Fluids*, 13(8):2437–2440, 2001. doi: 10.1063/1.1385390. URL https://doi.org/10.1063/1.1385390.

T. Atherton and D. Kerbyson. Size invariant circle detection. *Image and Vision Computing*, 17(11):795–803, 1999. ISSN 02628856. doi: 10.1016/S0262-8856(98)00160-7. URL http://www.sciencedirect.com/science/article/pii/S0262885698001607.

T. R. Auton. The lift force on a spherical body in a rotational flow. *Journal of Fluid Mechanics*, 183(-1):199, oct 1987. ISSN 0022-1120. doi: 10.1017/S002211208700260X. URL http://www.journals.cambridge.org/abstract{_}S002211208700260X.

P. Bagchi and S. Balachandar. Steady planar straining flow past a rigid sphere at moderate Reynolds number. *Journal of Fluid Mechanics*, 466:365–407, sep 2002. ISSN 0022-1120. doi: 10.1017/S0022112002001490. URL http://www.journals.cambridge.org/abstract{_}S0022112002001490.

L. J. Baker and F. Coletti. Experimental study of negatively buoyant finite-size particles in a turbulent boundary layer up to dense regimes. *Journal of Fluid Mechanics*, 866:598–629, 2019. doi: 10.1017/jfm.2019.99.

S. Balachandar and J. K. Eaton. Turbulent Dispersed Multiphase Flow. *Annual Review of Fluid Mechanics*, 42(1):111–133, 2010. ISSN 0066-4189. doi: 10.1146/annurev.fluid.010908.165243. URL http://www.annualreviews.org/doi/abs/10.1146/annurev.fluid.010908.165243.

A. B. Basset. Treatise on Hydrodynamics. *Nature*, 40(1035):412–413, 1889. ISSN 1476-4687. doi: 10.1038/040412a0. URL https://doi.org/10.1038/040412a0.

A. B. Basset and J. W. Strutt. On the motion of a sphere in a viscous liquid. *Philosophical Transactions of the Royal Society of London. (A.)*, 179:43–63, 1888. doi: 10.1098/rsta.1888.0003. URL https://royalsocietypublishing.org/doi/abs/10.1098/rsta.1888.0003.

J. Boussinesq. Theorie analytique de la chaleur. *L'Ecole Polytechnique, Paris*, 2:224, 1895.

G. Brenn, H. Braeske, G. Živković, and F. Durst. Experimental and numerical investigation of liquid channel flows with dispersed gas and solid particles. *International Journal of Multiphase Flow*, 29(2):219–247, feb 2003. ISSN 0301-9322. doi: 10.1016/S0301-9322(02)00133-7. URL https://www.sciencedirect.com/science/article/pii/S0301932202001337.

J. W. Brooke, K. Kontomaris, T. J. Hanratty, and J. B. McLaughlin. Turbulent deposition and trapping of aerosols at a wall. *Physics of Fluids A: Fluid Dynamics*, 4(4):825–834, 1992. doi: 10.1063/1.858299. URL https://doi.org/10.1063/1.858299.

T. R. Camp. Velocity gradients and internal work in fluid motion. *J. Boston Soc. Civ. Eng.*, 30:219–230, 1943.

J. Capecelatro and O. Desjardins. Mass Loading Effects on Turbulence Modulation by Particle Clustering in Dilute and Moderately Dilute Channel Flows. *Journal of Fluids Engineering*, 137(11):111102–111108, nov 2015. ISSN 0098-2202. URL http://dx.doi.org/10.1115/1.4030644.

J. Capecelatro, O. Desjardins, and R. O. Fox. On the transition between turbulence regimes in particle-laden channel flows. *Journal of Fluid Mechanics*, 845:499–519, jun 2018. ISSN 0022-1120. doi: 10.1017/jfm.2018.259. URL https://www.cambridge.org/core/product/identifier/S0022112018002598/type/journal{_}article.

M. Caporaloni, F. Tampieri, F. Trombetti, and O. Vittori. Transfer of Particles in Nonisotropic Air Turbulence. *Journal of the Atmospheric Sciences*, 32(3):565–568, mar 1975. ISSN 0022-4928. doi: 10.1175/1520-0469(1975)032⟨0565:TOPINA⟩2.0.CO;2. URL https://doi.org/10.1175/1520-0469(1975)032{%}3C0565:TOPINA{%}3E2.0.COhttp://0.0.0.2.

N. Chien and Z. Wan. *Mechanics of Sediment Transport*. American Society of Civil Engineers, 1999. doi: 10.1061/9780784404003. URL https://ascelibrary.org/doi/abs/10.1061/9780784404003.

F. H. Clauser. The Turbulent Boundary Layer. *Advances in Applied Mechanics*, 4:1–51, jan 1956. ISSN 0065-2156. doi: 10.1016/S0065-2156(08)70370-3. URL https://www.sciencedirect.com/science/article/pii/S0065215608703703.

E. R. Corino and R. S. Brodkey. A visual investigation of the wall region in turbulent flow. *Journal of Fluid Mechanics*, 37(1):1–30, 1969. doi: 10.1017/S0022112069000395.

P. Costa, F. Picano, L. Brandt, and W.-P. Breugem. Effects of the finite particle size in turbulent wall-bounded flows of dense suspensions. *Journal of Fluid Mechanics*, 843:450–478, may 2018. ISSN 0022-1120. doi: 10.1017/jfm.2018.117. URL https://www.cambridge.org/core/product/identifier/S0022112018001179/type/journal{_}article.

P. A. Davidson. *Turbulence: an introduction for scientists and engineers*. Oxford university press, 2015.

E. Delnoij, J. Westerweel, N. Deen, J. Kuipers, and W. van Swaaij. Ensemble correlation PIV applied to bubble plumes rising in a bubble column. *Chemical Engineering Science*, 54(21):5159–5171, nov 1999. ISSN 00092509. doi: 10.1016/S0009-2509(99)00233-X. URL http://linkinghub.elsevier.com/retrieve/pii/S000925099900233X.

A. Dorgan and E. Loth. Efficient calculation of the history force at finite reynolds numbers. *International Journal of Multiphase Flow*, 33(8):833 – 848, 2007. ISSN 0301-9322. doi: https://doi.org/10.1016/j.ijmultiphaseflow.2007.02.005. URL http://www.sciencedirect.com/science/article/pii/S0301932207000304.

E. Doroodchi, G. Evans, M. Schwarz, G. Lane, N. Shah, and A. Nguyen. Influence of turbulence intensity on particle drag coefficients. *Chemical Engineering Journal*, 135(1-2):129–134, jan 2008. ISSN 1385-8947. doi: 10.1016/J.CEJ.2007.03.026. URL https://www.sciencedirect.com/science/article/pii/S1385894707001702.

M. Ebrahimian, R. Sean Sanders, and S. Ghaemi. Dynamics and wall collision of inertial particles in a solid–liquid turbulent channel flow. *Journal of Fluid Mechanics*, 881:872–905, dec 2019. ISSN 0022-1120. doi: 10.1017/jfm.2019.749. URL https://www.cambridge.org/core/product/identifier/S0022112019007493/type/journal{_}article.

S. Elghobashi. Particle-laden turbulent flows: direct simulation and closure models. *Applied Scientific Research*, 48(3):301–314, 1991. ISSN 1573-1987. doi: 10.1007/BF02008202. URL https://doi.org/10.1007/BF02008202.

W. Fornari, A. Formenti, F. Picano, and L. Brandt. The effect of particle density in turbulent channel flow laden with finite size particles in semi-dilute conditions. *Physics of Fluids*, 28(3):33301, 2016. doi: 10.1063/1.4942518. URL https://doi.org/10.1063/1.4942518.

A. Fuhr, M. Krantz, and B. Fotty. An investigation into developing slurry flow conditions and their effect on wear profiles using a pilot scale flow loop. *BHR Group - 19th International Conference on Hydrotransport 2014*, pages 325–337, 01 2014.

S. Ghaemi and F. Scarano. Multi-pass light amplification for tomographic particle image velocimetry applications. *Measurement Science and Technology*, 21(12):127002, 2010. URL http://stacks.iop.org/0957-0233/21/i=12/a=127002.

R. G. Gillies and C. A. Shook. Concentration distributions of sand slurries in horizontal pipe flow. *Particulate Science and Technology*, 12(1):45–69, 1994. doi: 10.1080/02726359408906641. URL https://doi.org/10.1080/02726359408906641.

R. Gore and C. Crowe. Effect of particle size on modulating turbulent intensity. *International Journal of Multiphase Flow*, 15(2):279–285, apr 1989. ISSN 03019322. doi: 10.1016/0301-9322(89)90076-1. URL http://linkinghub.elsevier.com/retrieve/pii/0301932289900761.

Y. A. Hassan, T. K. Blanchat, C. H. Seeley, and R. E. Canaan. Simultaneous velocity measurements of both components of a two-phase flow using particle image velocimetry. *International Journal of Multiphase Flow*, 18(3):371–395, 1992. ISSN 0301-9322. doi: http://dx.doi.org/10.1016/0301-9322(92)90023-A. URL http://www.sciencedirect.com/science/article/pii/030193229290023A.

C. Ji, A. Munjiza, E. Avital, J. Ma, and J. J. R. Williams. Direct numerical simulation of sediment entrainment in turbulent channel flow. *Physics of Fluids*, 25(5):56601, 2013. doi: 10.1063/1.4807075. URL https://doi.org/10.1063/1.4807075.

J. Jiménez and A. Pinelli. The autonomous cycle of near-wall turbulence. *Journal of Fluid Mechanics*, 389:335–359, 1999. doi: 10.1017/S0022112099005066.

D. Kaftori, G. Hetsroni, and S. Banerjee. Particle behavior in the turbulent boundary layer. I. Motion, deposition, and entrainment. *Physics of Fluids*, 7(5):1095–1106, 1995. doi: 10.1063/1.868551. URL https://doi.org/10.1063/1.868551.

C. J. Kähler, S. Scharnowski, and C. Cierpka. On the uncertainty of digital PIV and PTV near walls. *Experiments in Fluids*, 52(6):1641–1656, 2012. ISSN 1432-1114. doi: 10.1007/s00348-012-1307-3. URL http://dx.doi.org/10.1007/s00348-012-1307-3.

K. Kameyama, H. Kanai, H. Kawashima, and T. Ishima. Evaluation of particle motion in solid-liquid two-phase pipe flow with downward/upward flow directions. *17th Internatonal Symposium on Applications of Laser Techniques to Fluid Mechanics*, (1982):1–15, 2014.

A. J. Karabelas. Vertical distribution of dilute suspensions in turbulent pipe flow. *AIChE Journal*, 23(4):426–434, 1977. doi: 10.1002/aic.690230404. URL https://onlinelibrary.wiley.com/doi/abs/10.1002/aic.690230404.

D. A. Khalitov and E. K. Longmire. Simultaneous two-phase PIV by two-parameter phase discrimination. *Experiments in Fluids*, 32(2):252–268, 2002. ISSN 1432-1114. doi: 10.1007/s003480100356. URL http://dx.doi.org/10.1007/s003480100356.

K. T. Kiger and C. Pan. PIV technique for the simultaneous measurement of dilute two-phase flows. *TRANSACTIONS-AMERICAN SOCIETY OF MECHANICAL ENGINEERS JOURNAL OF FLUIDS ENGINEERING*, 122(4):811–818, 2000. ISSN 0098-2202.

K. T. Kiger and C. Pan. Suspension and turbulence modification effects of solid particulates on a horizontal turbulent channel flow. *Journal of Turbulence*, 3:N19, 2002. doi: 10.1088/1468-5248/3/1/019. URL http://dx.doi.org/10.1088/1468-5248/3/1/019.

S. J. Kline, W. C. Reynolds, F. A. Schraub, and P. W. Runstadler. The structure of turbulent boundary layers. *Journal of Fluid Mechanics*, 30(4):741–773, 1967. doi: 10.1017/S0022112067001740.

J. D. Kulick, J. R. Fessler, J. K. Eaton, and E. J. K. Particle response and turbulence modification in fully developed channel flow. *J. Fluid Mech.*, 277(-1):109, oct 1994. ISSN 0022-1120. doi: 10.1017/S0022112094002703. URL http://www.journals.cambridge.org/abstract{_}S0022112094002703.

J. Kussin and M. Sommerfeld. Experimental studies on particle behaviour and turbulence modification in horizontal channel flow with different wall roughness. *Experiments in Fluids*, 33(1):143–159, 2002. ISSN 1432-1114. doi: 10.1007/s00348-002-0485-9. URL http://dx.doi.org/10.1007/s00348-002-0485-9.

S. Lain, M. Sommerfeld, and J. Kussin. Experimental studies and modelling of four-way coupling in particle-laden horizontal channel flow. *International Journal of Heat and Fluid Flow*, 23(5):647–656, oct 2002. ISSN 0142-727X. doi: 10.1016/S0142-727X(02)00160-1. URL https://www.sciencedirect.com/science/article/pii/S0142727X02001601.

I. Lashgari, F. Picano, W. P. Breugem, and L. Brandt. Channel flow of rigid sphere suspensions: Particle dynamics in the inertial regime. *International Journal of Multiphase Flow*, 78:12–24, jan 2016. ISSN 0301-9322. doi: 10.1016/J.IJMULTIPHASEFLOW.2015.09.008. URL https://www.sciencedirect.com/science/article/pii/S0301932215002062.

J. Lee, C. Lee, and L. C. Modification of particle-laden near-wall turbulence: Effect of Stokes number. *Physics of Fluids*, 27(2):23303, 2015. doi: 10.1063/1.4908277. URL https://doi.org/10.1063/1.4908277.

J. H. Lee, Kevin, J. P. Monty, and N. Hutchins. Validating under-resolved turbulence intensities for PIV experiments in canonical wall-bounded turbulence. *Experiments in Fluids*, 57(8):129, jul 2016. ISSN 1432-1114. doi: 10.1007/s00348-016-2209-6. URL https://doi.org/10.1007/s00348-016-2209-6.

M. Lee and R. D. Moser. Direct numerical simulation of turbulent channel flow up to Re_{τ}˜ 5200. *Journal of Fluid Mechanics*, 774:395–415, 2015. ISSN 0022-1120. doi: DOI: 10.1017/jfm.2015.268.

S. Lee. Particle drag in a dilute turbulent two-phase suspension flow. *International Journal of Multiphase Flow*, 13(2):247–256, mar 1987. ISSN 0301-9322. doi: 10.1016/0301-9322(87)90032-2. URL https://www.sciencedirect.com/science/article/pii/0301932287900322.

S. Lee and F. Durst. On the motion of particles in turbulent duct flows. *International Journal of Multiphase Flow*, 8(2):125–146, apr 1982. ISSN 03019322. doi: 10.1016/0301-9322(82)90013-1. URL http://linkinghub.elsevier.com/retrieve/pii/0301932282900131.

J. Lelouvetel, F. Bigillon, D. Doppler, I. Vinkovic, and J.-Y. Champagne. Experimental investigation of ejections and sweeps involved in particle suspension. *Water Resources Research*, 45(2):n/a—-n/a, 2009. ISSN 1944-7973. doi: 10.1029/2007WR006520. URL http://dx.doi.org/10.1029/2007WR006520.

D. Li, A. Wei, L. Kun, and F. Jianren. Direct numerical simulation of a particle-laden flow in a flat plate boundary layer. *International Journal of Multiphase Flow*, 79:124–143, mar 2016. ISSN 0301-9322. doi: 10.1016/J.IJMULTIPHASEFLOW.2015.10.011. URL https://www.sciencedirect.com/science/article/pii/S0301932215002505.

Y. Li, J. B. McLaughlin, K. Kontomaris, and L. Portela. Numerical simulation of particle-laden turbulent channel flow. *Physics of Fluids*, 13(10):2957, sep 2001. ISSN 1070-6631. doi: 10.1063/1.1396846. URL https://doi.org/10.1063/1.1396846.

F. D. Lillo, M. Cencini, S. Musacchio, and G. Boffetta. Clustering and turbophoresis in a shear flow without walls. *Physics of Fluids*, 28(3):35104, 2016. doi: 10.1063/1.4943274. URL https://doi.org/10.1063/1.4943274.

E. Limacher, C. Morton, and D. Wood. On the calculation of force from PIV data using the generalized added-mass and circulatory force decomposition. *Experiments in Fluids*, 60(1):4, nov 2018. ISSN 1432-1114. doi: 10.1007/s00348-018-2648-3. URL https://doi.org/10.1007/s00348-018-2648-3.

Y. Ling, M. Parmar, and S. Balachandar. A scaling analysis of added-mass and history forces and their coupling in dispersed multiphase flows. *International Journal of Multiphase Flow*, 57:102–114, dec 2013. ISSN 0301-9322. doi: 10.1016/J.IJMULTIPHASEFLOW.2013.07.005. URL https://www.sciencedirect.com/science/article/pii/S0301932213001109.

C. Marchioli and A. Soldati. Mechanisms for particle transfer and segregation in a turbulent boundary layer. *Journal of Fluid Mechanics*, 468:283–315, 2002. ISSN 0022-1120. doi: DOI:10.1017/S0022112002001738.

C. Marchioli, A. Giusti, M. V. Salvetti, and A. Soldati. Direct numerical simulation of particle wall transfer and deposition in upward turbulent pipe flow. *International Journal of Multiphase Flow*, 29(6):1017–1038, jun 2003. ISSN 0301-9322. doi: 10.1016/S0301-9322(03)00036-3. URL http://www.sciencedirect.com/science/article/pii/S0301932203000363.

C. Marchioli, M. Picciotto, and A. Soldati. Influence of gravity and lift on particle velocity statistics and transfer rates in turbulent vertical channel flow. *International Journal of Multiphase Flow*, 33(3):227–251, mar 2007. ISSN 0301-9322. doi: 10.1016/J.IJMULTIPHASEFLOW.2006.09.005. URL https://www.sciencedirect.com/science/article/pii/S0301932206001649.

C. Marchioli, A. Soldati, J. Kuerten, B. Arcen, A. Tanière, G. Goldensoph, K. Squires, M. Cargnelutti, and L. Portela. Statistics of particle dispersion in direct numerical simulations of wall-bounded turbulence: Results of an international collaborative benchmark test. *International Journal of Multiphase Flow*, 34(9):879–893, sep 2008. ISSN 0301-9322. doi: 10.1016/J.IJMULTIPHASEFLOW.2008.01.009. URL https://www.sciencedirect.com/science/article/pii/S0301932208000414.

M. R. Maxey and J. J. Riley. Equation of motion for a small rigid sphere in a nonuniform flow. *The Physics of Fluids*, 26(4):883–889, 1983. doi: 10.1063/1.864230. URL https://aip.scitation.org/doi/abs/10.1063/1.864230.

R. Mei. An approximate expression for the shear lift force on a spherical particle at finite reynolds number. *International Journal of Multiphase Flow*, 18(1):145–147, jan 1992. ISSN 0301-9322. doi: 10.1016/0301-9322(92)90012-6. URL https://www.sciencedirect.com/science/article/pii/0301932292900126.

R. Mei and R. J. Adrian. Flow past a sphere with an oscillation in the free-stream velocity and unsteady drag at finite Reynolds number. *Journal of Fluid Mechanics*, 237:323–341, apr 1992. ISSN 0022-1120. doi: 10.1017/S0022112092003434. URL https://www.cambridge.org/core/product/identifier/S0022112092003434/type/journal{_}article.

C. D. Meinhart, S. T. Wereley, and J. G. Santiago. A PIV algorithm for estimating time-averaged velocity fields. *Journal of Fluids engineering*, 122(2):285–289, 2000. ISSN 0098-2202.

Y. Meller and A. Liberzon. Particle–fluid interaction forces as the source of acceleration PDF invariance in particle size. *International Journal of Multiphase Flow*, 76:22–31, nov 2015. ISSN 0301-9322. doi: 10.1016/J.IJMULTIPHASEFLOW.2015.04.018. URL https://www.sciencedirect.com/science/article/pii/S0301932215001445.

M. C. Miller, I. N. McCave, and P. D. Komar. Threshold of sediment motion under unidirectional currents. *Sedimentology*, 24(4):507–527, 1977. doi: 10.1111/j.1365-3091.1977.tb00136.x. URL https://onlinelibrary.wiley.com/doi/abs/10.1111/j.1365-3091.1977.tb00136.x.

D. Milojević. Lagrangian Stochastic-Deterministic (LSD) Predictions of Particle Dispersion in Turbulence. *Particle & Particle Systems Characterization*, 7(1-4):181–190, 1990. ISSN 1521-4117. doi: 10.1002/ppsc.19900070132. URL http://dx.doi.org/10.1002/ppsc.19900070132.

J.-P. Minier and J. Pozorski. *Particles in wall-bounded turbulent flows: deposition, resuspension and agglomeration*. Springer, 2017.

R. D. Moser, J. Kim, and N. N. Mansour. Direct numerical simulation of turbulent channel flow up to Reτ=590. *Physics of Fluids*, 11(4):943–945, mar 1999. ISSN 1070-6631. doi: 10.1063/1.869966. URL http://dx.doi.org/10.1063/1.869966.

H. Nasr-El-Din, C. Shook, and J. Colwell. The lateral variation of solids concentration in horizontal slurry pipeline flow. *International Journal of Multiphase Flow*, 13(5):661–670, sep 1987. ISSN 0301-9322. doi: 10.1016/0301-9322(87)90043-7. URL https://www.sciencedirect.com/science/article/pii/0301932287900437.

Y. Nino and M. H. Garcia. Experiments on particle-turbulence interactions in the near-wall region of an open channel flow: implications for sediment transport. *Journal of Fluid Mechanics*, 326(-1):285, nov 1996. ISSN 0022-1120. doi: 10.1017/S0022112096008324. URL http://www.journals.cambridge.org/abstract{_}S0022112096008324.

J. Nouri, J. Whitelaw, and M. Yianneskis. Particle motion and turbulence in dense two-phase flows. *International Journal of Multiphase Flow*, 13(6):729–739, nov 1987. ISSN 03019322. doi: 10.1016/0301-9322(87)90062-0. URL http://linkinghub.elsevier.com/retrieve/pii/0301932287900620.

J. Oliveira, C. van der Geld, and J. Kuerten. Lagrangian velocity and acceleration statistics of fluid and inertial particles measured in pipe flow with 3D particle tracking velocimetry. *International Journal of Multiphase Flow*, 73:97–107, jul 2015. ISSN 0301-9322. doi: 10.1016/J.IJMULTIPHASEFLOW.2015.03.017. URL https://www.sciencedirect.com/science/article/pii/S0301932215000737.

J. L. G. Oliveira, C. W. M. van der Geld, and J. G. M. Kuerten. Lagrangian and Eulerian Statistics of Pipe Flows Measured with 3D-PTV at Moderate and High Reynolds Numbers. *Flow, Turbulence and Combustion*, 91(1):105–137, jul 2013. ISSN 1573-1987. doi: 10.1007/s10494-013-9457-9. URL https://doi.org/10.1007/s10494-013-9457-9.

S. Olivieri, F. Picano, G. Sardina, D. Iudicone, and L. Brandt. The effect of the Basset history force on particle clustering in homogeneous and isotropic turbulence. *Physics of Fluids*, 26(4):41704, 2014. doi: 10.1063/1.4871480. URL https://doi.org/10.1063/1.4871480.

C. Oseen. Hydrodynamik, 1927.

Y. Pan and S. Banerjee. Numerical simulation of particle interactions with wall turbulence. *Physics of Fluids*, 8(10):2733–2755, 1996. doi: 10.1063/1.869059. URL https://doi.org/10.1063/1.869059.

V. C. Patel and M. R. Head. Some observations on skin friction and velocity profiles in fully developed pipe and channel flows. *Journal of Fluid Mechanics*, 38(1):181–201, 1969. doi: 10.1017/S0022112069000115.

F. Picano, W.-P. Breugem, and L. Brandt. Turbulent channel flow of dense suspensions of neutrally buoyant spheres. *Journal of Fluid Mechanics*, 764:463–487, feb 2015. ISSN 0022-1120. doi: 10.1017/jfm.2014.704. URL http://www.journals.cambridge.org/abstract{_}S0022112014007046.

S. B. Pope. *Turbulent Flows*. Cambridge University Press, Cambridge, 2000. ISBN 9780511840531. doi: 10.1017/CBO9780511840531. URL http://ebooks.cambridge.org/ref/id/CBO9780511840531.

L. Prandtl. Bemerkungen über die entstehung der turbulenz. *ZAMM - Journal of Applied Mathematics and Mechanics / Zeitschrift für Angewandte Mathematik und Mechanik*, 1 (6):431–436, 1921. doi: 10.1002/zamm.19210010602. URL https://onlinelibrary.wiley.com/doi/abs/10.1002/zamm.19210010602.

N. M. Qureshi, M. Bourgoin, C. Baudet, A. Cartellier, and Y. Gagne. Turbulent Transport of Material Particles: An Experimental Study of Finite Size Effects. *Phys. Rev. Lett.*, 99 (18):184502, oct 2007. doi: 10.1103/PhysRevLett.99.184502. URL https://link.aps.org/doi/10.1103/PhysRevLett.99.184502.

M. Raffel, C. E. Willert, J. Kompenhans, and Others. *Particle image velocimetry: a practical guide*. Springer Science & Business Media, 2007.

M. Rashidi, G. Hetsroni, and S. Banerjee. Particle-turbulence interaction in a boundary layer. *International Journal of Multiphase Flow*, 16(6):935–949, nov 1990. ISSN 03019322. doi: 10.1016/0301-9322(90)90099-5. URL http://linkinghub.elsevier.com/retrieve/pii/0301932290900995.

M. Reeks. The transport of discrete particles in inhomogeneous turbulence. *Journal of Aerosol Science*, 14(6):729–739, jan 1983. ISSN 0021-8502. doi: 10.1016/0021-8502(83)90055-1. URL http://www.sciencedirect.com/science/article/pii/0021850283900551.

M. Righetti and G. P. Romano. Particle–fluid interactions in a plane near-wall turbulent flow. *Journal of Fluid Mechanics*, 505:93–121, 2004. ISSN 0022-1120. doi: DOI:10.1017/S0022112004008304. URL https://www.cambridge.org/core/article/particlefluid-interactions-in-a-plane-nearwall-turbulent-flow/BB767577DF56EE5B02AD976A2A03DF08.

M. Roco and G. Addie. Erosion wear in slurry pumps and pipes. *Powder Technology*, 50 (1):35–46, mar 1987. ISSN 00325910. doi: 10.1016/0032-5910(87)80081-5. URL http://linkinghub.elsevier.com/retrieve/pii/0032591087800815.

P. G. Saffman. The lift on a small sphere in a slow shear flow. *Journal of Fluid Mechanics*, 22(2):385–400, 1965. ISSN 0022-1120. doi: DOI:10.1017/S0022112065000824. URL https://www.cambridge.org/core/article/lift-on-a-small-sphere-in-a-slow-shear-flow/56A8044522E68A3EB2CDB9C81D3DEE75.

P. G. Saffman and J. S. Turner. On the collision of drops in turbulent clouds. *Journal of Fluid Mechanics*, 1(1):16–30, 1956. doi: 10.1017/S0022112056000020.

G. Sardina, P. Schlatter, L. Brandt, F. Picano, and C. M. Casciola. Wall accumulation and spatial localization in particle-laden wall flows. *Journal of Fluid Mechanics*, 699:50–78, may 2012. ISSN 0022-1120. doi: 10.1017/jfm.2012.65. URL http://www.journals.cambridge.org/abstract{_}S0022112012000651.

D. Schanz, S. Gesemann, and A. Schröder. Shake-The-Box: Lagrangian particle tracking at high particle image densities. *Experiments in Fluids*, 57(5):70, apr 2016. ISSN 1432-1114. doi: 10.1007/s00348-016-2157-1. URL http://dx.doi.org/10.1007/s00348-016-2157-1.

L. Schiller and A. Naumann. Uber die grundlegenden berechnungen bei der schwerkraftaufbereitung. *Z. Ver. deut. Ing.*, 77:318–326, 1933. URL https://ci.nii.ac.jp/naid/10006954540/en/.

H. Schlichting and K. Gersten. *Boundary-Layer Theory*. Springer, Berlin, Heidelberg, 2017. ISBN 978-3-662-52919-5. doi: https://doi.org/10.1007/978-3-662-52919-5.

J. F. G. Schneiders and F. Scarano. Dense velocity reconstruction from tomographic PTV with material derivatives. *Experiments in Fluids*, 57(9):139, aug 2016. ISSN 1432-1114. doi: 10.1007/s00348-016-2225-6. URL https://doi.org/10.1007/s00348-016-2225-6.

X. Shao, T. Wu, and Z. Yu. Fully resolved numerical simulation of particle-laden turbulent flow in a horizontal channel at a low Reynolds number. *Journal of Fluid Mechanics*, 693:319–344, feb 2012. ISSN 0022-1120. doi: 10.1017/jfm.2011.533. URL http://www.journals.cambridge.org/abstract{_}S0022112011005337.

R. Shokri, S. Ghaemi, D. S. Nobes, and R. S. Sanders. Investigation of particle-laden turbulent pipe flow at high-Reynolds-number using particle image/tracking velocimetry (PIV/PTV). *International Journal of Multiphase Flow*, 89:136–149, 2017. ISSN 03019322. doi: 10.1016/j.ijmultiphaseflow.2016.06.023. URL http://dx.doi.org/10.1016/j.ijmultiphaseflow.2016.06.023.

C. A. Shook, M. McKibben, and M. Small. Experimental investigation of some hydrodynamic factors affecting slurry pipeline wall erosion. *The Canadian Journal of Chemical Engineering*, 68(1):17–23, 1990. doi: 10.1002/cjce.5450680102. URL https://onlinelibrary.wiley.com/doi/abs/10.1002/cjce.5450680102.

M. Simcik and M. Ruzicka. Added mass of dispersed particles by CFD: Further results. *Chemical Engineering Science*, 97:366–375, jun 2013. ISSN 0009-2509. doi: 10.1016/J.CES.2013.04.041. URL https://www.sciencedirect.com/science/article/pii/S0009250913003096?via{%}3Dihub.

A. Soldati and C. Marchioli. Physics and modelling of turbulent particle deposition and entrainment: Review of a systematic study. *International Journal of Multiphase Flow*, 35(9):827 – 839, 2009. ISSN 0301-9322. doi: https://doi.org/10.1016/j.ijmultiphaseflow.2009.02.016. URL http://www.sciencedirect.com/science/article/pii/S0301932209000329. Special Issue: Point-Particle Model for Disperse Turbulent Flows.

S. M. Soloff, R. J. Adrian, and Z.-C. Liu. Distortion compensation for generalized stereoscopic particle image velocimetry. *Measurement Science and Technology*, 8(12):1441, 1997. URL http://stacks.iop.org/0957-0233/8/i=12/a=008.

M. Sommerfeld. Analysis of collision effects for turbulent gas–particle flow in a horizontal channel: Part I. Particle transport. *International Journal of Multiphase Flow*, 29(4):675–699, 2003. ISSN 03019322. doi: 10.1016/S0301-9322(03)00031-4. URL http://www.sciencedirect.com/science/article/pii/S0301932203000314.

G. Sridhar and J. Katz. Drag and lift forces on microscopic bubbles entrained by a vortex. *Physics of Fluids*, 7(2):389–399, feb 1995. ISSN 1070-6631. doi: 10.1063/1.868637. URL http://dx.doi.org/10.1063/1.868637.

G. G. Stokes. On the Effect of the Internal Friction of Fluids on the Motion of Pendulums. *Transactions of the Cambridge Philosophical Society*, 9:8, Jan. 1851.

B. M. Sumer. Mean velocity and longitudinal dispersion of heavy particles in turbulent open-channel flow. *Journal of Fluid Mechanics*, 65(01):11, aug 1974. ISSN 0022-1120. doi: 10.1017/S0022112074001212. URL http://www.journals.cambridge.org/abstract{_}S0022112074001212.

B. M. Sumer and B. Oguz. Particle motions near the bottom in turbulent flow in an open channel. *Journal of Fluid Mechanics*, 86, may 1978. doi: 10.1017/S0022112078001020. URL https://www.cambridge.org/core/product/283D60A98D78AE75E230D882E80F3409http://www.journals.cambridge.org/abstract{_}S0022112078001020.

A. J. Sutherland. Proposed mechanism for sediment entrainment by turbulent flows. *Journal of Geophysical Research*, 72(24):6183–6194, 1967. doi: 10.1029/JZ072i024p06183. URL https://agupubs.onlinelibrary.wiley.com/doi/abs/10.1029/JZ072i024p06183.

Y. Suzuki, M. Ikenoya, and N. Kasagi. Simultaneous measurement of fluid and dispersed phases in a particle-laden turbulent channel flow with the aid of 3-D PTV. *Experiments in Fluids*, 29(1):S185—-S193, dec 2000. ISSN 1432-1114. doi: 10.1007/s003480070020. URL http://dx.doi.org/10.1007/s003480070020.

T. Tanaka and J. K. Eaton. Classification of turbulence modification by dispersed spheres using a novel dimensionless number. *Phys. Rev. Lett.*, 101:114502, Sep 2008. doi: 10.1103/PhysRevLett.101.114502. URL https://link.aps.org/doi/10.1103/PhysRevLett.101.114502.

S. Taneda. Experimental Investigation of the Wake behind a Sphere at Low Reynolds Numbers. *Journal of the Physical Society of Japan*, 11(10):1104–1108, oct 1956. ISSN 0031-9015. doi: 10.1143/JPSJ.11.1104. URL http://dx.doi.org/10.1143/JPSJ.11.1104.

C. Tchen. *Mean value and correlation problems connected with the motion of small particles in a turbulent field*. PhD thesis, Martinus Nijhoff, Delft University, Hague, 1947.

H. Tennekes and J. L. Lumley. *A First Course in Turbulence*. MIT Press, 1972. URL https://books.google.ca/books?id={_}pSyuQAACAAJ.

H. Traugott and A. Liberzon. Experimental study of forces on freely moving spherical particles during resuspension into turbulent flow. *International Journal of Multiphase Flow*, 88:167–178, jan 2017. ISSN 0301-9322. doi: 10.1016/J.IJMULTIPHASEFLOW.2016.10.003. URL https://www.sciencedirect.com/science/article/pii/S0301932215300860.

Y. Tsuji and Y. Morikawa. LDV measurements of an air–solid two-phase flow in a horizontal pipe. *Journal of Fluid Mechanics*, 120(-1):385, jul 1982. ISSN 0022-1120. doi: 10.1017/S002211208200281X. URL http://www.journals.cambridge.org/abstract{_}S002211208200281X.

Y. Tsuji, Y. Morikawa, and H. Shiomi. Ldv measurements of an air-solid two-phase flow in a vertical pipe. *Journal of Fluid Mechanics*, 139:417–434, 1984. doi: 10.1017/S0022112084000422.

M. van Hinsberg, J. ten Thije Boonkkamp, and H. Clercx. An efficient, second order method for the approximation of the Basset history force. *Journal of Computational Physics*, 230(4):1465–1478, feb 2011. ISSN 0021-9991. doi: 10.1016/J.JCP.2010.11.014. URL https://www.sciencedirect.com/science/article/pii/S0021999110006224.

R. van Hout. Time-resolved PIV measurements of the interaction of polystyrene beads with near-wall-coherent structures in a turbulent channel flow. *International Journal of Multiphase Flow*, 37(4):346–357, may 2011. ISSN 0301-9322. doi: 10.1016/J.IJMULTIPHASEFLOW.2010.11.004. URL https://www.sciencedirect.com/science/article/pii/S030193221000193X.

A. Varaksin, Y. Polezhaev, and A. Polyakov. Effect of particle concentration on fluctuating velocity of the disperse phase for turbulent pipe flow. *International Journal of Heat and Fluid Flow*, 21(5):562–567, 2000. ISSN 0142727X. doi: 10.1016/S0142-727X(00)00045-X. URL http://www.sciencedirect.com/science/article/pii/S0142727X0000045X.

I. Vinkovic, D. Doppler, J. Lelouvetel, and M. Buffat. Direct numerical simulation of particle interaction with ejections in turbulent channel flows. *International Journal of Multiphase Flow*, 37(2):187–197, 2011. ISSN 03019322. doi: 10.1016/j.ijmultiphaseflow.2010.09.008. URL http://www.sciencedirect.com/science/article/pii/S0301932210001539.

G. A. Voth. *Lagrangian Acceleration Measurements in Turbulence at Large Reynolds Numbers*. Phd thesis, Cornell University, 2000.

A. W. Vreman. Turbulence attenuation in particle-laden flow in smooth and rough channels. *Journal of Fluid Mechanics*, 773:103–136, jun 2015. ISSN 0022-1120. doi: 10.1017/jfm.2015.208. URL http://www.journals.cambridge.org/abstract{_}S0022112015002086.

L.-P. Wang, A. S. Wexler, and Y. Zhou. Statistical mechanical description and modelling of turbulent collision of inertial particles. *Journal of Fluid Mechanics*, 415: S0022112000008661, jul 2000. ISSN 00221120. doi: 10.1017/S0022112000008661. URL http://www.journals.cambridge.org/abstract{_}S0022112000008661.

J. Westerweel, D. Dabiri, and M. Gharib. The effect of a discrete window offset on the accuracy of cross-correlation analysis of digital PIV recordings. *Experiments in Fluids*, 23(1):20–28, may 1997. ISSN 1432-1114. doi: 10.1007/s003480050082. URL https://doi.org/10.1007/s003480050082.

F. White. *Viscous Fluid Flow*. McGraw-Hill international edition. McGraw-Hill, 2006. ISBN 9780071244930. URL https://books.google.ca/books?id=fl6wPwAACAAJ.

B. Wieneke. Stereo-PIV using self-calibration on particle images. *Experiments in Fluids*, 39(2):267–280, aug 2005. ISSN 1432-1114. doi: 10.1007/s00348-005-0962-z. URL http://dx.doi.org/10.1007/s00348-005-0962-z.

B. Wieneke. Volume self-calibration for 3D particle image velocimetry. *Experiments in Fluids*, 45(4):549–556, oct 2008. ISSN 1432-1114. doi: 10.1007/s00348-008-0521-5. URL http://dx.doi.org/10.1007/s00348-008-0521-5.

B. Wieneke. Iterative reconstruction of volumetric particle distribution. *Measurement Science and Technology*, 24(2):24008, 2013. ISSN 0957-0233. URL http://stacks.iop.org/0957-0233/24/i=2/a=024008.

W. W. Willmarth and S. S. Lu. Structure of the Reynolds stress near the wall. *Journal of Fluid Mechanics*, 55(01):65, sep 1972. ISSN 0022-1120. doi: 10.1017/S002211207200165X. URL http://www.journals.cambridge.org/abstract{_}S002211207200165X.

Y. Wu, H. Wang, Z. Liu, J. Li, L. Zhang, and C. Zheng. Experimental investigation on turbulence modification in a horizontal channel flow at relatively low mass loading. *Acta Mechanica Sinica*, 22(2):99–108, apr 2006. ISSN 1614-3116. doi: 10.1007/s10409-006-0103-9. URL https://doi.org/10.1007/s10409-006-0103-9.

Y. Yamamoto, M. Potthoff, T. Tanaka, T. Kajishima, and Y. Tsuji. Large-eddy simulation of turbulent gas–particle flow in a vertical channel: effect of considering inter-particle collisions. *Journal of Fluid Mechanics*, 442:303–334, 2001. ISSN 0022-1120. doi: DOI: 10.1017/S0022112001005092.

B. Yung, H. Merry, and T. Bott. The role of turbulent bursts in particle re-entrainment in aqueous systems. *Chemical Engineering Science*, 44(4):873–882, jan 1989. ISSN 0009-2509. doi: 10.1016/0009-2509(89)85260-1. URL https://www.sciencedirect.com/science/article/pii/0009250989852601.

S. Zade, P. Costa, W. Fornari, F. Lundell, and L. Brandt. Experimental investigation of turbulent suspensions of spherical particles in a square duct. *Journal of Fluid Mechanics*, 857:748–783, dec 2018. ISSN 0022-1120. doi: 10.1017/jfm.2018.783. URL https://www.cambridge.org/core/product/identifier/S0022112018007838/type/journal{_}article.

F. Zhao, W. George, and B. Van Wachem. Four-way coupled simulations of small particles in turbulent channel flow: The effects of particle shape and Stokes number. *Physics of Fluids*, 27(8):83301, aug 2015. ISSN 1070-6631. doi: 10.1063/1.4927277. URL http://aip.scitation.org/doi/abs/10.1063/1.4927277.

L. Zhao, H. I. Andersson, and J. J. J. Gillissen. Interphasial energy transfer and particle dissipation in particle-laden wall turbulence. *J. Fluid Mech.*, 715:32, jan 2013. ISSN 0022-1120. doi: 10.1017/jfm.2012.492. URL http://www.journals.cambridge.org/abstract{_}S0022112012004922.

Y. Zhou, A. S. Wexler, and L.-P. Wang. On the collision rate of small particles in isotropic turbulence. II. Finite inertia case. *Physics of Fluids*, 10(5):1206–1216, 1998. doi: 10.1063/1.869644. URL https://doi.org/10.1063/1.869644.